Corrections to inter-blade-row flow measurements in axial compressors

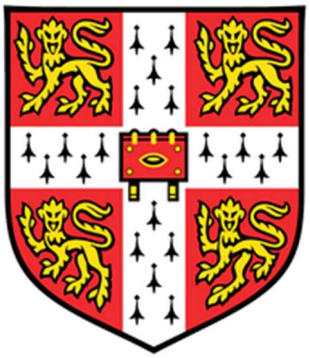

Viacheslav Alekseevich Sedunin

Department of Engineering

University of Cambridge

This dissertation is submitted for the degree of

Doctor of Philosophy

Downing College

December 2022

Declaration

I hereby declare that except where specific reference is made to the work of others, the contents of this dissertation are original and have not been submitted in whole or in part for consideration for any other degree or qualification in this, or any other university. This dissertation is the result of my own work and includes nothing which is the outcome of work done in collaboration, except where specifically indicated in the text. This dissertation contains fewer than 65,000 words including appendices, bibliography, footnotes, tables, and equations, and has fewer than 150 figures.

Viacheslav Alekseevich Sedunin

December 2022

Acknowledgements

The author is grateful to a number of organisations and individuals who have supported this work. First of all, Liping Xu, whose supervision of this work has been invaluable. Only through his input into the project has it been able to make an impact on the industry and the fundamental research of academia. In addition, James Taylor and Demetrios Lefas offered their insights and experience as well as endless support that was vital for this project.

Financial support by the Education Global research foundation is greatly appreciated, as are the experimental facilities provided by the Whittle laboratory and PAO 'Gazprom', as well as the pastoral support provided by Downing College.

Support within the Whittle lab has been forthcoming from all. Special thanks go to Bowen Ding for his introduction to the flow measurements at his rig; Tashiv Ramsander for his ideas about the probe design and his support and experience in the manufacturing process; and to Sam Grimshaw, Chris Clark, and Alejandro Castillias for their continuous support and advice throughout the experimental campaign and data processing. The support of the technical staff led by John Saunders and Dominic Basham has been excellent; the author would especially like to thank Luke Arnold for manufacturing a particularly complicated traversing gear, which reliably worked on the real industrial gas turbine engine.

From the industrial side, first I would like to thank A.O.Prokopets for the initiation of the project, his continuous support and the inspiration for me to work with the world-leading team. Also great thanks to D.A.Doronin, A.S.Titov, V.B.Bagaev, N.I.Kolomiets and many of their colleagues for their great team effort. Special thanks to Prith Harasghama for introducing me to the world of international science and Nikita Kulikov, whom I happened to meet in the very last and important moment of my test campaign, and who made a world-class control system for my traverse gear.

From Ural Federal University, which has been a part of my life for almost 20 years, I am grateful to O.V.Komarov for the project management and continuous supply of exciting industrial challenges; to I.A.Kalinin and Yu.G.Marchenko for their selfless work during the

experimental campaign and productive research discussions; to V.L.Blinov, S.A.Serkov, D.E.Ledkov, A.M.Nevolin, A.V.Skorokhodov and other colleagues and students of mine.

Especially, here I want to mention the teachers in various periods of my life, whose lessons made me the person I am now: I.D.Borodin, V.N.Rakhimov, E.V.Uriev, B.S.Revzin, I.D.Larionov, S.V.Zaitsev, G.B.Uflyand.

Life in Cambridge would never be so enjoyable without my friends Rakoen Martens, Hassan Imran, Yizhou Wan, Dusan Perovic, Jacques Li, Omer Tastemur, Pawel Przytarski, Aljaz Kotnik, Ildar Abdulkhaimov, Daria Mitko and all the nice people from Downing College Boat Club and Cambridge University Russian Society.

Everything else I owe to my family, Alexey, Lola, Alexander, and my wife Anastasia for believing in me and making my ambitions possible.

Abstract

For industrial multistage axial compressors, flow measurements in axial gaps between the blade rows are limited by mechanical constraints and the high uncertainty of the gathered data. The main factors affecting measurement uncertainties are the confined space between the blade rows, large relative dimensions of the probe and the holding stem, high flow velocities and complex flow structures.

In this thesis, it has been shown that the uncertainties become large when a cylindrical probe is placed in proximity to the blades or the large vortical structures, such as blade wakes or separation zones, or when the flow Mach number exceeds the probe critical values of 0.7. In these cases, the uncertainties may exceed 10° in the flow angle and over 30% of dynamic head in measured static pressure. A set of boundaries are defined for geometrical and flow conditions, where the deviations from the true value of the undisturbed flow are quasi-linear and can be estimated. These boundaries are based on the physical principles of the internal turbomachinery flows and can be universally applied to other multistage compressors.

The corrections were applied first to a CFD-simulated probe placed at representative locations along the span and circumference of the passage both upstream and downstream of stator blade rows at representative flow conditions. When the corrections were applied, the measurement uncertainties caused by the probe's flow field distortion were reduced to ±1° in the flow angle and to ±5% of the dynamic head.

Finally, the corrections were applied to the experimental spanwise measurements made on an axial compressor as a part of an industrial gas turbine during its operation on site. A procedure was developed to control the consistency of the measurement corrections based on fundamental physical principles such as mass and energy conservation and radial equilibrium. The corrected data have shown improved consistencies: the variation of the integrated mass flow values along the compressor axial locations was reduced from ±15% to ±4% from the inlet value, and the static pressure distribution along the span became within 5% of dynamic head away from the radial equilibrium condition compared to more than 30% initially.

The corrections presented in this thesis have fixed the first-order errors relating to the use of finite-size probes in multistage axial compressors, namely, consistently identifying and correcting for the blockage from the probe itself and the potential field of the upstream and downstream blade rows. Before the corrections, these errors meant spanwise measurements of flow angle and pressure had large uncertainties and errors; therefore, they were rarely performed in multistage industrial compressor environments. After the corrections, the results of spanwise traversing have shown improved consistency and can now be used as feedback in the design and development of multistage axial compressors.

Table of contents

List of figures

List of tables

Nomenclature

Roman Symbols

C_{max}	Maximum thickness of the airfoil
C_p	Pressure coefficient
C_{PYAW}	Probe calibration coefficient for yaw angle
C_{PTOTAL}	Probe calibration coefficient for total pressure
$C_{PSTATIC}$	Probe calibration coefficient for static pressure
$C_{p_{flow}}$	Pressure coefficient of the flow (measured with the probe or local undisturbed value)
$C_{p_{probe}}$	Pressure coefficient on the probe surface
C_0; C_1; C_2	Constant coefficients for parabolic correction
D	Dynamic coefficient for probe calibration
D_{probe}	Diameter of the probe head
Q	Side-pressure coefficient for probe calibration
Ma	Mach number
V	Flow velocity in the absolute frame
W	Flow velocity in the reference frame
U	Circumferential velocity of the rotor
y^+	Non-dimensional distance from the wall
$\overline{p_{s,1}}$	Pitchwise average static pressure at the inlet of the domain
$\overline{p_{o,1}}$	Pitchwise average total pressure at the inlet of the domain
P_1	Pressure tapping 1
P_2	Pressure tapping 2
P_3	Pressure tapping 3
C	Flow velocity

i	Incidence angle
$p_{s,o}$	Local value of the static pressure
$p_{o,o}$	Local value of the total pressure
P	Pressure
r	Radius
$\overline{T_{s,o}}$	Pitchwise averaged static temperature
i	Flow incidence angle
He	Euler work

Greek symbols

β	Flow angle
Δ	Difference between the parameters
ρ	Density
Λ	Stage reaction
$\phi = \frac{V_{axial}}{U_{mid}}$	Stage flow coefficient
φ	Angular position on the probe surface
$\psi = \frac{H_e}{{U_{mid}}^2}$	Stage loading coefficient

Acronyms

ANSYS CFX	Commercial CFD software
CFD	Computational Fluid Dynamics
FSS	Full-scale span
HPT	High-pressure turbine
LE	Leading edge of the blade
MF	Mass flow
OP	Operating point
PS	Pressure side
PT	Power turbine
RANS	Reynolds-averaged Navier-Stokes

SS	Suction side
SST	Shear stress transport turbulence model
SST GTM	Shear stress transport turbulence model with Gamma-Re-Theta transition model (γ-Re_θ) for the laminar-turbulent transition (see Menter et al (2004) for details)

Subscripts

0	Total pressure
1	Inlet conditions
2	Outlet conditions
ave	Average
axial	Axial component of the flow
circumferential	Circumferential component of the flow
corr	Corrected
ex	Exit
exp	Experimental
flow	Value of the flow
in	Inlet conditions
kin	Kinetic
local	Local value of the undisturbed flow
meas	Measured
MFA	Mass flow averaged
mid	At the mid-span
out	Outlet conditions
θ	Circumferential direction
R	Rotor
S	Stator
st	Static (for pressures)
undist	Value of the undisturbed flow

Chapter 1 Introduction

In the turbomachinery industry, design processes based on the intensive use of the methods of computational fluid dynamics (CFD) are now common practice for key gas turbine components such as axial compressors and turbines. These methods include two- and three-dimensional optimisation of the blade channels, consideration of fluid-structure interaction, and then matching compressor stages into one flow path. Unlike the traditional approach, where experimentally based correlations are used at each step of the process, in the simulation-based approach, the computational modelling results often completely substitute the experimental ones. Feedback to the design system is postponed until the moment when the full-scale demonstrator or even the pilot engine is manufactured. When the experimental data is only available so late in the development process, the measured parameters, spatial resolution of measurement points, and level of measurement uncertainty are crucial to the success of the whole project. This data then becomes important feedback to the design system.

1.1 Experimental work on the real gas turbine engines

Experimental work on the industrial gas turbine engines during their operation on site is more relevant for heavy-duty gas turbines, especially during modernisation and retrofit. This is because the real environment can have specific features that cannot be reproduced during subscale testing or testing of a group of stages, for example, realistic boundary conditions throughout a compressor operating line, radial gaps and manufacturing deviations, as well as system level features of the whole engine, including relative thermal expansions, leakages and bleeding mass flows, and operating point matching with the turbine. In addition, the capital cost for the subscale testing of the initial and the modernised design is usually prohibitive for the retrofit programs. Therefore, normally, one of the representative engines of the fleet is

chosen for the pilot trials, and additional instrumentations are set up on the engine for more detailed experimental data.

The industrial standard for compressor testing requires the flow parameters to be measured upstream and downstream of the whole compressor in the inlet and outlet ducts, and an effort is made to measure the mass flow averaged values. Such data is usually complemented by pressure measurements on the casing surface of the compressor between the blade rows, see for example Ikeguchi (2013). The latter provides information about stage matching, therefore it can be used, for example, for the identification of those stages approaching stall limits at various engine operating conditions. However, the casing pressures cannot provide necessary radial information about the flow, which is especially important when the newly designed blades are leant and swept, accounting for three-dimensional effects. For such blades it is important to achieve the design intent along the whole blade span.

To measure the radial flow field in a full-scale compressor, a common industrial practice would be an instrumentation of the leading edges of several blades of each stator blade row along the compressor with so-called Kiel probes for measuring total pressure. Normally this is measured at five-to-10 points along the span downstream of rotors.

In comparison with the instrumentation of leading edges, the spanwise traversing with a three hole probe has the following benefits. First, it allows three parameters— flow angle, total and static pressures—instead of one to be obtained. Second, the measurements can be taken at multiple measurement planes both upstream and downstream of stators by moving the traverse gear. This provides a low cost route compared to instrumentation of blade leading edges at every stator blade row, which is especially beneficial when several sets of compressor blades are being tested. Finally, traversing enables better spatial resolution. Achieving the same resolution with Kiel probes is not practical.

In a laboratory environment, traversing is widely used in large-scale low-speed compressor rigs where the probe blockage can be minimised, the aerodynamic loading on the traverse stem is relatively low so they can be slim, and the axial space is designed to be sufficient to accommodate necessary fixtures at optimal locations both radially and circumferentially. However, until recently, the spanwise traversing in gas turbine engines working under real operating conditions was considered to be unfeasible. This is because of the limited axial spacing between the blade rows and the resultant risk of blade impact, and high flow speeds,

which force the probe heads and the supporting stems to be made relatively large. As a result, the probe blockage and its interaction with the blade flow field can no longer be neglected. In addition, the circumferential motion of the probe is not possible due to the limited space on the casing and requirements for its structural integrity, so there are only a few traversing locations along the blade pitch available at each measurement plane. This thesis is aimed to extend the availability of the spanwise traversing to industrial multistage compressor testing by addressing these problems.

1.2 Project Motivation

The axial compressor of interest is a 10-stage subsonic industrial compressor with moderate stage loading, representative of modern industrial compressors. Several issues were associated with the compressor's stability at off-design and there were multiple cases of blade failure. The improvement of compressor performance was the core motivation for the research and development project.

As a part of this project, advanced measurement techniques were implemented, one of which was the spanwise traversing in the axial gaps between the blade rows. The need for such a detailed measurement was due to the fact that the new version of compressor blading was meant to be installed directly to the engine, without prior low-speed or isolated compressor testing. That is why any experimental knowledge of the newly designed compressor could only be available during the on-site testing. Since the new blades featured a three-dimensional design approach to minimize the impact of secondary flows near the end walls, it was crucial to have detailed spanwise profiles of the flow parameters in addition to the casing pressures, normally used in the industry.

Figure 1.1 illustrates the challenges of spanwise traversing in the industrial compressor of interest. Figure 1.1 (a) shows a cross-section of the compressor with 13 planes, where the measurements were taken. The probe is immersed between the blade rows through a series of holes, shown, for example, for planes 7 and 8 in Figure 1.1 (b). A typical potential flow field upstream of the blades is shown in solid line in Figure 1.1 (c) as a variation of the difference between the local flow angle and the pitchwise averaged value. Two blades are sketched here for demonstration purposes at 0 and 1.0 of the pitch.

An empty circle in Figure 1.1 (c) is placed at a location of the casing hole in section 9 along the horizontal axis. The vertical position of the circle represents the measured value of the flow angle. It is unclear whether this measured value coincides with the local value of the undisturbed flow.

This leads to the research questions of this thesis: will probe measurements during traversing agree with the values of the undisturbed flow at a location of interest? If not, then what are the mechanisms causing the deviations, and how can these measurements be transferred to the local values and then representative averaged parameters of the flow?

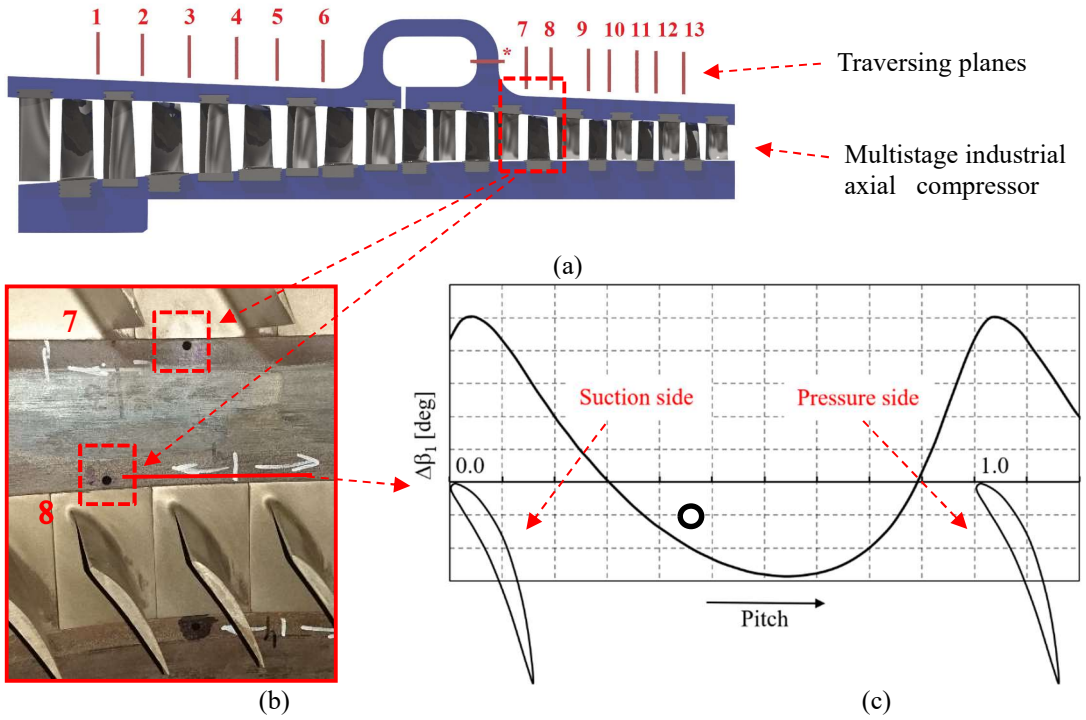

Figure 1.1 Compressor cross-section with traversing locations between the blade rows (a), a view of the holes in the casing (b) and the potential field upstream of stator blades (c)

Another important topic that the research has shed light upon is how the limited experimental data can be verified for its consistency, and how the combination of this data with computational results can be used to understand the flow in a real multistage compressor. Computational research is vulnerable to uncertainties in geometry, boundary conditions and turbulence modelling (Denton 2010). At the same time, the measurements are taken at limited locations and in limited operating conditions, and are subjected to measurement uncertainties.

In this work, an interconnection between the measured and computational data has been studied based on fundamental physical principles so that both data sources can be understood and processed accordingly.

1.3 Scope of the work

The compressor of interest is a part of the industrial gas turbine engine for mechanical drive applications. This is why in this thesis it is referred to as an industrial compressor. However, for aeroengines the limitations for spanwise traversing are identical: constrained axial spacing between the blade rows, high subsonic speeds at the middle and rear stages, and constrained space outside the casing for installation of the traversing gear. The compressor of interest also has representative loadings and geometrical features. Therefore, the word 'industrial' here and the findings of this work apply to axial compressors as a part of gas turbine engines regardless of the industry they are developed for, with representative geometrical parameters and with respect to all the complexities of external and internal structures.

For the compressor of interest, a tip Mach number of the first rotor reaches 0.8, therefore the compressibility effects can play a role in flow redistributions; the potential field interaction is also comparably stronger than that in the low-speed laboratory-standard compressors, where normally the Mach number does not exceed 0.3. This is why the research compressor in this thesis is referred to as high-speed. For the low-speed environment, detailed spanwise and pitchwise traversing is a common practice since the aerodynamic interaction with the probe can be minimised and the loads on the stem are lower. For high-speed subsonic flows, the distortion brought up by the instrumentation can no longer be neglected and the forces on the stem can be an order of magnitude higher. That is why traversing in high-speed subsonic compressors remains challenging and requires deeper understanding.

In this work, a cylindrical three-hole probe is considered; additional considerations would be required for wedge-type probes. The cylindrical probe introduces identical flow distortion regardless of its angular orientation. This eliminates an extra degree of freedom in the simulations and measurement corrections—the relative orientation of the probe along the blade surface. This is especially critical when the blades are twisted along the span and the probe has a fixed orientation during traversing. With the cylindrical probe only the locations of the

pressure tappings are important, whereas for more complicated probe geometries each combination of blade stagger and probe orientation would require a new set of simulations.

1.4 Outline

The thesis starts with an overview of relevant literature in Chapter 2. This includes experimental techniques for axial compressors suitable for on-site measurements, best practices for pneumatic probe design and calibration, as well as the aspects of flow field interaction with the immersed probe and measurement corrections found in the literature.

An experimental facility, for which the corrections were developed, together with the computational setup of the compressor and the immersed probe are presented in Chapter 3.

A simplified case of the flow around the probe in a constrained channel is studied numerically in Chapter 4, aiming to understand the basic mechanisms affecting the probe readings.

The flow around the probe upstream of the stator blades and its effect on the probe readings are presented in Chapter 5, and the same questions for measurements downstream of the stator are considered in Chapter 6. As a result, possible measurement corrections are discussed in these chapters with respect to the probe position and flow conditions.

In Chapter 7 the developed correction procedure is applied to the actual experimental results, and the improvement in data consistency is shown, based on the principles of mass conservation and radial equilibrium conditions. Finally, Chapter 7 presents the corrected experimental data in comparison with computational results and discusses how the actual flow field in the multistage compressor can be studied and verified considering the limited experimental data.

In the final chapter, conclusions and recommendations for future work are given.

Chapter 2 Literature review

When a pneumatic probe is used for flow measurements in an industrial multistage axial compressor, it has to be placed in between the blade rows with limited axial spacing, therefore the measured flow field near the probe is inevitably distorted. In his thesis, Coldrick (2003), defined this influence as a 'blockage effect'. He found that the probe caused a reduction in the mass flow in the blocked passage and a change in the pressure distribution about the probe resulting from a proximity effect.

When measuring along the circumference of the blade passage, the blockage effect is not uniform, and depends on the probe position relative to the blades. Therefore, the flow field upstream or downstream of the blade passage cannot be correctly resolved by circumferential traversing, as the measurements will be biased, especially when in proximity to the blades. Therefore the question arises of how limited data points measured in the least uncertain region in the middle of the passage can be reliably transformed into representative pitchwise averaged flow metrics.

This chapter aims to summarise current knowledge and experience about measurements in industrial axial compressors. It also covers the impact of the probe on the measured flow field, and the flow field reconstruction based on limited spatial measurements in relation to multistage axial compressors. Finally, the research questions are set.

2.1 Experimental work on industrial axial compressors

Over the past few decades, the role of computational fluid dynamics (CFD) in compressor design systems has grown drastically, taking a bigger portion of the design work from experimental studies. This helps to reduce the cost of development and shorten its timeframe. There are several compressors reported in the literature; see, for example, Ikeguchi (2012), Mito (2015), Tanaka (2012), and Outa (2016), where the whole multistage compressor design

and optimisation exercise was performed with the use of throughflow and CFD methods, and only the whole multistage setup was built and tested experimentally. Most of the reported compressors have had a wide experimental background in the past, so that the meridional shape of the flow path is historically formed and most of the blade designs have well-proven configurations. In addition, most of the modelling techniques used by the authors had been previously validated on similar designs. Even then the discrepancies in parameters between the obtained simulation results and newly tested designs were reported to be significant. However, with further developments in computational methods and the reducing costs of computational power, it is likely that the majority of design decisions in the future will be based on simulations, and experimental studies to be used for confirmation purposes only.

Denton (2010), in his paper about uncertainties in CFD methods points out that as engineers are exposed more and more to the results of CFD and less and less to experimental data, there is a danger that they may not realise the limitations of CFD and so will view its predictions as more reliable than they really are and not question them sufficiently. Cumpsty (2010), in his paper about the industrial experience in compressor CFD simulations points out that the modelling uncertainties in a single stage have a cumulative effect on the stage matching. Even when each stage is well designed for expected boundary conditions, the uncertainties in blockage estimation and losses can build up and affect the stage matching, which can lead to a shortfall in compressor performance. Because of the growth in blockage in compressors, and the relation between the blockage and the pressure rise, the multistage compressor is the most common component affected by this.

Figure 2.1 from Ikeguchi (2012) shows the experimental map of the CFD-optimised axial compressor. The first build (solid triangles) failed to provide the required pressure ratio; according to the authors, this was due to the middle stages being overloaded at design point and in reality have not produced sufficient pressure rise. This resulted in an increased flow coefficient to the rear stages and prevented them from producing sufficiently high pressure ratios, which in turn caused the less-than-intended overall compressor pressure ratio. As an adjustment solution on site, the authors decided to vary the bleed after the seventh stage of the compressor (empty triangles in Figure 2.1). Increased bleed allowed the rear stages to be loaded up by reducing their inlet flow coefficients and allowing the compressor to reach its design operating point, even though the stall margin was minimum. This paper illustrates how the

stage matching can have a detrimental effect on compressor performance. The causes of the mismatch were investigated by comparing the casing pressures at limited axial locations.

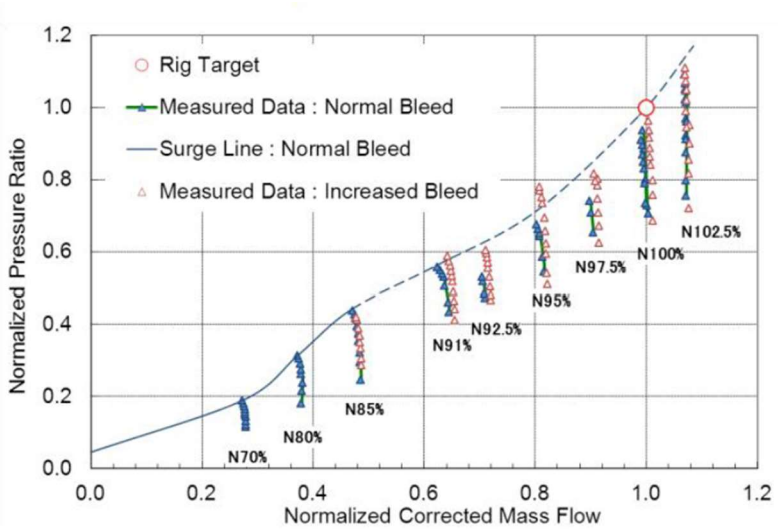

Figure 2.1 Experimental map of the first build of the axial compressor, optimised with CFD (Ikeguchi et al., 2012)

Figure 2.2 shows the effect of the increased bleed on the compressor performance. Initial error in stage matching caused the rear stages to underperform by 12% of the stage pressure rise. Increased bleed allowed this deviation to decrease by half, eventually leading the designers towards re-staggering the rear stators to achieve the design intent. Overall, this work illustrates how the uncertainties in CFD simulations accumulate throughout the flow path and lead to incorrect design decisions. To understand the actual reason for stage mismatching, the designers would need to measure the stage-by-stage radial distributions of the flow between the blade rows and analyse the performance of each blade row individually.

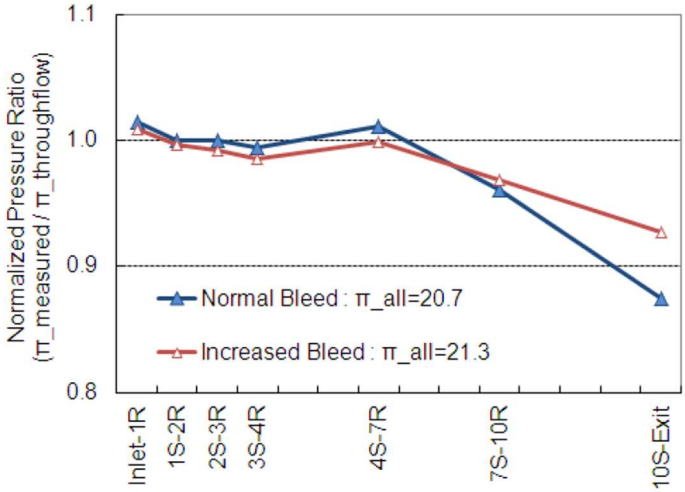

Figure 2.2 Normalised stage pressure ratio for the first build of the compressor (Ikeguchi et al., 2012)

Another point worth noting from this work is that the main source of experimental data was the pressure measurements on the compressor casing in seven planes between the blade rows. This was accompanied by several stator blades of the 1st, 4th, 7th, and 10th stages that had instrumented leading edges with five Kiel-type probes for total pressure measurements and more for the total temperature. This instrumentation was sufficient to find out underperforming stages and correct the stage matching accordingly; however, that level of spatial resolution would not be enough to study the core problem of stage underperformance, such as the difference to the CFD-simulated endwall blockage or the blade deviation.

A similar experience is reported by Wellborne and Delaney (2001), which is shown in Figure 2.3 as a pressure coefficient distribution along the compressor stages. The loading of the rear stages is overpredicted by multistage CFD simulation (white circles) and there is a distinctive shift in the performance of the middle stages, in particular stage 6. In this case, for the compressor of interest, finer spanwise measurements were available at the instrumented stator leading edges; these are shown in Figure 2.4. An deficit in total pressure of up to 5% at 0–20% of the span can be seen. Between 70% and 90% of the span on the same graph an additional measurement point could be beneficial to resolve the tip flow structure.

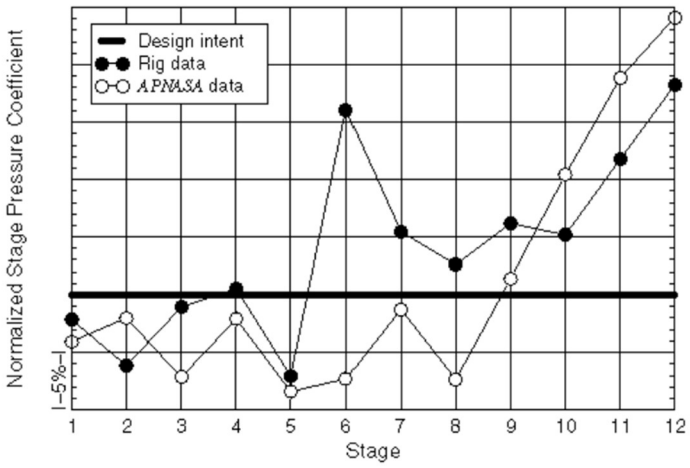

Figure 2.3 Normalised stage pressure coefficient from compressor rig and multistage CFD tool (Wellborne and Delaney, 2001)

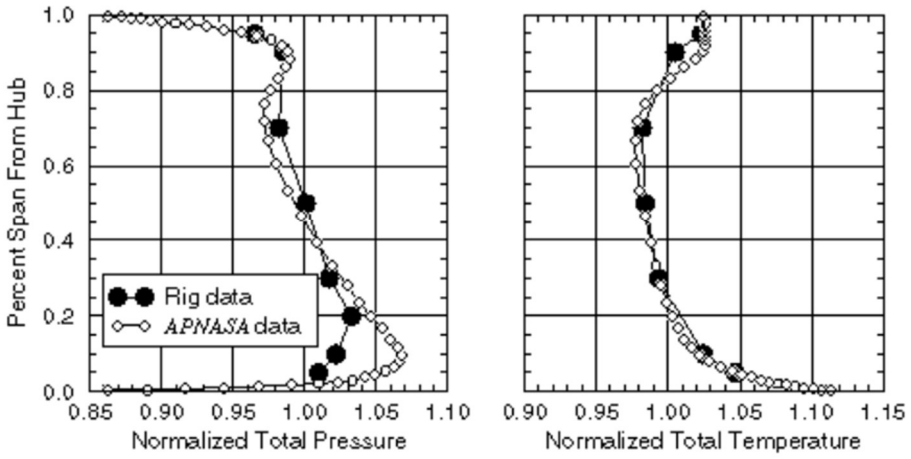

Figure 2.4 Radial distributions of normalised flow properties at the discharge of Rotor 6 (Wellborne and Delaney, 2001)

Brown and Fred (1962) provide insight into how the interstage performance data can be studied based on the pressure measurements at the casing wall between the blade rows. The authors point out that it is not just matching between the stages that matters, but also the radial matching of the blade sections between each other. Altogether the authors call it 'three-dimensional' matching. This can be judged when the characteristics of a middle stage are built at several compressor speed lines towards the compressor stalling point. However, as a

component of an industrial gas turbine engine, the compressor can be tested along the operating line only, and the spatial resolution of the pressure measurements along the span is crucial in assessing the three-dimensional matching of all the stages.

There are multiple papers on spanwise traversing in axial compressors, carried out on low-speed experimental rigs with one or few stages (see, for example, Tweedt and Okiishi (1983) and Robinson (1991)). The low speed and large dimensions allow for better spatial and time resolution of the pressure readings, but also allow for other types of instrumentation, including hot-wire anemometry, oil-flow visualisation, and others that are not available for full-speed machines. Lakshminarayana et al (1994) had a similar approach to the compressor with a tip Mach number of 0.5, but since the facility was made for research purposes with sufficient axial gaps and possible pitchwise motion of the probe, the pitchwise averaged values were used in spanwise distributions. Due to mechanical constraints and space limitations, for industrial testing like the one mentioned by Takuya et al.(2012), circumferential 2D traversing is not possible. For the current work the casing holes, originally made for the static pressure readings similar to Takuya et al. (2012), were used to immerse the cylindrical probe on the stainless steel solid cylindrical rod inside the compressor flow path.

Calvert et al.(1989) provide a detailed experience of traversing in a four-stage, high-speed research compressor. The authors point out that the compressor was axially extended compared to the industry representative: the axial gaps were increased up to 50% of blade chords to allow for the area traverses, placed between the blade rows. Together with a relatively low Mach number at the stator exit (0.265) and low probe blockage downstream of the stator, the authors did not to apply corrections to the cobra-probe measurements. However, the authors do point out that the measured flow angles near the stator wakes look unrealistic and should be omitted from consideration.

This section illustrates that spanwise traversing has been rarely used for studying the industry-ready high-speed multistage axial compressor environment, and that many compressor designs would benefit from fine measurement resolution in the radial direction between the blade rows. Many published papers reported stage mismatching when comparing CFD and experimental results. This is because CFD methods struggled to predict correct spanwise blockage. However, the differences in spanwise blockage between CFD and experimental data cannot be seen without the measurements of spanwise flow distribution.

Reported successful traversing experiences were affected by constrained space (which designers attempted to extend), high aerodynamic loading on the stem, and flow distortion introduced by the setup.

2.2 Pneumatic measurements in high-speed subsonic turbomachines

In the section below, the research is divided into three parts. First, the studies on the effects of the probe measurements in a constrained environment are presented. Second, when the probe is measuring upstream of the blade passage, the potential flow field around the blades is far from uniform, therefore the finite-size probe is measuring in the gradient flow. In addition, the presence of the probe, and especially the presence of the holding stem is disturbing the flow field, so that the measured parameters are no longer the same as those in the undisturbed flow.

Thirdly, when the probe is measuring downstream of the blades, it interacts with the intense vortical structures such as blade wakes, separation zones and tip flows. Such structures can be significantly affected by the presence of the probe; therefore the probe immersion can change the flow environment in principle, affecting blockage and diffusion in the blade passage.

Pneumatic measurements are commonly used when studying high-speed turbomachinery flows; several authors reported the change in the measured flow field due to immersion of the probe. Lee and Yoon (1999) experimentally studied the probe orientation effect on its calibration characteristics near the wall (Figure 2.5). Researchers found a change in a pitch angle coefficient when the probe was pointed towards the wall, parallel and away from the wall (Figure 2.5 (a), (b) and (c) respectively). In relation to this thesis, similar conclusions can be drawn for a yaw angle when a three-hole probe is approaching the blade wall with either of the sides.

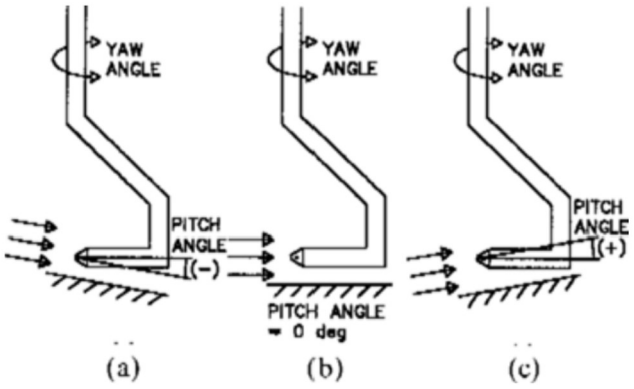

Figure 2.5 Some five-hole probe orientations near the wall: (a) pointed towards the wall, (b) parallel to the wall and (c) away from the wall (Lee and Yoon, 1999)

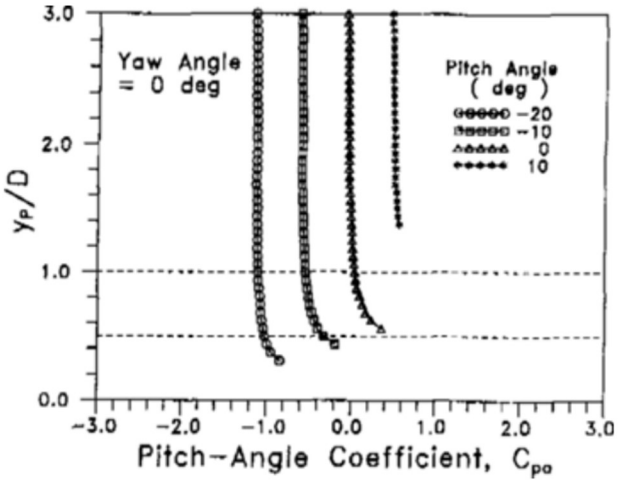

Figure 2.6 Effects of wall proximity on the pitch angle coefficient as a function of pitch angle between the probe and the wall (Lee and Yoon, 1999)

Figure 2.6 shows the change in the pitch angle coefficient as a function of the pitch angle. The authors conclude that the wall proximity effects are pronounced only when the distance from the wall is less than two probe diameters. However, in their case the incoming flow was parallel to the wall and the channel had zero pressure gradient along the flow. The authors also point out that the flow around the probe depends on the probe orientation. For turbomachinery applications this would mean that when a non-nulling probe moves along the twisted blade, the flow interaction between the probe and the blade will with at every location along the span. This would require including two more degrees of freedom into a possible correction

procedure: the angle between the probe axis and the wall, and the flow angle upstream of the wall (the blade incidence).

2.2.1 Uncertainties when measuring in a constrained environment

When a multihole probe is used to make measurements upstream or downstream of a compressor stator, if insufficient axial space is available, the probe must be positioned close to the blade passage. This situation is very similar to the problem of measuring in a finite size duct. Wyler (1975) investigated the effects of blockage of probes in a free jet and a duct. By using a single-hole cylindrical probe and rotating the probe in the flow to capture the pressure distribution for one revolution, Wyler was able to conclude that the effect of the probe on the flow in the duct was an increase in indicated Mach number and a decrease in the indicated pressure. When the probe was positioned in front of a nozzle, the effect was found to be in the opposite direction, giving a decrease in measured Mach number and an increase in pressure.

Mutlu Sumer and Fredsoe (1999) have shown the streamlines around a cylinder in proximity to the wall (Figure 2.7); when the probe is near the wall, the stagnation point is shifted towards the wall, causing the force normal to the wall (the lift) and asymmetry of the flow around the cylinder.

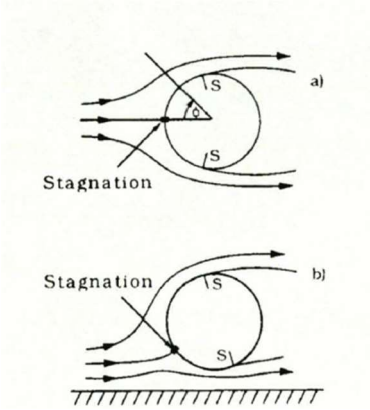

Figure 2.7 Streamlines around the cylinder in a free stream and in proximity to the wall (Mutlu Sumer and Fredsoe, 1999)

Vasseur et al. (2022) separated the effect of the wall proximity and the one from the boundary layer on the probe readings. They found that when approaching the wall the probe

measures a false pitch angle, as if the flow was diverging from the wall, but the boundary layer has the opposite effect. The two effects are in competition regarding pitch measurements and can compensate in some cases. The five-hole probe used in the study had a spherical shape and was approaching the wall with its tip, therefore it affected measured pitch angle. These findings can be relevant to a three-hole cylindrical probe approaching the blade surface at probe's side when measuring the yaw angle.

2.2.2 Uncertainties when measuring upstream of the stator blade row

One of the concerns about measurements in a real flow field is that the pressure gradient in that field will affect the calibration map of the pneumatic probe. Coldrick et al. (2004a) did an experimental study, calibrating the probe first in a laboratory wind tunnel, then the low-speed and high-speed compressors. In the case of the compressors, the probe was placed upstream of the stator blade row in the middle of the passage. It was found that the individual probe hole pressures were not modified by the non-uniform flow downstream of the rotor, provided that the probe was within a certain angular range from zero incidence. From the high-speed case, this range was found to be approximately ±5°. Since the individual hole pressures were not modified, it was assumed that any flow angle error arose because the entire pressure distribution about the probe was shifted, rather than an individual hole being in error.

Xiang et al. (2016) carried out an experimental study of the probe effect on the flow field in a compressor blade row. A large-scale probe was placed upstream of the stator blade cascade, as shown in Figure 2.8, together with the wake losses downstream of that blade row. It was found that when the probe is placed near the suction side of blade C (P3 in the figure), it can cause separation on the suction side, causing extra losses in the passage, whereas when placed closer to the pressure side (P4), the probe's wake joining both the leading edge of blade B and the total wake downstream of blade B does not affect the losses to the same extent as it does in location P3.

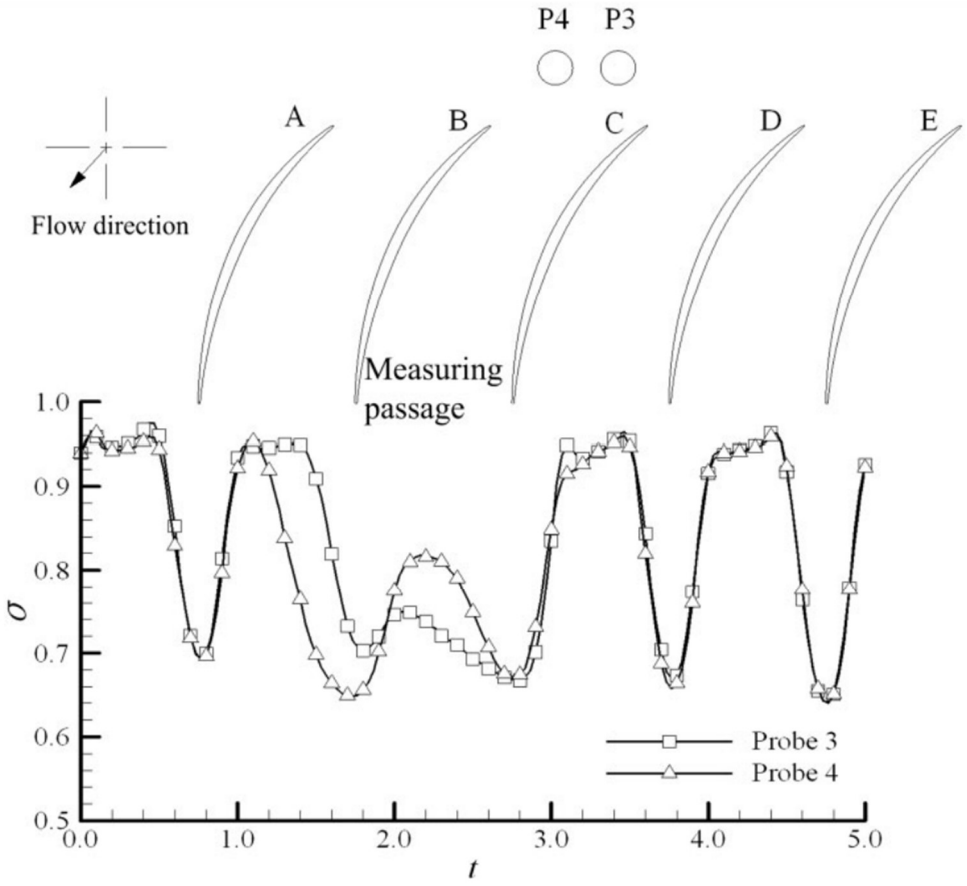

Figure 2.8 Probe positions upstream of the stator blade row and the wake loss distribution along the blade cascade with immersed probe (Xiang et al., 2016)

Lopes et al. (2022) found that the presence of the probe modifies the pitchwise distribution of aerodynamic quantities at the endwall locations. However, the spanwise variation of the pitchwise averaged quantities is reduced.

Ma et al. (2014) analysed the effect of the probe and stem blockage on the spanwise flow measurements in a low-speed compressor environment. The authors report that the high blockage from the holding stem caused radial flow redistribution downwards in the hub, which in turn caused a reduction of over 10% in measured total pressure in the upper 20% of the span, and a change of up to 5° in the flow angle. In Figure 2.9 the flow angle (yaw) and total pressure distributions are shown. However, the stem diameter to pitch ratio was over 20% and the probe diameter was more than 5%, and for such a large stem the blockage effect even in the low-speed environment was well pronounced. The probe immersion also caused a reduction of over

10% in compressor mass flow rate. This level of deviation makes it hard to correct for, therefore an effort should be made to reduce the geometrical blockage of the measuring structure.

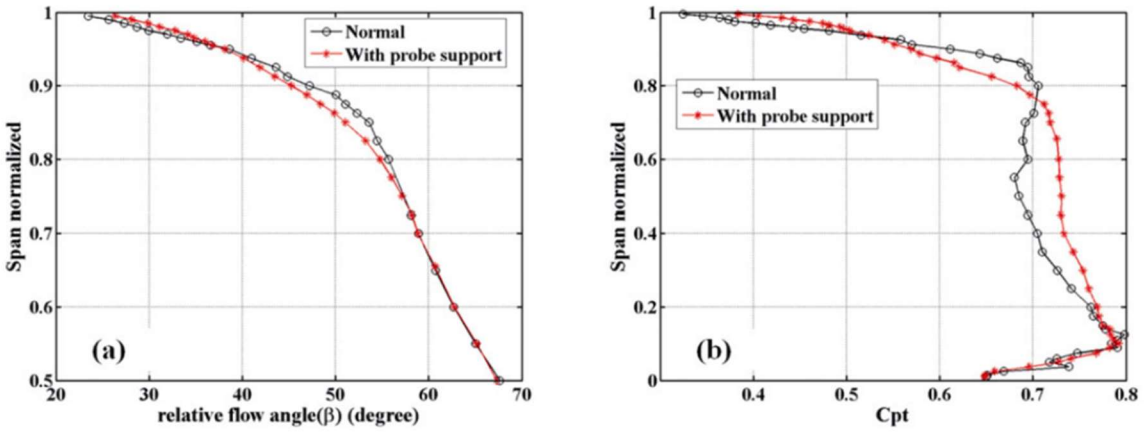

Figure 2.9 Radial distributions of flow parameters downstream of the rotor in a low-speed research compressor: flow angle (a) and total pressure (b) (Ma et al., 2014)

When measuring downstream of rotating blades, the flow is treated as circumferentially averaged. Coldrick et al. (2004b) explored the unsteadiness effect on the probe measurements. Figure 2.10 shows the computational domain for steady and unsteady calculations, and Figure 2.11 shows the time variation of the measured angle. Authors report a change of over two degrees in the averaged measured flow angle compared to the undisturbed flow value. The difference in total pressure measurements was less than 0.4% of the dynamic head; in practice that would fall within the measurement uncertainty. Important conclusions from this paper are that a steady state disturbance effect is responsible for the majority of contamination of probe measurements, and that the pressure gradient in the stator passage does not impart any significant error into the measurements.

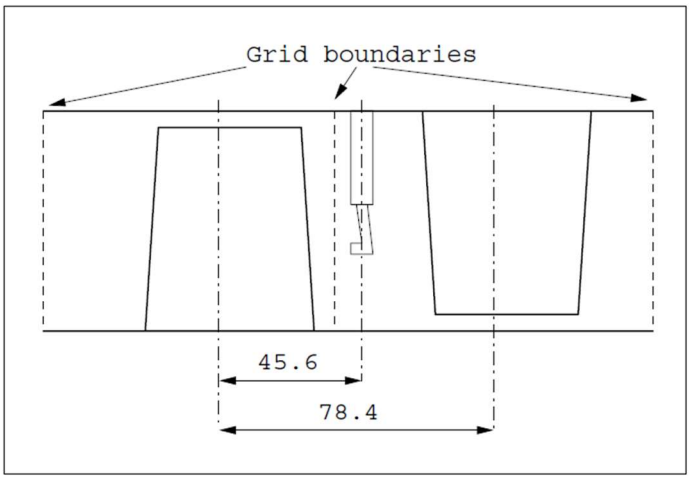

Figure 2.10 Rotor-stator-probe domain for estimation of the probe measurements downstream of compressor rotor (Coldrick et al., 2004b)

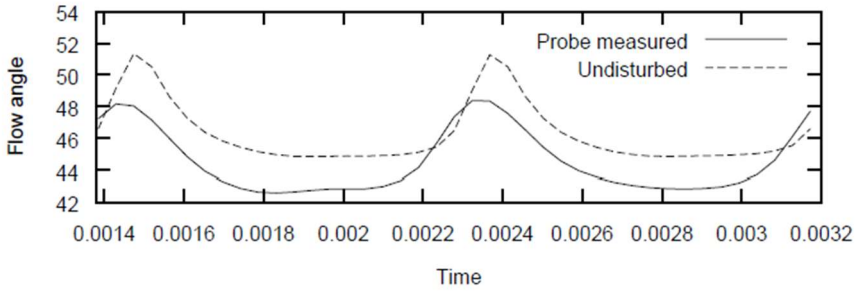

Figure 2.11 Variation of flow angle with time during unsteady calculations (Coldrick et al., 2004b)

2.2.3 Uncertainties when measuring downstream of the stator blade row

Sanders et al. (2017) provided a detailed numerical study on the intrusive influence of the five-hole pressure probe in a high-speed compressor environment. They found that the values measured by pressure probe traverse behind stator vanes do not always accurately represent the undisturbed flow field, and the maximum numerically estimated differences were −3% for the average Mach number and ±0.9° when measuring the flow angle.

For cascade measurements downstream of a set of blades, Sieverding (1993) suggests that the best solution to the blockage problem is to position the measuring head on a sting far upstream of the stem. This sting then moves the measuring probe head away from the stem blockage effects. In an axial turbomachine this is not possible, firstly due to the limited axial

space available and secondly the problems of fitting a traversing probe of the required length. Therefore, blockage effects give rise to velocity biasing, the magnitude of which depends on the measuring arrangement. With the probe moves radially, the blockage varies with immersion depth as the flow can pass underneath the probe.

When the probe is measuring in proximity to the trailing edges, it acts not only as a blockage to the flow, but might also deflect the flow towards the wake, thus changing the flow direction and speed. Hoenen et al. (2012) took PIV measurements of the flow around the probe in such conditions. In Figure 2.12 the nozzle effect and the difference in velocity vectors are shown as a result of the PIV comparison. The authors claim that when the probe is placed away from the trailing edge the flow field below the probe remains undisturbed by any influence from the probe itself. When the probe head approaches the trailing edge region, first interactions appear. The applied corrections near the wake region changed the measured Mach number by 62.24% and the flow angle measurements were corrected by over 30%. As a result, the pitchwise profiles fell in good agreement with the PIV data, and the authors conclude that these corrections can be applied in the two-dimensional traversing of turbomachinery flows. However, it is not said how the variations in blade geometry and flow conditions might change the amount of required correction, or how to calculate the correction for a specific case.

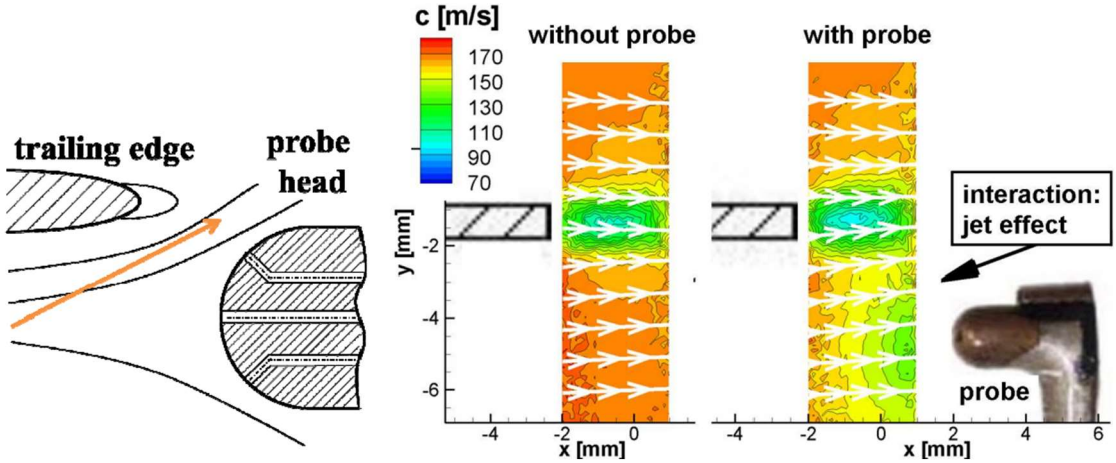

(a) (b)

Figure 2.12 Nozzle effect (a) and jet effect (b) between the probe head and trailing edge (Hoenen et al., 2012)

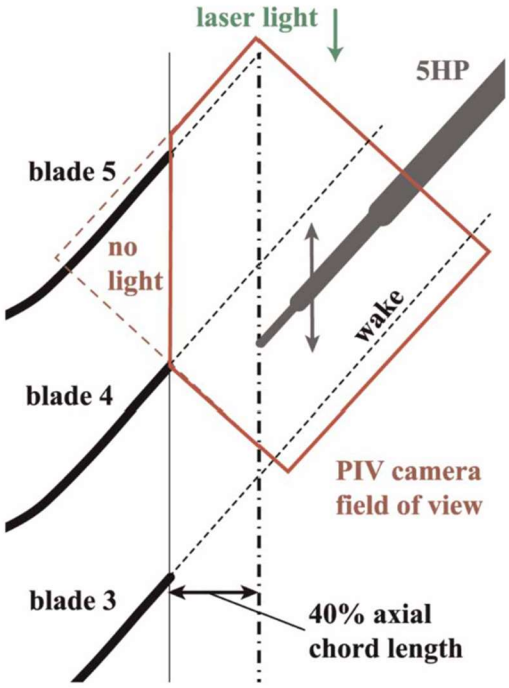

Figure 2.13 Experimental setup of a five-hole probe traverse and PIV measurements downstream of turbine cascade (Borner et al., 2018)

Borner et al. (2018) studied the probe measurements of high Mach number flows downstream of turbine nozzles. The setup is shown in Figure 2.13; it is close to the one from Sieverding (1993) and the probe is placed on the stem oriented along the flow with the holding stem far downstream. The differences between the flow field with the probe and the undisturbed flow field are shown in Figure 2.14; the authors discovered that for a given configuration the variations in the Mach number can exceed ±5% from the undisturbed flow.

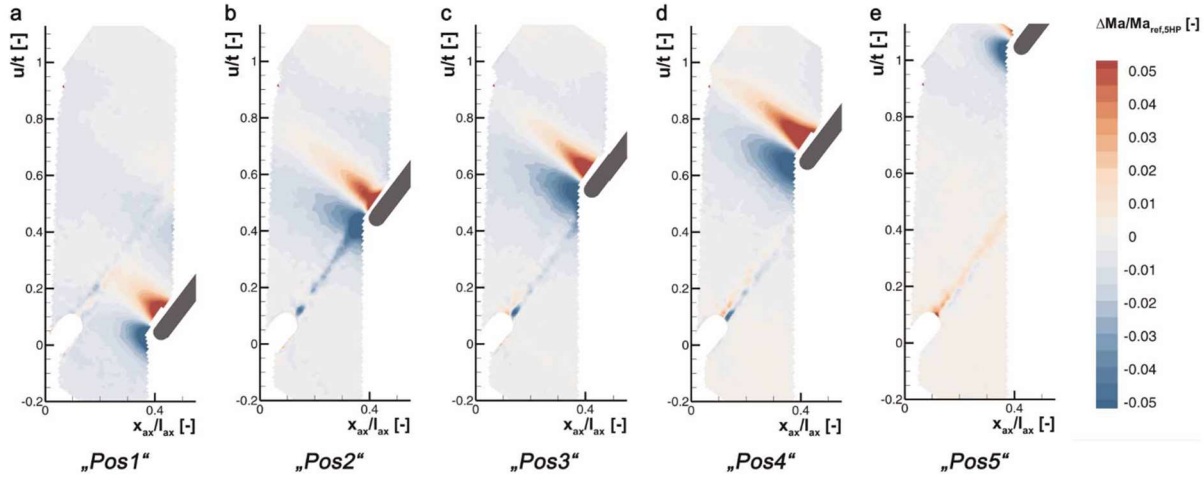

Figure 2.14 Normalised Mach number differences between the clean flow and the one with the five-hole probe, obtained by PIV measurements in a high-Mach-number subsonic flow (Borner et al., 2018)

2.2.4 Summary on the probe measurements in a constrained environment

To conclude, a flow field distortion, caused by the probe placed in turbomachinery flows is widely explored and well-reported in the literature. However, few authors report on how this distortion affects the measurements of the probe itself. In most cases, the simulations or experiments were carried out for a particular configuration and no information in the open literature was found on the parametrisation of the probe measurements in a wider design space and at various flow conditions. In addition, only a few parametrised recommendations were found for the probe location both upstream and downstream of the stationary blade row, and the impact of all the flow mechanisms at such locations.

2.3 Corrections to the flow field measurements

Bailey et al. (2013) report an extensive collection of known correction approaches for measuring boundary layer flows with Pitot tubes. The use of a Pitot tube in a shear flow introduces additional adverse effects through nonlinear averaging of the pressure variation

across the probe face and asymmetric deflection of the streamlines. The effect of spatial averaging across the face of the probe is usually small compared to that of asymmetric streamline deflection, thus a velocity gradient correction typically only compensates for the higher velocity streamlines deflecting towards the tube. The proposed correction accounted for the shear in the boundary layer and turbulence intensity, measured with the hot-wire anemometry. The authors achieved a good agreement within a distance of under $y+ < 300$. However, the experience published by Bailey et al. is related to a zero-pressure-gradient flat plate boundary layer and although potentially applicable to other simple turbulent wall-bounded flows, the observations cannot be extended to more complex flows, such as those found in strong adverse pressure gradients or three-dimensional boundary layers. Additionally, for real turbomachinery applications, detailed measurements of the boundary layers, especially the hot-wire anemometry, are not feasible.

Coldrick et al. (2003a) studied the flow around the probe when positioned in proximity to the stator leading edge plane near the middle pitch and how this flow is changed compared to the undisturbed case (Figure 2.15). They concluded that the presence of the probe caused an increase in pressure and a decrease in speed in the region between the blade and the probe, leading to a shift in the stagnation point and an erroneous reading on the adjacent probe pressure port (see Figure 2.16). The addition of the measuring uncertainty led to approximately 3.3° of total uncertainty. The authors proposed to resolve this issue by moving the probe away from the centre of the passage or to a lesser degree by using a smaller probe. Later in his thesis, Coldrick (2003b) also simulated a smaller diameter probe, which, for a high-speed environment, demonstrated only a ‘minimal improvement’. The author also indicated a lower pitch angle sensitivity range compared to the freestream calibration of the probe. Coldrick then compared the simulation and experimental data with the design intent to see if the probe blockage effect was consistent.

It is also unclear how the probe location in the circumferential direction can affect the probe measurements and to what extent the probe shall be moved away from the centre of the passage to resolve the issue of erroneous angular measurements.

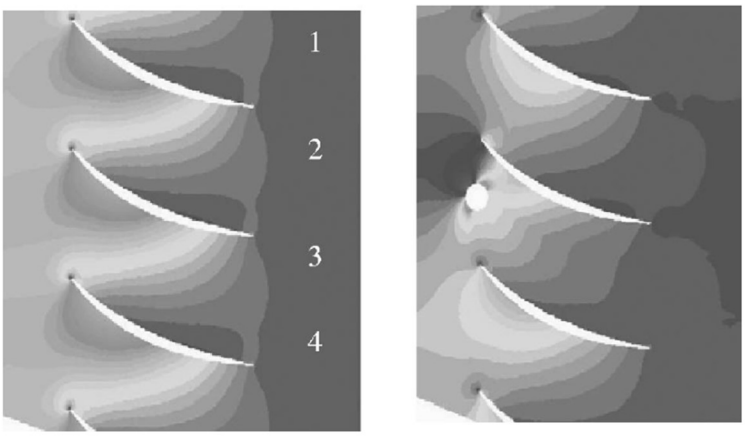

Figure 2.15 An undisturbed flow field in a stator blade row (left) and the flow with the immersed probe (right) (Coldrick et al., 2003)

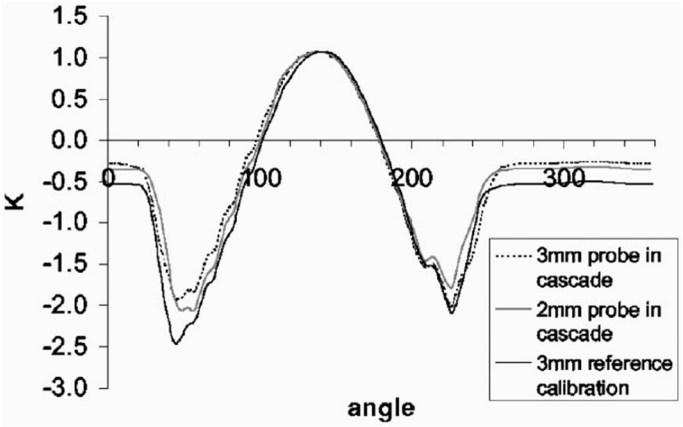

Figure 2.16 Pressure coefficient (K) distribution around the probe at freestream calibration and when placed upstream of the stator blade row (Coldrick et al., 2003)

Chernoray (2008) reported an overestimation of measured flow angles downstream of the turbine outlet guide vane in the wake region. This is due to the finite-size effects of the five-hole probe. The values were compared with reference values from hot-wire anemometry at the same plane. In Figure 2.17 raw measurements and corrected results are compared with the reference. In this case, the corrections reached up to 10% of the measured values of the circumferential to axial velocity ratio.

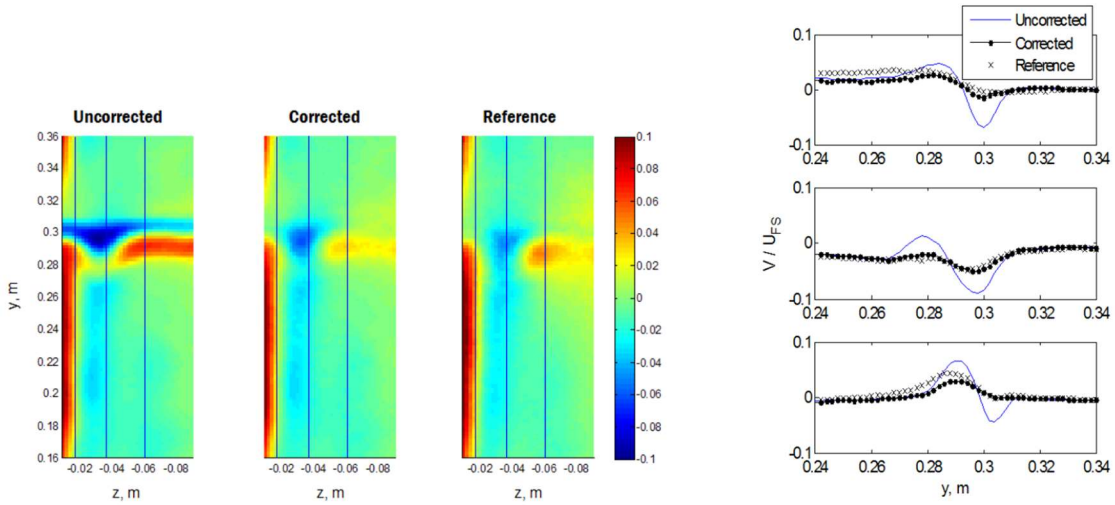

Figure 2.17 Comparisons of hot-wire and five-hole probe measurements of a vertical velocity with and without velocity corrections (Chernoray, 2008)

To conclude, CFD methods have been used in the past to estimate the required correction values for finite-size probe measurements. For many applications, the local flow calculations were found to be sufficient to correct the measurements; however, in some cases the magnitude of corrections was significant. Up to a 60% difference in measured pressures was reported and for such large values it is unlikely that these corrections can be universally applied to other test cases. In addition, the available literature lacks universal dependencies for a wide range of design and flow parameters. Typically, the corrections in the literature only account for a subset of physical mechanisms causing the measurement errors.

2.4 Reconstruction of the flow field based on limited measurements

When experimental results appear only from a multistage compressor setup, it is crucial to carry as many measurements as technically possible along the whole operating range of the compressor. In high-speed turbomachinery, both for laboratory and industrial applications, the range of available locations for measuring the flow is limited by multiple factors. Therefore, to consider a fuller picture of the complex flow, an effort is required to couple the limited

experimental measurements with a data assimilation framework compensating for the limited information available. Lou and Key, 2020 and Lou, Matthews, Iii, and Key, 2020 implemented an optimisation algorithm to select optimal probe placing, followed by a multi-wavelet approximation to reconstruct the circumferential flow of the machine, avoiding the common usage of averaging rake measurements to evaluate performance. Seshadri et al., 2020 applied a Bayesian treatment to engine experimental data in the form of Gaussian processes (GP) and decomposed the posterior uncertainty into the error of the measurements and insufficient sampling, leading to optimal sensor placement.

Data assimilation techniques can benefit the entire field of fluid mechanics, even in fundamental research (see, for example, Clark Di Leoni et al., 2020), by tackling two differing problems: the accurately measured experimental data is limited in space and time, and a computational simulation, due to numerical discretisation or inaccurate definition on boundary conditions, may not represent the state of the real flow (Hayase, 2015).

2.5 Research questions

The combined body of literature has raised a number of key questions. These are summarised below and will be answered in the results chapters of this thesis:

1. It is known that the presence of the probe disturbs the flow field in the blade channel, and the probe readings can no longer be processed with the freestream calibration characteristics when measuring at high speeds in confined inter-blade-row space. But it is not clear how the key geometrical and flow parameters affect the flow field interaction and the measurement uncertainties. This is studied in Chapter 4 for a simplified case of the probe in a rectangular channel, and then in Chapters 5 and 6 for probe measurements upstream and downstream of the stator blade passage.
2. Since it is not always possible to place the probe in the middle of the blade channel, and the probe's pitchwise position might vary as the probe moves along the span, the probe might approach the blade walls or regions of high vorticity. It is necessary to know the physical limitations for the probe to measure reliably, and in which conditions such measurements can be corrected to account for the flow field interaction. In Chapter

5 the limitations and possible corrections are considered for measurements upstream of the stator, and in Chapter 6 the same is done for the measurements downstream.

3. When only a few measurements along the circumference of the blade row are known it is important to obtain a fuller picture of the flow. The CFD methods have repeatedly been used to reconstruct the flow field with the use of limited point data. However, it is important to correct the measured values before such reconstruction. A two-step procedure was proposed in Chapter 5 and then later applied to the experimental results in Chapter 7.
4. Measurement corrections can shift the experimental results by a significant margin, and it is assumed that the direction of the shift is always towards the correct values of the undisturbed flow. This, however, must be independently verified based on fundamental physical principles or other measurements before the data can be used by the designer. Chapter 7 presents a procedure the researcher can follow to control the consistency of the measurements before and after the corrections. It also shows useful information that can be obtained from the spanwise traversing of the industrial compressor.
5. Finally, experimental and computational data may have large uncertainties, and in some places in the compressor the measurements are hardly possible. This raises the question of how the combination of the two sources can be used to obtain fuller and more reliable information about the compressor's flow physics, based on the low-uncertainty parameters from both sources and the physical interdependencies of these two groups.

Chapter 3 Methods

The aim of the present work is to investigate whether the measurements in a confined inter-blade-row space are equal to the values of the undisturbed flow at a location of the probe and if not, then to identify the mechanisms causing the deviations and explain how these measurements can be corrected. This work explores advantages of both computational and experimental methods and gives an insight into how they can be combined in multistage compressor research so that the sources of the highest uncertainties of both methods can be compensated for. In this chapter, the experimental setup of the multistage compressor is presented first to define geometrical parameters and limitations of the real environment. Then the computational model of the whole compressor and the stator blades of interest with the immersed probe are discussed.

3.1 Experimental setup

Experimental data presented in this thesis was obtained from the industrial gas turbine on-site test facility in one of the natural gas transportation pipelines in West Siberia. The traversing gear was designed and manufactured at the Whittle laboratory in Cambridge.

This section serves three aims. First, it provides a description of the experimental rig and the experimental techniques used. The geometrical data and operating conditions from this description will be used in Chapters 4–7 for the computational research on the measurement corrections. Second, this section shows that the measurement uncertainties are at the minimum feasible level, considering the complexity of the experimental work on the real gas turbine engine. This is important because during the processing of preliminary results the inconsistencies were found to be up to 5° in measured angles and over 30% in pressure measurements, which could not be explained by the setup problems. This contradiction has been the basis for full-scale research on the measurement uncertainties, which then resulted in

this thesis. Finally, this section is aimed to be of use to other experimental engineers aiming to design similar setups.

3.1.1 Compressor of interest

Experimental work on the gas turbine engine of interest was performed during its operation on site. This is because the capital cost and the timeline for the subscale testing of the initial and the modernised design were found to be prohibitive, especially for a retrofit program. As a result, one of the representative engines of the fleet was chosen for the pilot trials, and additional instrumentation was set up on the engine for a detailed experimental study.

Figure 3.1 shows a cross-section of the compressor with the planes where the holes in the casing were drilled. Each plane has four holes drilled in the upper half of the compressor casing. The circumferential location of these holes was not always optimal from the measurement perspective due to space limitations on the outer casing caused by structural ribs, bleeding pipes and auxiliary mechanisms. The locations were also set to account for the differing number of blades between the datum and modernised blade sets.

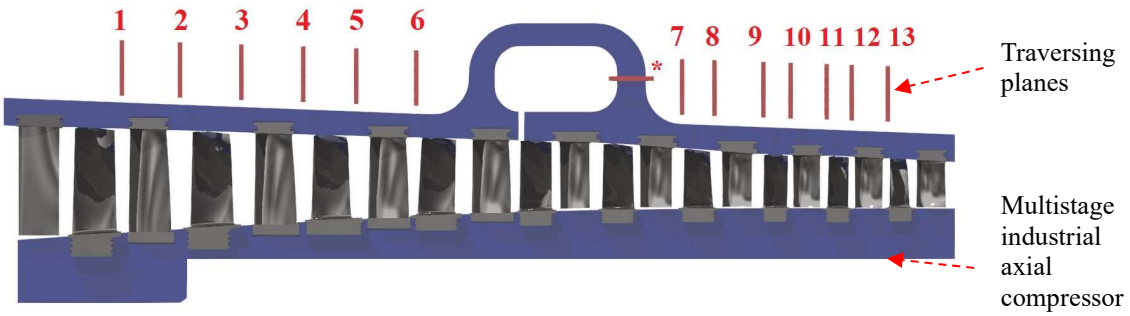

Figure 3.1 A cross-section of the axial compressor with axial locations where the traversing has been performed

There were 11 operating points where only the casing pressures were measured and three operating points with full traversing. A compressor operating line is shown in Figure 3.2. The traversing was carried out at 0.86, 0.92 and 0.98 of the compressor corrected design speed. This covered a wide range of operating conditions for the frontal stages including those where the first stage was working in proximity to its stability limit.

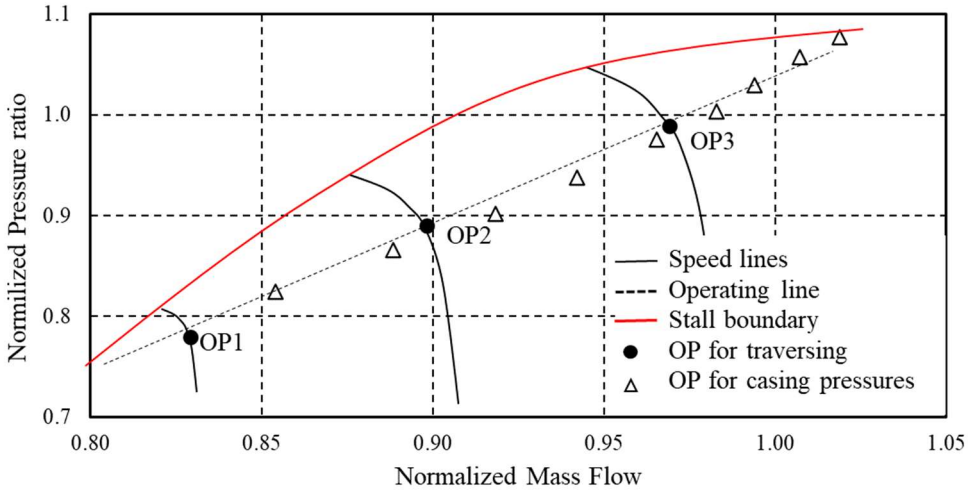

Figure 3.2 Operating line of the axial compressor with the points where the full traversing was performed

In Figure 3.3 the experimental rig comprises an industrial gas turbine for mechanical drive, installed in a workshop with all the necessary auxiliaries and control systems, which is typical for this kind of application. The turbine consists of two modules: the high-pressure turbine (HPT) and the power turbine (PT). This split allows the axial compressor to have variable rotational speed along the operating line. Traditionally, compressor parameters are measured upstream and downstream of the compressor, in the inlet and outlet ducts, and these values are treated as mass flow averaged. The gas turbine engine works in a recuperative cycle in which the air after the compressor is heated up using the heat of the turbine exhaust gases. From an experimental perspective, this engine type allows better access to the compressor's exhaust air as it is taken away from the machine to a free-standing recuperator module (see Figure 3.3 points 4 and 5), therefore the parameters of the exit air can be measured with better precision compared to cases in which the compressor exit is integrated with a combustor.

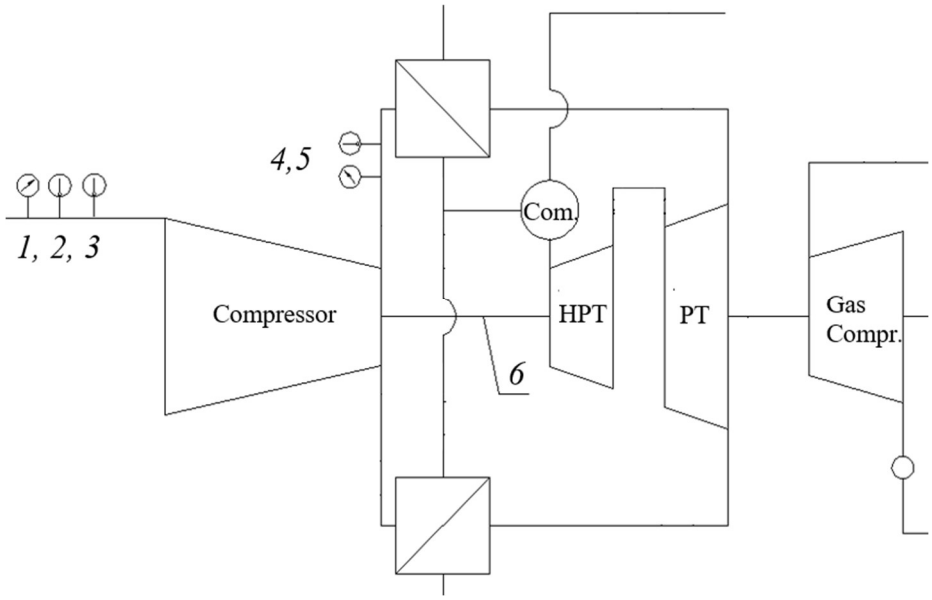

Figure 3.3 An industrial gas turbine for mechanical drive with cycle measurements

The axial compressor of interest is a 10-stage subsonic industrial compressor with moderate stage loading, representative of modern industrial compressors. The stage loading coefficient for the mid-span is 0.32-0.35. More parameters are shown in Table 3.1.

Table 3.1 Key geometrical parameters of the compressor

Parameter	Value
Number of stages	10
Rotor 1 tip Mach number	0.8
Rotor 1 tip speed (m/s)	240
IGV flow swirl at mid-span	35°
Blade's inlet angles	35–60°
Blade's outlet angles	10–30°
Blade axial chord at mid-span	95mm (first rotor), 70mm (last stator)
Pitch-to-chord ratio at mid-span	0.9 (first rotor), 0.7 (last stator)
Mid-height flow coefficient	0.5–0.6
Mid-height loading coefficient	0.32–0.35
Mid-height design reaction	0.55–0.65
Stator blades shrouded at	Stages 1–4
Swirl distribution	1–4: constant reaction, 5–10: free-vortex
Meridional contours	1–5: constant mid diameter, 6–10: constant hub diameter
Axial gaps	0.2–0.3 of blade chords
Radial gaps (% of blade height)	First stage: 0.5%, Last stages: 1.2%
Blade airfoils	Customised, originated from NACA-65 C_{max} = 7–12% of the cord length LE radius 3–5% of the cord Max thickness at 40% of the cord Max camber at 50% of the cord

3.1.2 Traversing gear

The traversing gear was designed as two independent plug-in modules, which were moved between sections of the compressor during the experiments. These are shown in Figure 3.4 being installed on the compressor casing. Each hole in the compressor was equipped with a valve and a fixture on top of it. The valve fixtures at each measurement plane were aligned against each other, so that when the traversing module was clamped to the valve, its orientation against the compressor axis of rotation was definite. Two fixtures at each measurement plane were sufficient to get the traversing orientation.

Figure 3.4 also shows spatial constraints outside the compressor casing. The presence of structural ribs, blow off valves, bleeding slots and pipes, heating air pipes and auxiliaries was significantly limiting the available space for valve positioning.

The reasons for independent modules rather than pre-set and pre-aligned traverses at each section were:

- Safety regulations prescribed not to have any obstacles on the engine casing during start-up.
- The low-pressure blow-off valves were releasing air in proximity to the casing wall, so the traversing tools could be damaged.
- The casing wall temperature exceeded 200° Celsius, and permanent contact with the wall would cause overheating of the traversing module.
- Thermal expansion of the casing required additional control of the traverse alignment before each measurement, so the initial traverse set-up on the cold machine would not save machine operating time required for testing.
- Each measurement must be monitored for accidents by an operator, and the space on the machine was not sufficient to operate more than two traverses simultaneously.
- The amount of labour and funding for each traverse was limited.

Precise drilling of the holes allowed for the traversing gear to be aligned against two of the holes at the same axial plane. The linear distance between the holes was more than 300 millimetres, and the total play in the alignment fixture was less than 0.2mm. This defined the angular orientation of the tower with a precision well within ±0.05°.

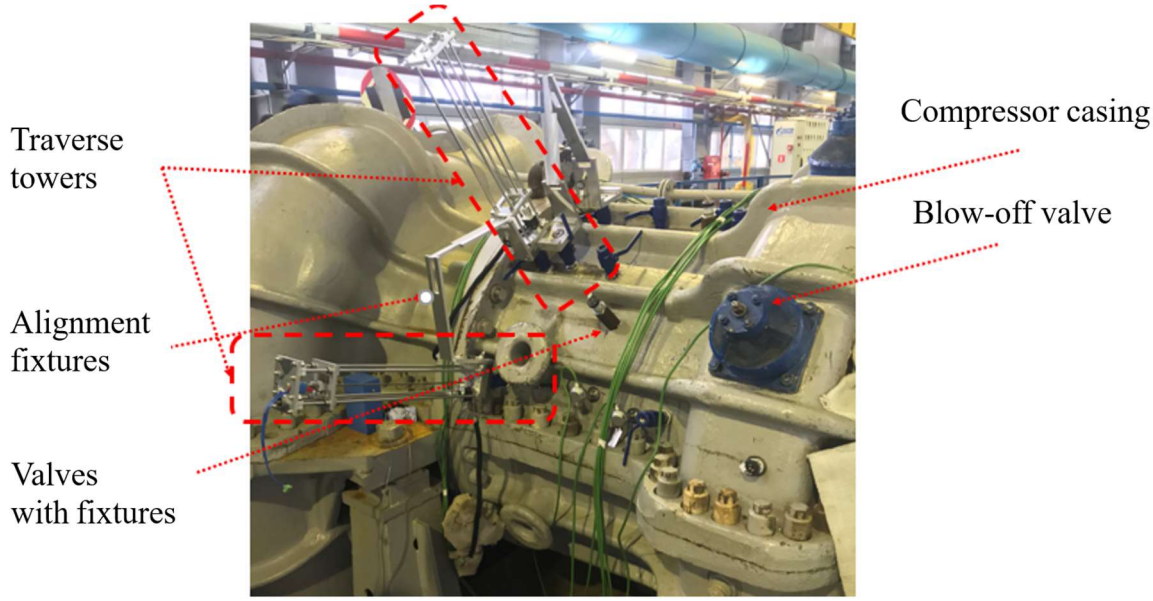

Figure 3.4 Traversing gear installed on the compressor

The holes are shown in Figure 3.5; they were drilled on the double-gantry milling centre, where special attention was been paid to their alignment, so that each group of four holes lay in one plane, perpendicular to the axis of rotation, and the axis of each hole was oriented in the radial direction. The circumferential position of the holes was chosen with respect to all the positioning limitations on the inner and outer surfaces of the casing and also to account for a change in blade count for the new blade design so that the holes could be used for future traversing.

The uncertainty of the holes' location was ±0.1mm, and the deviation from a radial angle was less than one minute of a degree. The inner surfaces of the holes were reamed with a diameter of 5.05–5.10mm, which together with the holes' depth of 60–80mm allowed for maximum rigidity of the traverse stem. These holes were also used to measure the static pressure on the casing surfaces.

The setup uncertainty of the gear was calculated to be well within 0.5° so the major source of uncertainty would be caused by the probe calibration. The resolution of the stepper motor allowed the probe position to be within ±0.01 mm, and the spatial resolution during the traversing was 0.1mm near the end walls and 5–20 mm in the middle span.

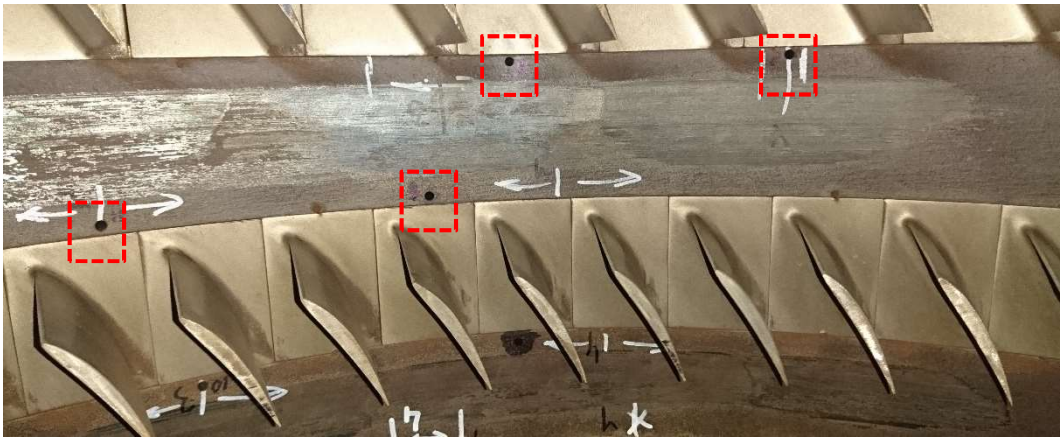

Figure 3.5 Compressor traversing locations between the blade rows

3.1.3 Probe and stem assembly

One of the key elements that distinguish the traversing solution in this thesis from others reported in the open literature is the design of the probe and the holding stem. It allowed the probe to be immersed to a distance of over 40 stem diameters—over 220 mm immersion for a 5mm stem. Normally, for high-speed laboratory traversing this ratio does not exceed 5–10. A stem of less than 5% of the blade pitch was used for minimum possible blockage in the blade passage, and it had a constant diameter along its length (without thickening the stem away from the probe) to minimise radial flow redistribution when immersed.

In Figure 3.6 this stem is shown in an assembly with the combined three-hole probe, which was also specially developed for this project.

The stem is a solid cylinder made out of hardened stainless steel with two side slots to accommodate hypodermic tubes and wires. The slot dimensions were optimised so that they were always in the wake region of a cylinder (considered for turbulent boundary layer) and at the same time, the contact area between the stem and the casing hole was maximised to reduce the contact stresses. The probe had a threaded end which was screwed into the stem; the hypodermic tubes were laid towards the outer corner slots on the stem.

Each probe was aligned with a zero mark on the other end of the stem using a fixture, and the orientation was then checked with the laser pointer. The remaining angular offset was stored in the calibration file, so the uncertainty in the angular position of the probe was within 10

minutes of a degree. The axial gap between the thread and the stem was filled with high-temperature epoxy resin. The same was used as a filler and protection for the accelerometer, its wires, and the tubes.

The three pneumatic holes (1) were accompanied by the stagnation chamber (2) for temperature measurements. Due to the setup problems, the temperature was only measured in a few sections, therefore it was impossible to judge the validity of the temperature measurements. However, because of the low level of ventilation in this chamber, the pressure in it for most of the cases was within 2% away from the total pressure of the flow in the ±20° yaw range. This was found to be a useful parameter in controlling the consistency of the other three holes' measurements.

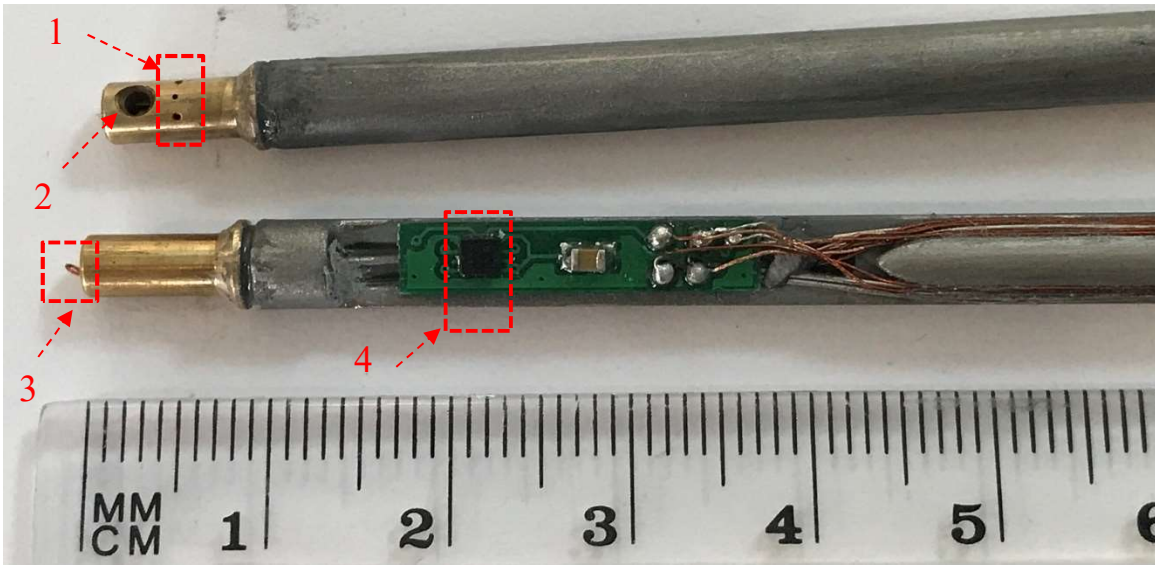

Figure 3.6 A three-hole pneumatic probe and a holding stem: three-hole cylindrical probe (1), stagnation chamber for a thermocouple (2), contact wire for safety (3), accelerometer (4)—all before covering with epoxy resin

The key requirement for industrial testing was the safety of the probe. To avoid contact with the rotating hub and in the event of probe damage the contact wire was set at the very tip of the probe. It was designed as a closed loop, and in the event of impact the resistance of the loop, measured by the control board, initiated the emergency extraction of the stem.

At the back of the stem, a temperature-resistant miniature accelerometer was installed to study the stem vibration and deviation from its radial position. The accelerometer was also used during calibration when the stem was allowed to oscillate with significant magnitude, and the dynamic calibration performance of the probe was studied.

3.1.4 Probe design

A cylindrical probe was used in the current work for two reasons: the limited size of the hole in the casing and the uniformity of the pressure field around the probe regardless of its orientation. The first factor required a probe to fit into a hole in the casing which was 5 mm in diameter and over 80 mm deep. A miniature cobra probe that would fit into such a hole would not be able to bear an aerodynamic load. The cylindrical shape was preferred to the wedge type to avoid an additional degree of freedom in simulations and corrections, which is the wedge orientation against the blades. When the probe was travelling along the span, its angular orientation was fixed, therefore, its relative angular orientation to the blade passage could vary. When the probe is cylindrical the flow around it does not depend on its angular orientation. Therefore, when the measurements of the simulated probe are considered, they can be based on the wall pressures at desired locations on the cylindrical surface, which can easily be obtained. For a non-cylindrical shape, each orientation would require a new set of simulations. The probe dimensions are given in Table 3.2 in absolute values and those related to representative blade passage metrics.

Table 3.2 Probe dimensions

Parameter	Value	Relative value	Related to
Probe diameter	3.5 mm	4..8%	Blade pitch
Stem diameter	5 mm	6..11%	Blade pitch
Probe height	8 mm	4..10%	Blade span
Pressure holes	0.3 mm	8.6%	Probe diameter
Holes distance from the tip	4.5 mm	56%	Probe height
Angle between the holes		±42°	–

Multiple optimisation problems were solved during the probe design. One was the distance between the pressure holes and the probe tip, illustrated in Figure 3.7 in terms of the pressure coefficient:

$$C_P = \frac{P - P_{stat_{inlet}}}{P_{0_{inlet}} - P_{stat_{inl}}} \quad (3.1)$$

Where P is pressure at the probe surface. Near the probe tip, the flow goes around the cylinder as well as under it, so the pressure distribution around the cylinder near the probe tip is different from a two-dimensional flow. To avoid the tip flow effect on the pressure distributions, the distance from the tip is chosen to be 1.5 probe diameters.

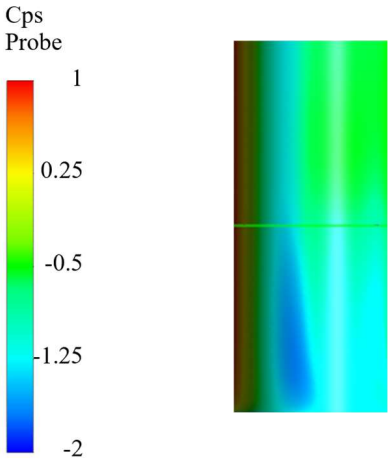

Figure 3.7 C_p distributions on the probe surface with the tip end at the bottom with the flow coming from the left

3.1.5 Data acquisition and control system

A PCB board was developed for the experimental campaign. It accommodated pressure sensors, a thermocouple board, stepper motor controls, data acquisition, storage, and communication units. This allowed for a traverse tower being fully portable, with a single connection to the electric socket, and two connections for the reference pressures. This significantly improved the usability of the module and settling time at each location.

The number of points expected to be measured at each plane was between 40 and 200. Each measurement required waiting for probe readings to settle, so that a single reading is within sensor uncertainty away from the averaged value. To minimise the settling time, the pressure sensors were placed on the traversing tower, in particular, on the moving part of the tower, which held the stem with the probe. Figure 3.8 shows that settling time has been reduced down to less than 1.8 seconds, compared to more than 5 seconds when the sensors were placed on top of the tower. Further reduction was achieved by reducing the tubing inner diameters between the probe stem and the sensors from 1 mm to 0.25 mm, which resulted in a settling time of less than 1.2 seconds. As a result, traversing at one location required less than 5 minutes for the whole span, including homing. The control board and the pressure connectors were isolated from the metallic surfaces of the gas turbine and an artificial cooling system with a Peltier element was used.

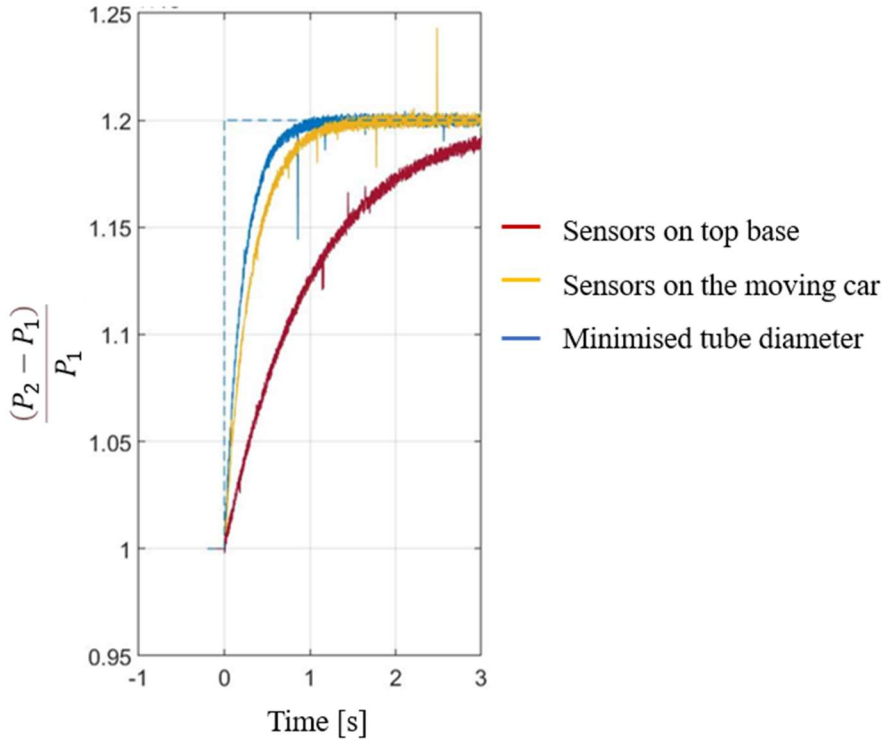

Figure 3.8 Measured step function response of pneumatic probe with varied tube configuration and inner diameters of pneumatic tubing

Honeywell HSC gauge pressure transducers were used for pressure measurements. To optimise sensitivity of the sensors within a wide range of compressor parameters, one of the two sensor ports was connected to one of the holes on the compressor casing. The pressure in the hole was the static pressure at the compressor casing in the measurement plane of interest. Hence, the range of the pressure sensors was chosen to be enough to cover the dynamic head behind rotors, not the overall compressor pressure ratio. This allowed one order of magnitude improvement in measurement uncertainty. For measuring casing pressures, a 10-bar range was chosen for the sensors, whereas for the probe pressures the range was 0.6 bar. The discharge pressure at the compressor inlet was measured with a 160-mbar sensor.

Figure 3.9 shows the calibration map of the sensors along their range. They were calibrated with a Druck-460 pressure module. Altogether, 20 sensors were calibrated before and after the on-site testing. The two sets of points are shown for the two sensors with maximum and minimum offsets, and all other sensors lay in between the two sets. It can be seen that all the readings fell within a range of ±0.5% of the full-scale span (FSS). The repeatability of the readings for each sensor is within 0.1% FSS.

The calibration was also performed when the sensors and the board were placed in the insulated box with the thermostat and electric heater at 60° Celsius to account for the real operating conditions of the equipment. The shift in the calibration curve was within 0.2% FSS towards larger positive values.

The same calibration procedure was carried out after the experimental campaign; after more than 80 hours the sensors had been exposed to the operating environment (including waiting and troubleshooting time). The deviation from the initial curves was found to be within 0.1% FSS.

Sensor readings were then corrected in accordance with individual linear calibration functions (shown in lines in Figure 3.9). For example, when measuring a value of 20% of the FSS, the correction would be -0.18% and -0.21% of FSS for each of the two sensors. Each sensor was tracked during the campaign and calibration coefficients were applied accordingly. As a result, the initial sensor uncertainty claimed by the manufacturer was reduced by 80% compared to the datasheet and is expected to be within ±0.1% of the full span, or ±0.25% of the dynamic head downstream of the stators and half that downstream of the rotors.

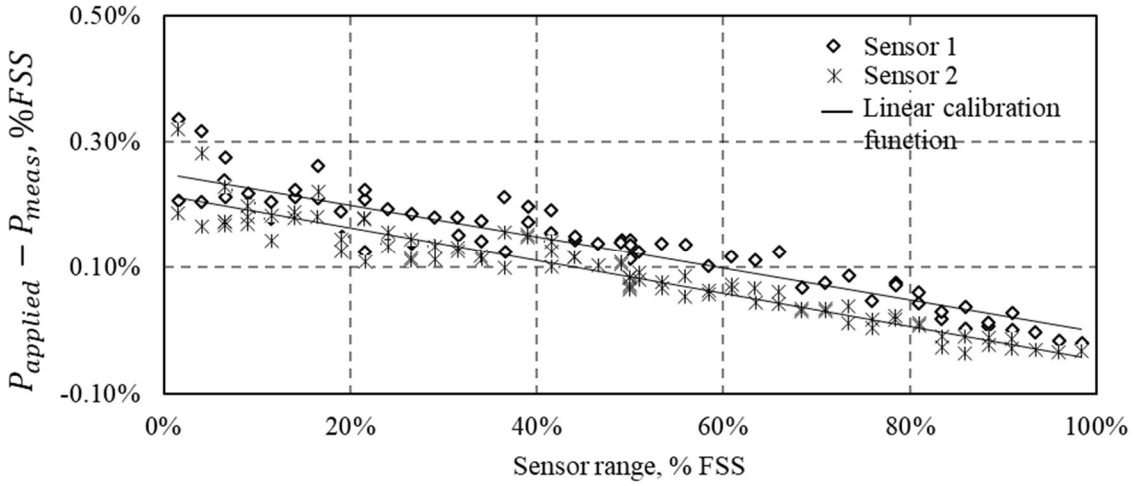

Figure 3.9 Pressure sensor calibration: difference between applied and measured pressures along the sensor's range: sensors with maximum and minimum offset

3.1.6 Probe calibration

For a high-speed probe calibration, a bespoke calibration tunnel was manufactured; it had two purposes. The first was to calibrate the probe at high flow Mach numbers up to 0.8. This required a uniform jet of the biggest possible diameter. The geometrical probe blockage ratio was 7% based on the probe and jet diameters. For reference, the low-speed calibration was performed at the Peregrine calibration tunnel with a blockage ratio of 1.75%.

The second purpose was to test the probe and the stem behaviour at aerodynamic loading at representative flow speeds and the maximum possible exposure to the flow, to simulate the probe immersion into the flow path. For this, a narrow rectangular channel was made, which was sufficient to place 120mm of the stem into the flow, while the distance from the clamping point to the probe tip was 220mm—the same distance as at the first measurement section. In this experiment, the rigidity of the stem was assessed, together with its deflection. In addition, the probe was calibrated with the oscillating stem.

The tunnel is shown in Figure 3.10. The air enters the chamber through convoluting pipes (1) or (2) and is sucked through the adjustable collector (6) by a high-pressure-ratio vacuum pump in the Whittle laboratory. Probe (3) is placed in the middle of the jet for calibration and

at the bottom of the calibration tunnel for the stress tests. The holding stem (4) is clamped in the fixture (5), where the stiffness of the connection is controlled by replaceable inserts.

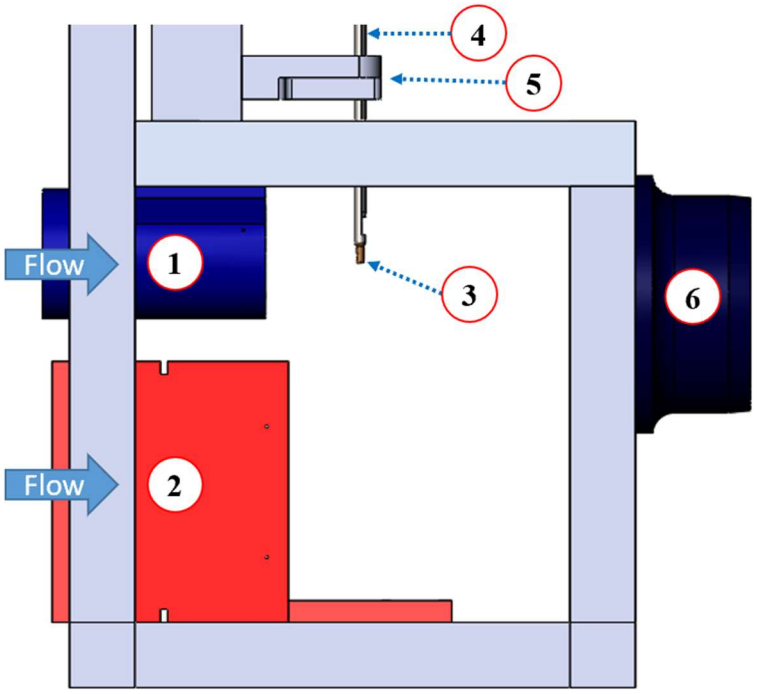

(a)

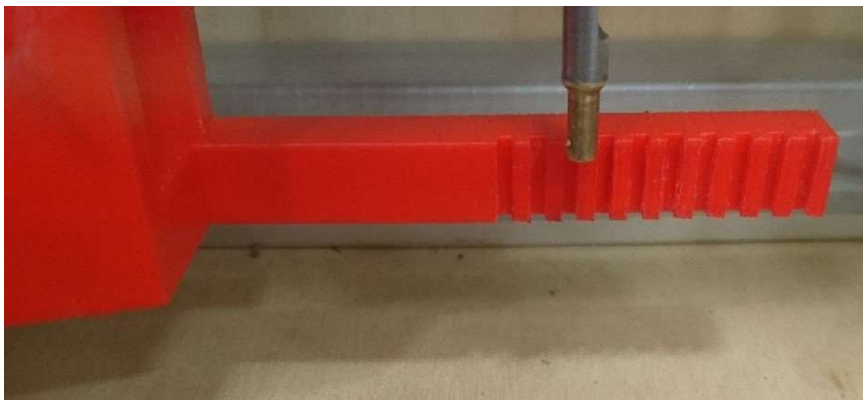

(b)

Figure 3.10 Traversing chamber for the high-speed probe calibration: general view (a) and the probe at vibration test (b)

A typical pressure distribution around a cylinder is shown in Figure 3.11. The probe has three holes on the cylindrical surface, and a stagnation chamber for the thermocouple, where

the pressure has also been measured. When the probe is rotating along its axis and is exposed to the freestream jet, the pressures measured at each of the three holes follow the sinusoidal shape with the offset in probe incidence angle according to the angular distance between the holes.

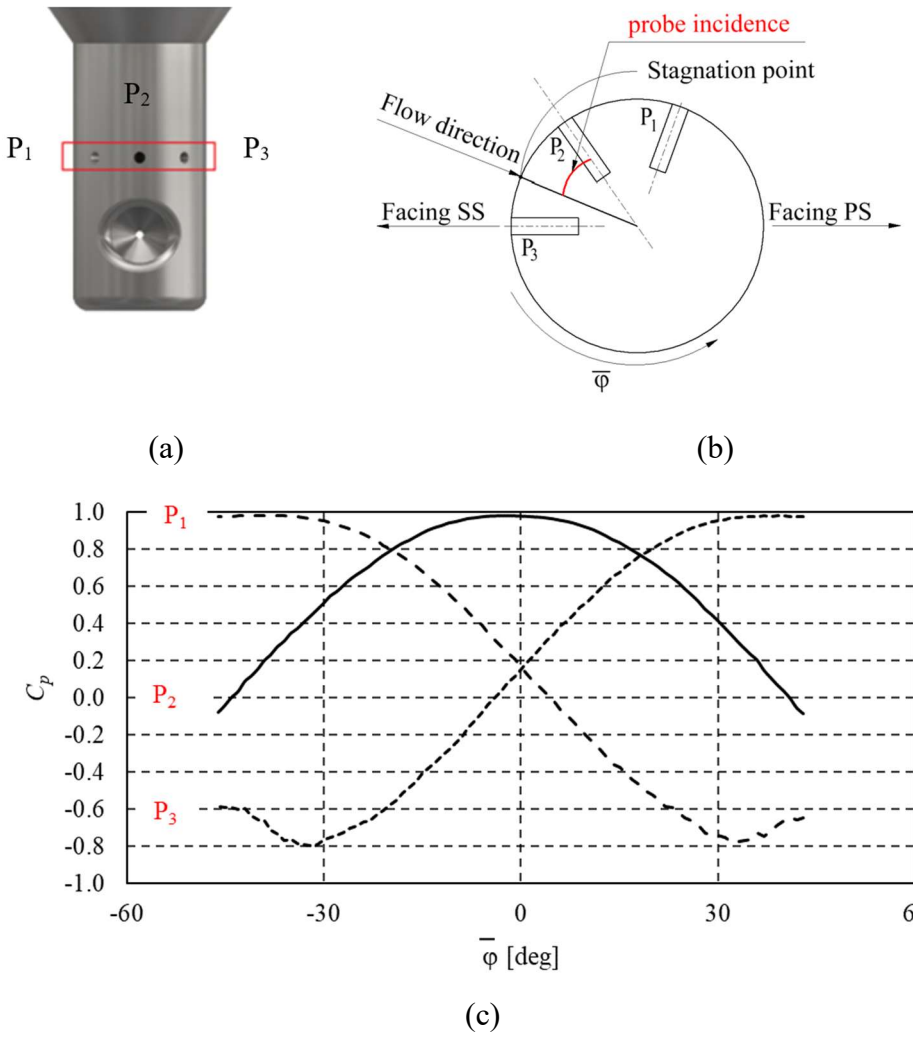

Figure 3.11 Overview of three pressure holes (a), explanation of probe incidence (b) and Cp measurements of the holes at variable probe incidence (c)

Three measured pressures can result in three flow parameters: flow angle (yaw), and total and static pressures. The coefficients for each pressure are given in Equations (3.2-(3.4.

$$C_{YAW} = \frac{P_1 - P_3}{P_2 - (P_1 + P_3)/2} \tag{3.2}$$

$$C_{TOTAL} = \frac{P_2 - (P_1 + P_3)/2}{P_0 - (P_1 + P_3)/2} \tag{3.3}$$

$$C_{STAT} = \frac{(P_1 + P_3)/2 - P_{stat}}{P_0 - P_{stat}} \tag{3.4}$$

Where P_1, P_2, P_3 are pressures measured at holes 1, 2, and 3 respectively

The calibration was performed for the flow Mach number at a range of 0.3–0.85. Typical distributions of the calibration coefficients are shown in Figure 3.12 for the flow Mach number of 0.4.

The calibration tunnel allowed choking conditions of the flow to be achieved, so that the probe could be calibrated along the whole range of operating Mach numbers. Figure 3.13 (a) shows the example of static pressure coefficient calibration for three Mach numbers. The calibration was carried out with an increment of 0.1 in the Mach number.

Figure 3.13 (b) shows the distribution of $C_{p_{probe}}$ values. For the sake of clarity in this thesis two types of C_p values are used: $C_{p_{probe}}$ and $C_{p_{flow}}$:

$$C_{p_{probe}} = \frac{(P_{probe\,surface} - P_{st,inlet})}{(P_{0,inlet} - P_{st,inlet})} \tag{3.5}$$

$$C_{p_{flow}} = \frac{(P - P_{st,inlet})}{(P_{0,mid} - P_{st,inlet})} \tag{3.6}$$

Both parameters have the same physical meaning; however, the first one is related to the pressures on the probe surface. This is used to study probe calibration maps and its changes under a range of operating conditions: when the probe operates in the confined channel, the pressure distributions can become asymmetric, changing the gradient or character of the line, thus indicating changes in the boundary layer regime, flow separation point and other features. The second parameter, $C_{p_{flow}}$, refers to the parameters of the flow—either local undisturbed flow at a location of the measurement, or a measured value, obtained by processing the three pressure readings on the probe surface when the probe is immersed into the flow.

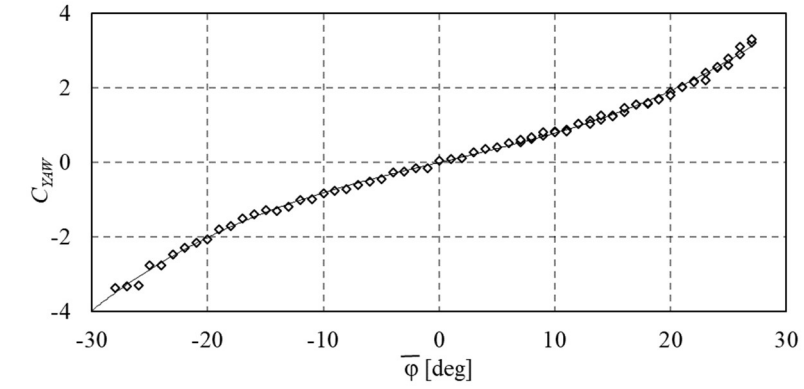

(a)

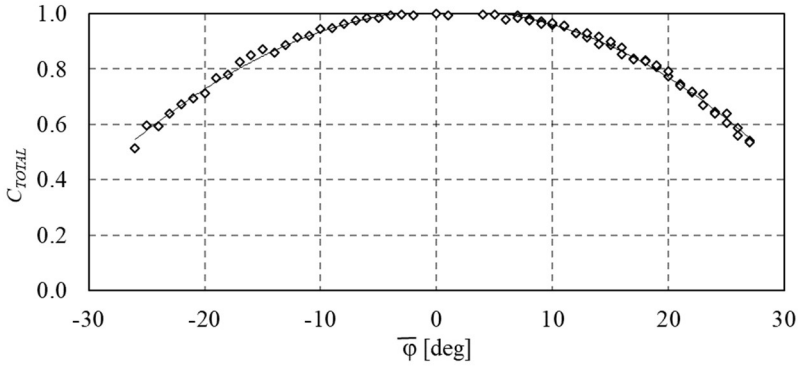

(b)

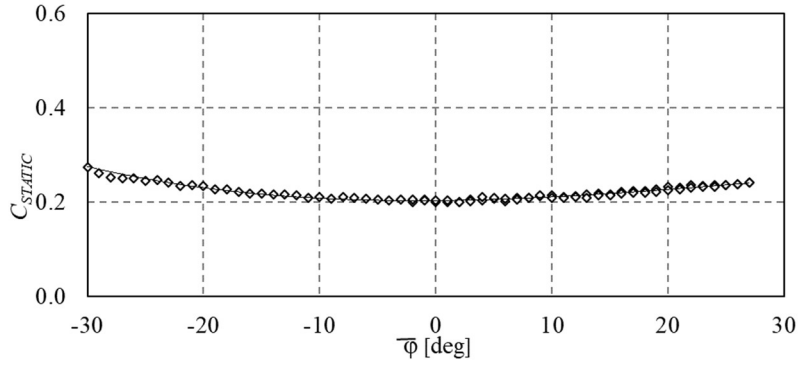

(c)

Figure 3.12 Calibration coefficients for one of the probes at Mach number 0.4

During probe vibration tests, the 5 mm stem was held in the fixture with a 6 mm diameter hole. This allowed the probe to oscillate by more than 3.5 mm (one probe diameter) forward and backward. Then the fixture had a 5.1 mm diameter and 10 mm depth, which significantly increased the rigidity of the structure, and the probe head vibrated within less than 0.2 mm (5% of probe diameter). The scale at the back in Figure 3.10 (b) was used for the postprocessing of

the probe position from the high-speed camera recordings. This data was used to calibrate the vibration measurements made by the built-in accelerometer.

In Figure 3.14 a comparison of pressure coefficient distributions is shown for a steady and then oscillating probe. Probe vibration mainly affects pressures at a 60° angular position and further downstream. This means that within ±20° of the probe incidence, its calibration coefficients can be used for the vibrating probe in a similar way as it can for the steady one.

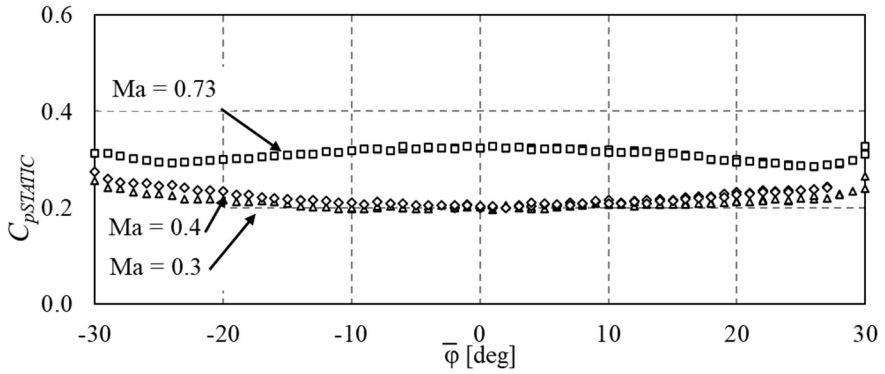

Figure 3.13 Calibration coefficient for static pressure at three flow Mach numbers

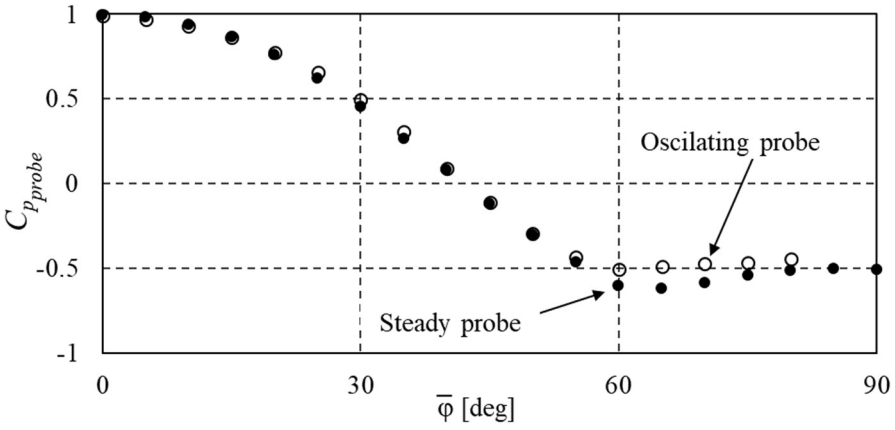

Figure 3.14 Calibration characteristics of the cylindrical probe: steady and oscillating

3.1.7 Measurement consistency

During the on-site testing, special attention was paid to the consistency and repeatability of the measurements. Figure 3.15 shows the total and static pressure measurements in one of the locations with two probes. The readings were processed with the freestream calibration

coefficients. The agreement between the two sets of data is within 2% of the dynamic head at the measured section.

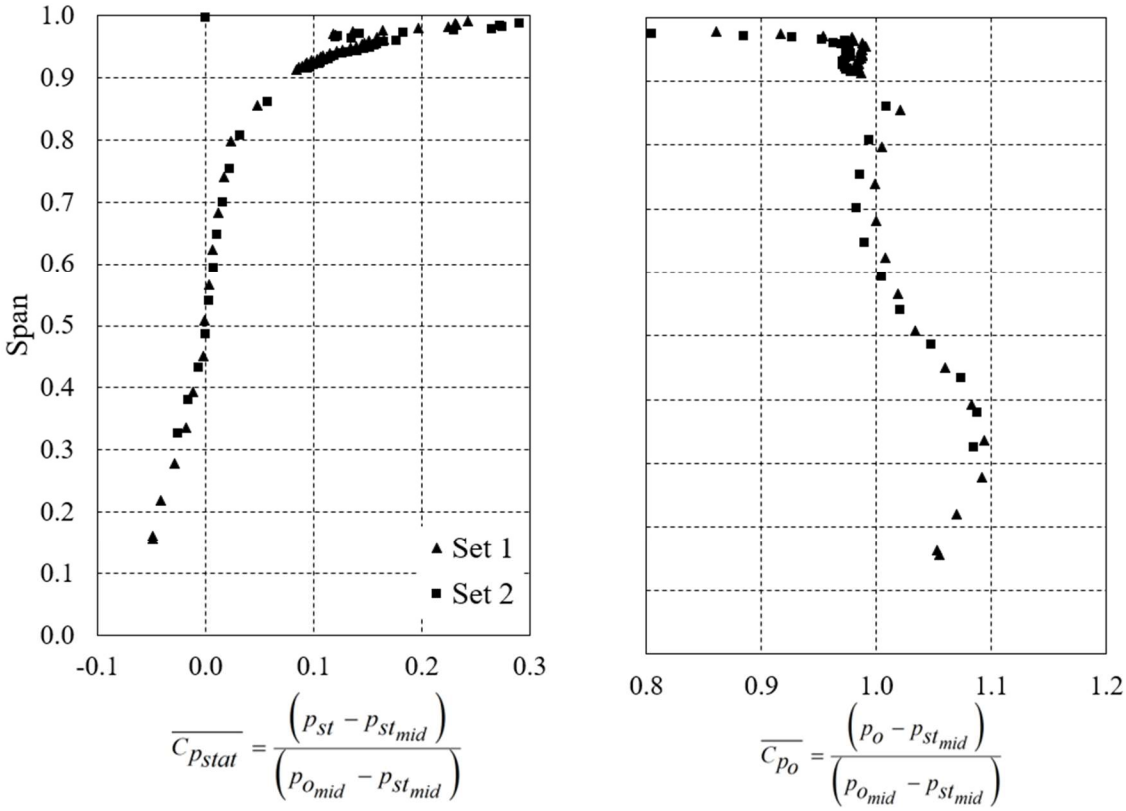

(a) (b)

Figure 3.15 Two sets of spanwise measurements of static (a) and total (b) pressures at the same traversing position with two different pneumatic probes

3.2 Computational modelling

ANSYS CFX was used as the main CFD package in the present research. This was to match the current design practice of the industrial partner. Originally, the modelling was carried out as a part of the compressor redesign process: the datum multistage compressor was simulated first to understand its performance. Then the multistage modelling results were used to apply the boundary conditions for the current study during the traversing gear development, and then for a better understanding of possible measurement uncertainties and deviations.

No attempts were made in this project regarding the improvement of the CFD performance in terms of better matching with experimental data or some reference cases. This work has been carried out during the collaboration with the industrial partner, and the outcomes of the validation procedure were found not to affect the basic findings of this thesis.

Neither the CFD nor experimental results are treated in this research as 'true values'. Instead, it is the use of the two methods to complement each other that can help the designer to capture the right physics of the flow and to see whether the experimental readings follow the consistency trends of the computational model, and, in turn, the model is correctly resolving the flow features such as the total pressure deficit near the end walls, which are more reliably captured by the measurements. In this section, CFD modelling parameters for each simulation are presented.

3.2.1 Modelling of the flow around the probe and the blades

Investigation of the flow field around the cylindrical probe in proximity to the stator blades is the main tool of the present research. It is known, that CFD methods can provide reliable calculations of potential flows, but if intensive vortical structures and flow separation zones are present, the CFD results should be treated with care (Denton 2010). Therefore, special attention has been paid to minimising the impact of CFD uncertainties in turbulence modelling on the outcomes of the work.

First, in most cases the probe was away from the blades and vortical structures, and their impact on the flow was only by the amount of blockage they caused. Therefore, the probe experiences the potential flow field effects caused by the blockage, and these effects are the main difference between the clean-flow laboratory calibration environment and the multistage axial compressor. When the blades or vortical structures were in proximity to the probe and could significantly change the flow field by affecting separations onset and local velocities, the results are used for qualitative purposes only.

Second, for the flow around cylindrical probe, the most uncertain region for orientation of the holes is near the separation point: ±90-110° of the probe circumference; this region is sensitive to the boundary layer modelling. However, later in the work it will be shown that the pressure field of the neighbouring blades and vortical structures has a significantly larger

impact on the probe's performance, and the limiting angle for the orientation of the holes will be below 80°.

For the same reason, modelling the probe downstream of stator blades is only possible when the blades are not stalled. In the absence of large separation zones, the CFD can adequately estimate the probe's blockage and flow redistribution both along the span—to the neighbouring passages and radially—under the probe.

A computational domain is shown in Figure 3.16, with five stationary blades taken from the real compressor geometry. Two cases were studied: the quasi-two-dimensional case and the full-span case. In the former, the blade span was twice the probe's height. This is to account for the conical transition part of the structure between the probe and the stem. At the same time, the probe tip was not included in the model to avoid uncertainties caused by the flow between the tip and the end wall. The end walls in this case were defined as free slip. Hub to tip ratio was kept above 0.95. The inlet conditions are uniform in both circumferential and spanwise directions. This relatively simple case was used to study a wide range of probe locations and flow conditions, which are presented in Chapters 5 and 6. Overall, more than 270 simulations were carried out with this setup.

The full-span case considered the full length of the blade including when applicable the radial gap between the stator and the hub. In this case, the complete realistic design of the probe and the stem was modelled with variable probe immersion. The end walls were defined according to the configuration of the real blade channel: a stationary no-slip casing wall and rotating or stationary (depending on the blade row) no-slip hub wall. For both cases steady simulations were performed.

The probe was immersed between blades 3 and 4, counting in the direction of rotation. At the inlet, the flow is circumferentially uniform, since downstream of the rotor the flow is naturally averaged out and the real probe is measuring the time-averaged signal. The unsteady effects were not considered in this research; all the simulations were performed in steady mode.

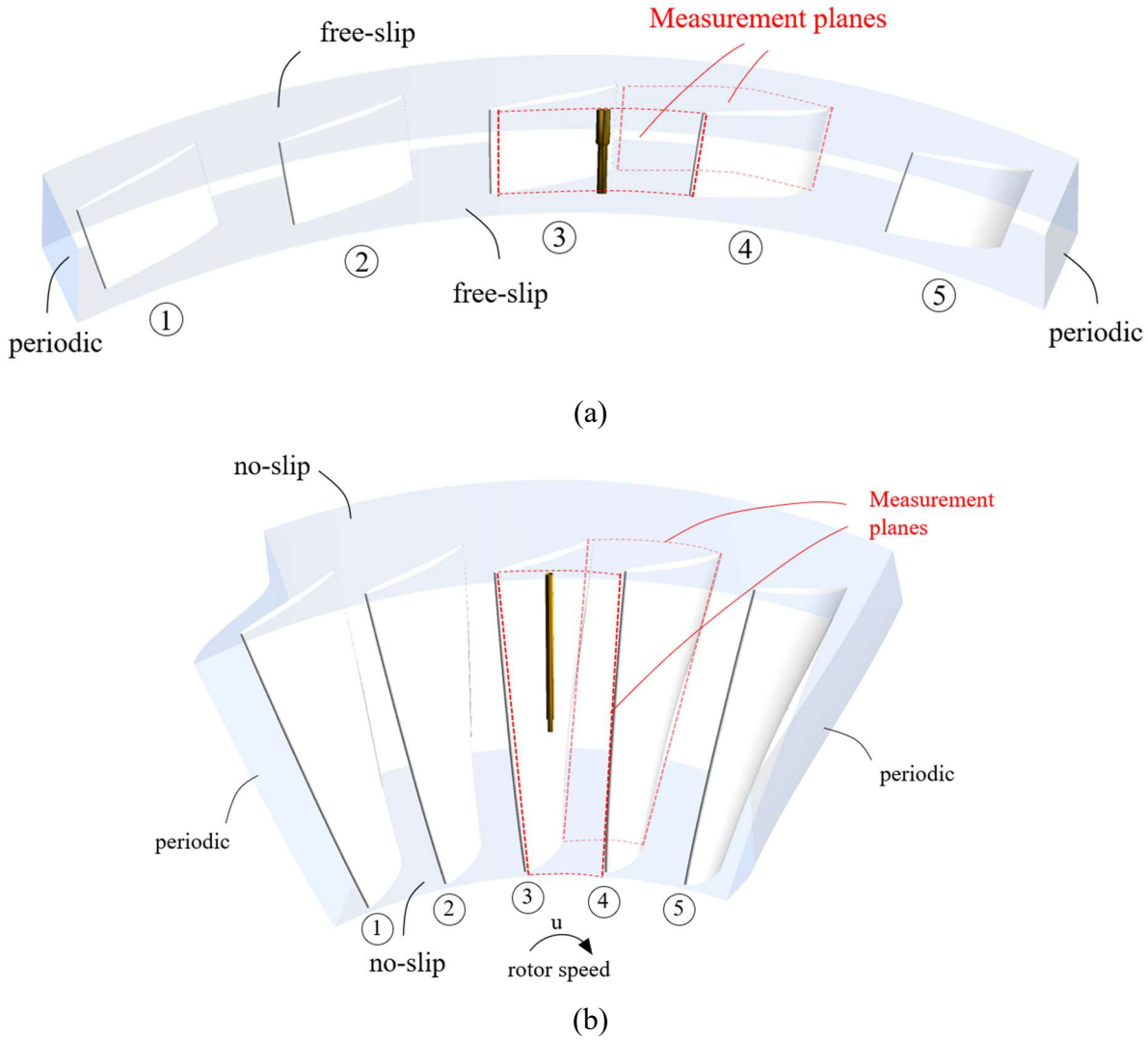

Figure 3.16 Computational model for the quasi-two-dimensional blade cascade (a) and the full-span case with the probe immersed upstream of the stator blades

At the outlet, for the two-dimensional case the static pressure was defined as uniform across the whole area; the pressures were chosen to reach the appropriate Mach number. For the full-span case, the pressure profile was taken from the multistage compressor simulation.

The domain has a rotational periodicity condition on the sides, which simplifies the setup, but limits estimations of the probe blockage effect on the full annulus losses and pressure rise.

For the two-dimensional setup, the boundary conditions at the inlet were taken from the multistage simulation results at the design point, and then they were varied for that setup with a range of speeds and incidences.

For the full-span setup, the conditions were taken from the multistage simulations at three operating points of the whole compressor. This is because the operating conditions do not change uniformly along the span, and manual varying of these conditions might not be physically correct. The boundary conditions also included flow temperature and turbulence intensity.

Meshing

The computational mesh was produced for the SST turbulence model requirements and normally had a parameter y^+ less than 1. For high-speed cases and multistage calculations this parameter did not exceed 10 on blade and probe surfaces.

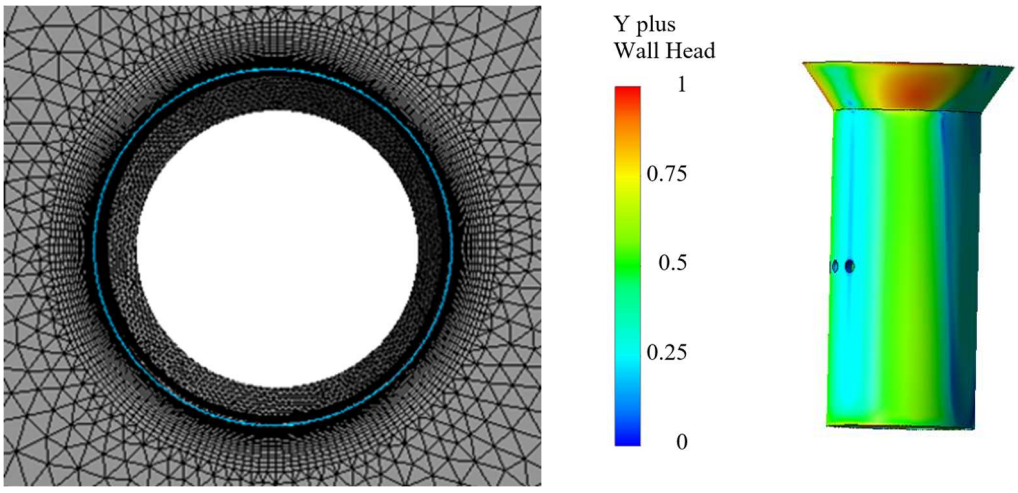

(a) (b)

Figure 3.17 Computational mesh around the stem and the probe (a) and y^+ distribution on the probe surface

The mesh around the cylindrical probe is shown in Figure 3.17 (a) and the y+ parameter on the probe surface is in Figure 3.17 (b). There were 30 prismatic layers on the probe surface with an expansion ratio of 1.1. The rest of the domain had a tetrahedral mesh. Inside the pressure holes were 10 layers of the O-grid mesh, however, as shown below, the pressure tappings were excluded from the consideration for the sake of simplicity, and the pressure distributions were calculated on a smooth surface of the probe.

The mesh around the blades was identical to the multistage compressor calculations. As a result, for a two-dimensional setup with the probe, the mesh size was over 3 million cells, for

a full-span case it was 10-12 million cells, and for the multistage simulation the overall number of cells was 68 million.

Turbulence model

The standard SST model was used for all simulations with a Gamma-Re-Theta transition model (Referred in ANSYS CFX manual as Gamma-Theta SST model, later in the text referred to as SST GTM) to account for laminar-turbulent transition in the boundary layer on the probe and blade surfaces. This was important since the Reynolds number based on the probe diameter was in the range of $2–6 \cdot 10^4$. In Figure 3.18 the two CFD-modelled distributions of probe pressure coefficient are compared with the measured values in the calibration tunnel. The effects of real geometry cause the experimental line to be higher than the two simulations; however, the onset of separation is in better agreement with the transitional model.

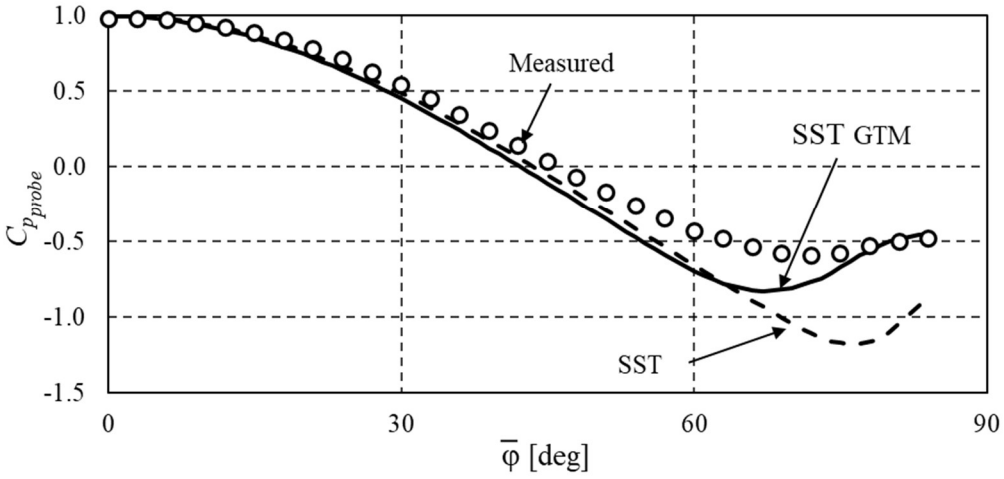

Figure 3.18 Effect of boundary layer modelling on the $C_{p_{probe}}$ distribution around the probe

Modelling of the pressure holes

Initially, the pressure holes were modelled as shown in Figure 3.17 (b), and the resulting channels were meshed more than two diameters deep into the probe. Then, for comparison, a smooth cylinder was simulated without the holes. The resultant $C_{p_{probe}}$ distributions around the cylinder are shown in Figure 3.19. The black line is a typical distribution over a smooth cylinder and the red dots show the $C_{p_{probe}}$ coefficient measured at the bottom of a properly meshed and modelled pressure hole. Along the descending part of the line, the coefficients agree within

0.5% of the dynamic head. Points further downstream of peak velocity were not used in the research.

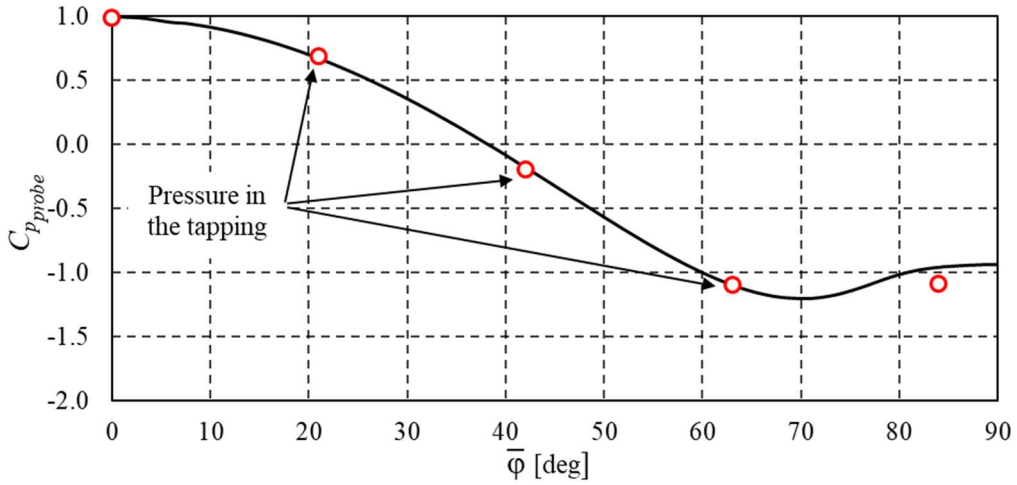

Figure 3.19 $C_{p_{probe}}$ distributions around the smooth cylinder, measured at the bottom of the pressure holes of the probe when modelled

3.2.2 Modelling of the multistage axial compressor

A full ten-stage simulation of the experimental compressor was performed to provide reference results for the experimental study. Despite possible uncertainties in computational modelling, especially when dealing with complex turbulent flows, CFD results can still be of great value for the experimental engineer, since one of the requirements for a CFD solver is to maintain the conservation laws within the whole computational model. Therefore, some of the simulated flow parameters can be used for comparison with the measured values:

- Mass flow. A combination of axial velocity and density integrated over a swept area (area of the channel, perpendicular to the axis of rotation) results in the mass flow value, which must be constant along the compressor. Therefore, the axial velocity distribution can be used as a reference for the measurement results.
- Energy conservation. The change in the circumferential component of the absolute velocity, ΔV_θ, is a measure of the work input into the system at a given rotating blade row. It can be seen as a change in the flow angle in the absolute direction on the

vector diagram. This work input results in the rise of the total pressure and the temperature of the flow. Therefore, a combination of measured total pressures and flow velocities in both CFD and the experiment can be cross-validated.

- Radial equilibrium. The pressure distribution along the span is mainly a potential flow field effect, caused by the flow swirl—the circumferential component of the velocity. It is also affected by the flow curvature in the meridional plane, for example, when the flow is deflected due to endwall blockage, and other parameters less significant for moderately loaded axial compressors.

The meshing parameters were as follows. The y^+ was maintained to be below 10. The total multistage setup has 68 million cells including the inlet and outlet domains. Along the operating line, the convergence of the multistage simulation was normally reached within 200–300 iterations depending on the initial state and flow regime, and the simulations carried on for 400–500 iterations.

In this work, no attempts have been made to fine-tune the CFD model of the multistage axial compressor to match it with the experimental results, nor there were attempts to blindly ‘adjust’ or ‘correct’ the experimental results towards the simulated ones. Instead, the physics-based corrections, developed during the simplified CFD simulations of the stator blade row with the immersed probe, are applied to the measurement results independently of the multistage CFD, and then the corrected values are compared against the simulations to see if basic physical principles are obeyed. In addition, the use of the basic settings of the commercially available software means more generalisable findings that can be verified by other researchers.

When the CFD-based corrections to the probe measurements are applied at given locations, the deviations between the two sets of values can be discussed in more detail, and only then can any attempts in model tuning be exercised.

Chapter 4 Influence of the channel walls on probe readings

A typical flow around the probe upstream of the stator blade row is shown in Figure 4.1 (a). The probe is measuring local flow angle, stagnation, and static pressures. However, when obtaining the measurements in a real multistage environment, two problems arise. The first is that the probe obstructs a significant part of the passage, causing the flow to accelerate around it and redistribute to the neighbouring passages, therefore the properties of this flow are no longer the same as without the probe. Second, the flow around the blade is fundamentally different from the undisturbed jet flow into a constant pressure plenum, at which the probe is calibrated in a laboratory environment, and when the freestream calibration coefficients are used, this can result in false measurements.

The idea of the probe blockage effect on the flow around the blade can be seen by comparing the flows at the suction sides of the left-hand side and the right-hand side blades in Figure 4.1. Although the flow around the suction side of the right blade is also affected by the probe immersion, the difference between the two flows can be seen.

Figure 4.1 (b) shows a simplified case, where the probe is placed in a rectangular channel of similar proportions to the real blade passage. The aim of this chapter is to study the probe measurements in this simplified channel so that the understanding can then be used for real blade environments.

First, to replicate the laboratory calibration process, the probe measurements will be taken within the side wall boundary conditions, allowing the flow to go in and out of the channel so that the probe blockage can be neglected. Next, the side walls will be modelled as solid inviscid walls to imitate the presence of the blades. An understanding of the probe measurements in this simple case will be used later in Chapters 5 and 6 for the probe locations upstream and downstream of the stator blades. Finally, as shown in Figure 4.1 (a) the probe is biased towards one side of the passage to represent one of the cases from the real engine as was explained in Chapter 3. Such proximity to the wall will be imitated in the final part of this chapter.

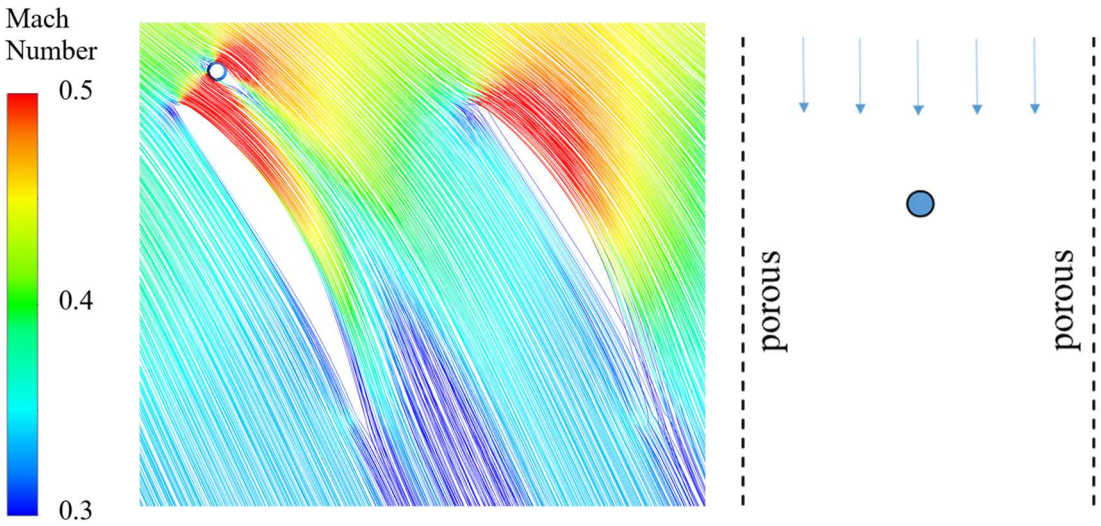

(a) (b)

Figure 4.1 Streamlines around the probe installed upstream of the stator blade row (a) and a simplified case of the flow calibration in a rectangular channel (b).

4.1 Probe calibration case

Figure 4.2 (a) shows a cross-section of the cylindrical three-hole probe, where each hole—P1, P2 and P3—is connected to an individual pressure transducer to measure the static pressure on a cylindrical surface. These three pressure readings are then processed to the flow parameters—flow angle, total and static pressures—based on the calibration coefficients described in Chapter 3. Figure 4.2 (b) shows the typical distribution of the pressure coefficient C_p around the circumference of the probe. The Cp values are calculated as follows:

$$C_{p_{probe}} = \frac{(p - \overline{p_{s,1}})}{(\overline{p_{0,1}} - \overline{p_{s,1}})} \tag{4.1}$$

Where $\overline{p_{o,1}}$ is a mass flow averaged total pressure and $\overline{p_{s,1}}$ is an area-averaged static pressure; both are at the domain's inlet, and p_s is a local static pressure at the probe's surface.

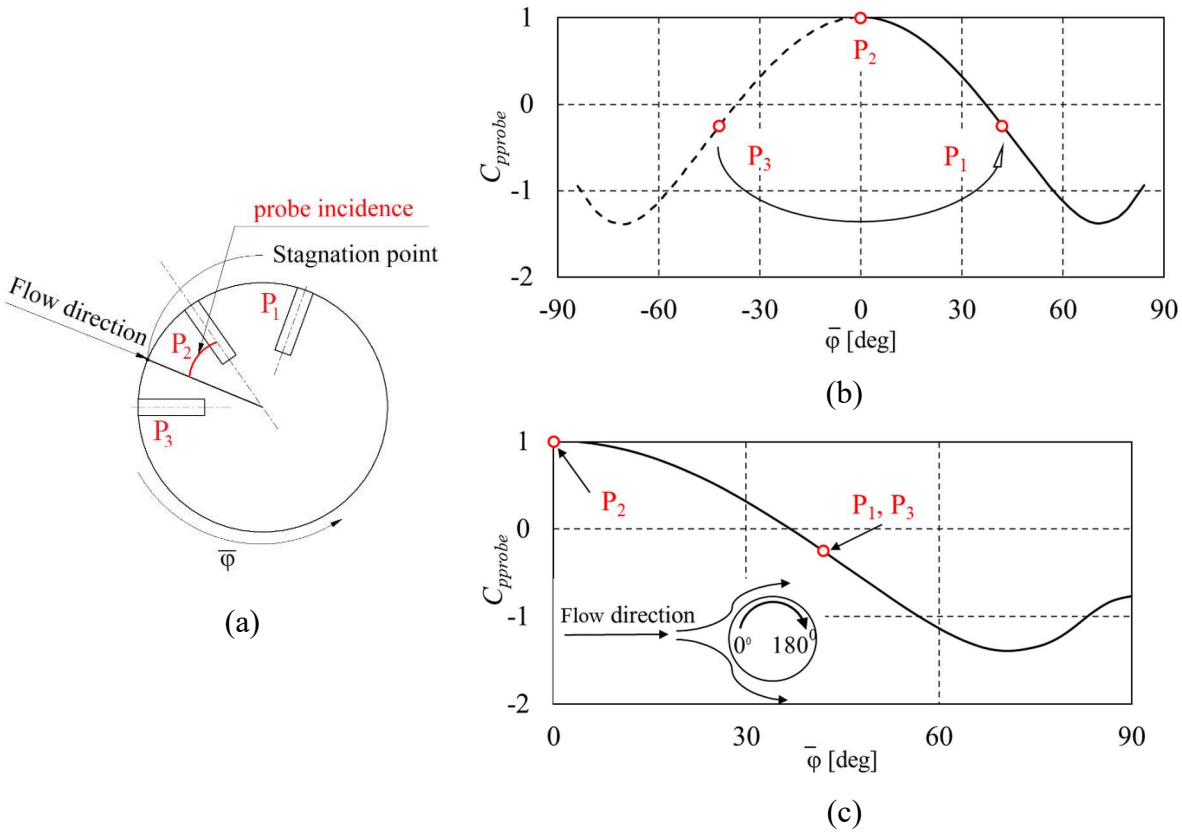

Figure 4.2 Cross-section of the probe (a), a typical C_p distribution around the cylindrical probe with the dots pointed at the angular position of the side holes (b) and the same distribution with the left-hand side of the curve flipped over zero point on the horizontal axis (c)

All the values of C_p in this chapter are non-dimensionalised by the averaged inlet flow conditions of the undisturbed flow. The pressure coefficient around the probe will be referred to as $C_{p_{probe}}$ and the pressure coefficient in the flow field will be referenced as $C_{p_{flow}}$.

In an idealised case, all three probe holes would have identical $C_{p_{probe}}$ distributions and the probe's incidence would have an offset, equal to the angle between the holes. The offset for the probe of interest is 42° between each other. At zero probe incidence, the middle hole is oriented along the flow direction and is measuring the total pressure, or C_p = 1.0, and the side holes read identical values at -42° and +42°, as shown in red dots in Figure 4.2 (b). Since the $C_{p_{probe}}$ characteristic is identical for all three holes, just one line can be drawn with three points

on it according to the angular offset between the points. In addition, for the sake of comparison, one can fold the line around the vertical axis, as shown in Figure 4.2 c). Now, if the flow around the probe is perfectly symmetrical, the two lines will overlap, and pressures P_1 and P_3 will be at the same place and have the same value. And when later the probe experiences the incidence and the asymmetry, the difference between the lines and the points will indicate this change in the flow.

Another important feature from Figure 4.2 is the location of the peak velocity, or minimum *Cp* value, which can be seen at around 70 °. In terms of measurements, it is important to have readings of P_1 and P_3 on the part of the $C_{p_{probe}}$ branches that have a negative slope, such as between 10 ° and 65 ° in Figure 4.2 c). Later in this chapter, it will be shown that due to the flow field interaction on the sides and downstream of the probe the peak velocity point and its location can be changed significantly.

4.2 Probe in a constrained environment

When the probe is immersed in the channel, the flow around it is affected by the type of wall boundaries and their proximity. This section aims to study how these affect the performance of the cylindrical probe immersed in the rectangular channel, first in the middle of it, and later near one side.

In this section, five cases are calculated to illustrate the probe measurements in this environment. A summary of the test cases is given in Table 4.1.

Table 4.1 List of test cases in Chapter 4.

Case #	Geometry	Locations	Boundary conditions
1	Straight channel	Centre	‘opening’ at the side walls
2	Straight channel	Centre	no-slip wall
3	Contracting	Centre	no-slip wall
4	Straight channel	$1D_{probe}$ from the wall	no-slip wall
5	Contracting	$1D_{probe}$ from the wall	no-slip wall

The first example is an unconstrained flow environment, typical of laboratory calibration. In Figure 4.3 (a) this is referred to as Case 1. Case 2 in the same figure has the same channel

geometry, but with solid walls on the sides, and Case 3 has solid walls with a flow contraction downstream of the probe. The contracting walls are inclined by 2.5° in order to account for the flow acceleration in the inlet part of the blade passage. The proportions of the channel are made to replicate a representative blade passage with the probe of interest; the ratio of the probe diameter to the channel width is 5%. In real operation, the values would be between 3 and 8%. For the sake of clarity, the size of the probe is exaggerated in the figure.

Figure 4.3 (b) shows the $C_{p_{probe}}$ distributions around the probe, where the black line is for Case 1, blue is for Case 2 and red is for Case 3. In this example, the probe is placed well within the channel, so that the walls are drawn both upstream and downstream of the probe.

When the flow around the probe has no limitations on the sides, it can freely go around it, so the probe blockage does not cause extra acceleration. This case was simulated with freestream boundary conditions at the sidewalls of the channel, which is referred to as ‘opening’ in ANSYS CFX. This type allows for the flow to enter and leave the domain on its sides depending on pressure distribution on the sides. This flow is similar to that of a free jet calibration tunnel, where the jet flows into a constant pressure plenum; the size of the probe is significantly smaller than the size of the jet, and its blockage is negligible. The black line in Figure 4.3 (b) represents such calibration conditions and is referred to later in the chapter as ‘CFD freestream calibration’. This line will also be used to obtain calibration characteristics of the probe for post-processing of the probe ‘readings’ in various conditions later in Chapters 5 and 6. The calibration was done for the whole range of inlet Mach numbers met in the compressor of interest.

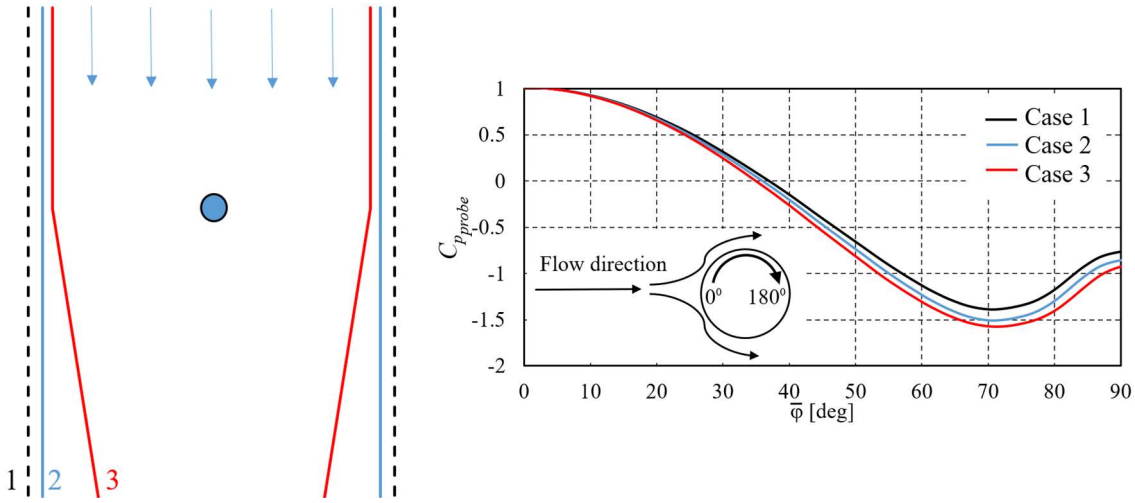

(a) (b)

Figure 4.3 A flow channel with a cylindrical probe in its centre, with varying boundary conditions on sidewalls (a) and $C_{p_{probe}}$ distributions around the cylinder at varying boundary conditions (b)

For Case 2, free-slip walls were introduced on the sides of the channel, as shown in solid blue lines in Figure 4.3 (a). The probe blockage has caused flow acceleration in the channel, and the $C_{p_{probe}}$ value at peak acceleration is 0.07 lower than that of the freestream jet. A different gradient in $C_{p_{probe}}$ distribution means that when probe hole readings are processed with the freestream calibration characteristics (Case 1), the results will show a 7% higher dynamic head. Case 3 introduces a contraction of the channel starting at the axial position of the probe's centre. This is to account for the flow contraction between the stator inlet plane and the throat of the blade channel: the flow is going around the stator leading edges and then towards the maximum thickness of the blades. In this case, the $C_{p_{probe}}$ value is lower by almost 10% than that of the freestream calibration at the position of the side holes, so when the freestream calibration characteristics are used to measure the flow, it will predict about a 10% larger dynamic head than it is in the undisturbed flow.

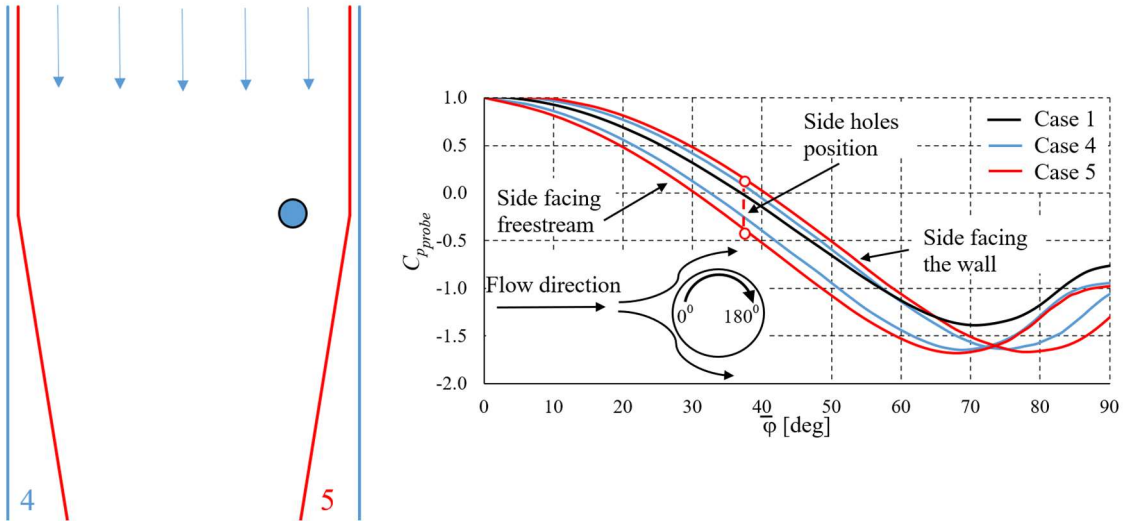

(a) (b)

Figure 4.4 Channel with the probe near the side wall (a) and $C_{p_{probe}}$ distributions around the cylinder at varying boundary conditions (b)

For cases 4 and 5, shown in Figure 4.4, the probe is placed at 7.5% of pitch aside from one of the walls, with Case 4 presenting the straight walls of the channel and Case 5 the contraction.

In Case 4 the probe is experiencing asymmetric pressure distribution on the sides, shown by the blue line. As a result, if the freestream calibration coefficients were used, the probe readings would result in a 7.2° flow incidence, despite the fact that the real undisturbed flow angle throughout the channel would be still zero, as the flow is strictly vertical. This illustrates how the probe readings could be affected by local flow asymmetry and flow redistribution, and how the probe could give false angular measurements.

It is important to notice here, that the local flow distortion causes a shift of the stagnation point on the cylinder surface aside from its strictly vertical location, which would be in the centre of the channel. In Case 4 the stagnation point has shifted by 2.7° away from vertical (Figure 4.5 (a). The remaining 4.5° in false angular readings is caused by the flow asymmetry around the probe due to the difference in the flow around the probe near the wall and on its other side. The dynamic head is 5% larger than that of the freestream.

Red lines in Figure 4.4 (b) show the $C_{p_{probe}}$ distribution for Case 5, in which the probe is near the wall with contraction. When measured with side holes at the same angular position, the dynamic head would be 10% larger than that of the freestream. The angle measurement error, in this case, would be more than 10°, and the stagnation point is shifted by 5.9° (Figure 4.5 (b).

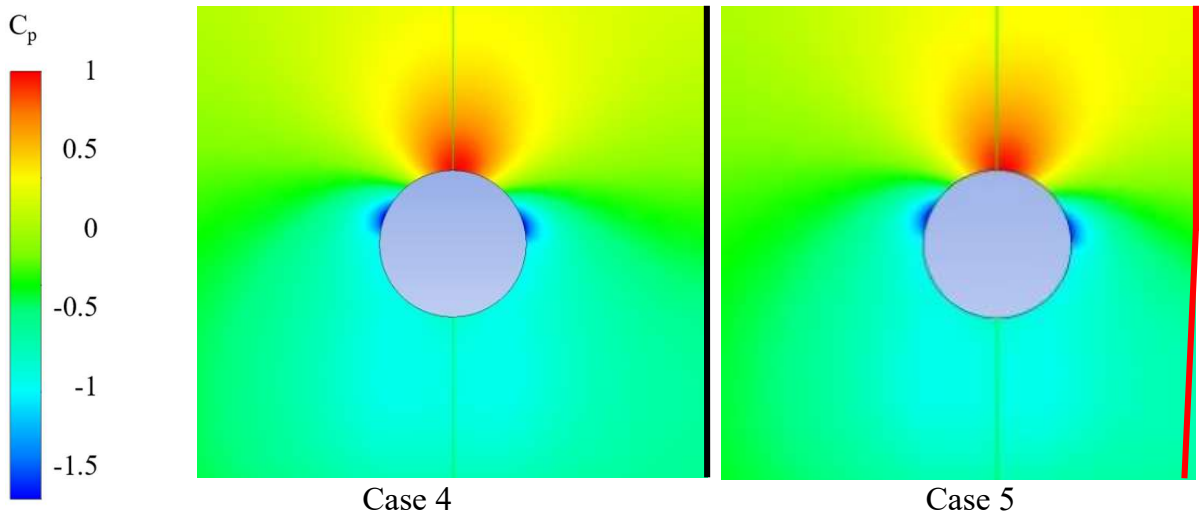

Figure 4.5 $C_{p_{flow}}$ flow field around the cylinder in proximity to the sidewall for a rectangular channel (a) and the one with the flow contraction downstream (b)

In Figure 4.5 the $C_{p_{flow}}$ distribution is shown around the probe placed near the wall. The stagnation point is shifted towards the wall. More details on such flows are given in Mutlu Sumer and Fredsoe (1999).

Figure 4.6 presents the same $C_{p_{probe}}$ distributions as in Figure 4.4, but now the lines are offset by the angular position of the stagnation point, which was shown to be non-zero for Cases 4 and 5. This is to separate the incidence onto the probe from the effect of flow asymmetry around the probe sides. Figure 4.6 (b) shows an expanded view of the $C_{p_{probe}}$ curves around 42°, where the side hole probes would be at zero probe incidence. The horizontal distance between the two blue lines is about 1.9°, which can be explained as a residual asymmetry. The shift in angular direction brings the lines towards each other, each of them by the value of stagnation point offset. For Case 4, the total asymmetry in Figure 4.4 is 7.2°; the stagnation point shift is 2.7°. This results in a remaining offset of 1.8°. Therefore, the flow asymmetry around the probe has a noticeable effect on the flow angle measurements.

The vertical offset between the two blue lines is 5%, and both lines are below the freestream distribution. This will cause the probe to measure a 10% lower average C_p value than it would in a freestream calibration. The same differences but on a larger scale can be seen in Case 5.

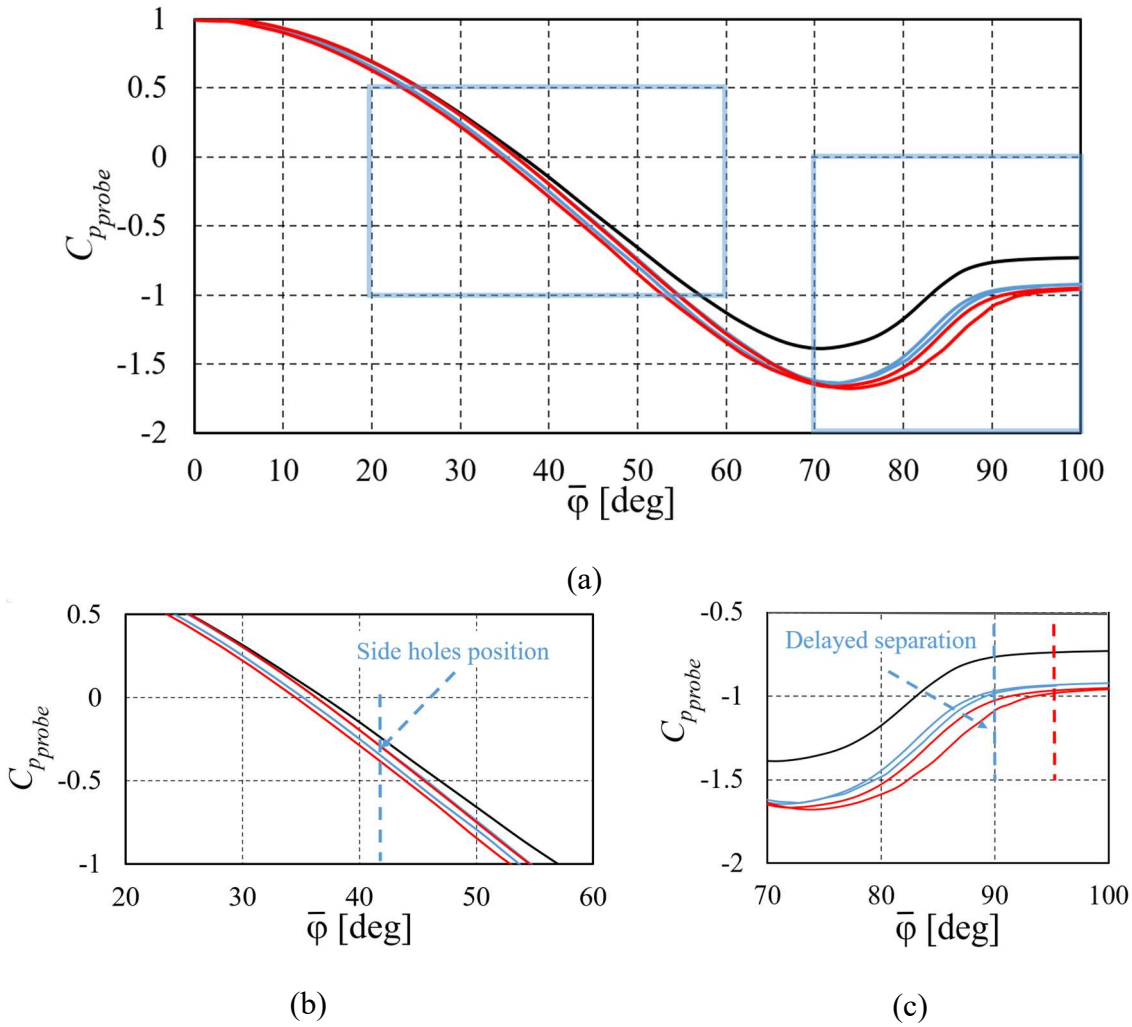

Figure 4.6 $C_{p_{probe}}$ distributions around the cylinder in proximity to the sidewall for Cases 1, 4, 5 (lines offset along the horizontal axis so the stagnation point is at zero) (a) with magnification near the side holes (b) and near the separation (c)

Figure 4.6 c) shows an expanded view of the $C_{p_{probe}}$ curves around 90°. The position of peak velocity (minimum $C_{p_{probe}}$ value) is shifted by around 5° for cases 4 and 5, and the gradients of the curves differ from those of Case 1. If one of the side holes is placed in this angular position, it will cause extra uncertainty to the probe readings. Therefore, it is important to keep track of the actual probe orientation during data processing and treat such measurement points where one of the probe holes is near the peak velocity with special care. Figure 4.6 (c) also shows a delay in separation position by 5°.

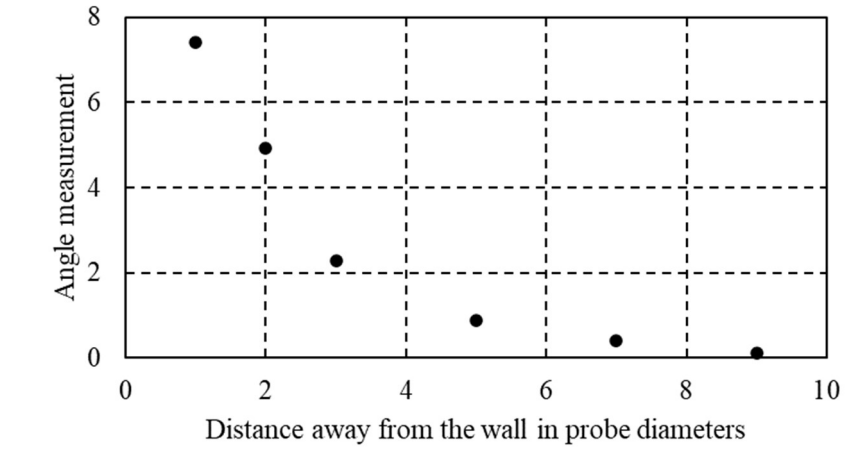

(a)

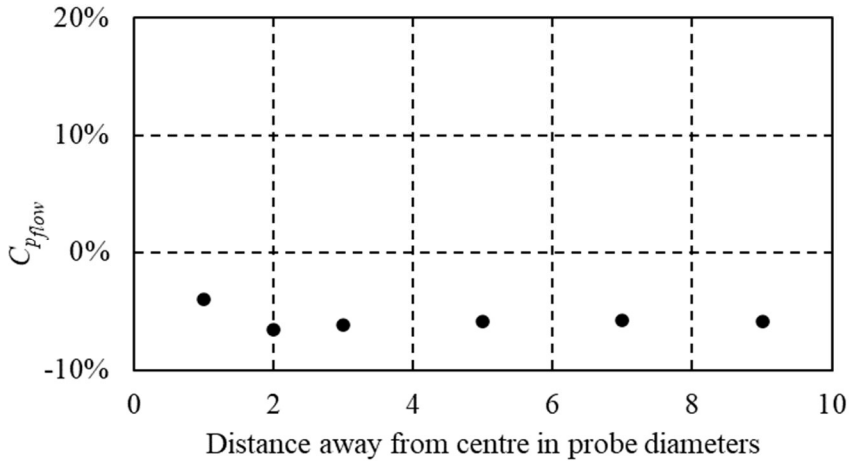

(b)

Figure 4.7 Deviation of angle (a) and flow pressure coefficient (b) measurements of the probe in a rectangular channel in proximity to the side wall (channel width is 20 x probe diameter)

In Figure 4.7 (a) the flow angular measurement error of the probe is shown as a function of distance away from the side wall for Case 4 and the error in measured pressure is shown in Figure 4.7 (b). The angle measurement deviation grows parabolically when approaching the wall; however, within six probe diameters away from the centre of the channel, this deviation is within 1°, and for on-site measurements it can be accepted.

Proximity to the channel wall mainly causes the angular offset between the $C_{p_{probe}}$ lines for probe sides, which mainly affects the flow angle measurements. The absolute values of $C_{p_{probe}}$

throughout the calculations used in Figure 4.7 (b) are more balanced for a slightly higher $C_{p_{probe}}$ value on the probe side near the channel wall; $C_{p_{probe}}$ on the opposite side was lower in the same manner shown in Figure 4.4 (b). As a result, for probe locations between the centre and 2 diameters away from the wall, the static pressure measurements varied within 2% of the dynamic head and are less than the undisturbed flow values by 5–7%.

For total pressure, the calibration map of the cylindrical probe is such that it is mostly the middle hole, which provides this measurement, especially when the probe is facing the flow. At the middle hole, there are no major loss sources or flow disturbances, unless the probe is measuring downstream of the stalled blade passage. Therefore, the probe measurements will normally provide the value of the total pressure within the measurement uncertainty.

The present example does not include the probe interaction with vortical flow disturbances such as blade wakes and separations from the suction side, nor does it include the opportunity for the flow to redistribute into the neighbouring blade passages. If the channel is one of many in the stator blade row, then increased resistance would cause flow redistribution to the neighbouring channels. To account for these effects and the real geometry of the blade passage, the next chapter presents a two-dimensional case of the cylindrical probe upstream and downstream of the stator blade row.

4.3 Concluding remarks

This chapter set up the framework for the research of the probe measurements when placed in a confined channel with a uniform or non-uniform flow field. The research addresses the impact of the complex flow environment on the probe measurements. Even though the probe immersion complicates the flow field further, it is the measurement uncertainty that has a practical interest during the experimental campaign.

With this, the flow mechanisms affecting the measurement uncertainties of the probe were illustrated. The probe's presence in the flow could affect the flow parameters, which are then measured by that probe. In addition, the flow field around it is no longer uniform as it would be in a calibration tunnel.

For an isolated channel, the probe's blockage would cause a higher flow velocity. In a given example, when the probe obstructs 5% of the channel and placed in the middle of the channel, it measures a 7% larger dynamic head. In the case with flow contraction downstream of the probe the measured dynamic head is larger by 10%.

Probe proximity to one of the side walls causes flow asymmetry around the probe, which can cause an error in flow angle measurement due to extra acceleration between the probe and the wall. The flow angle measurement error exceeds 7° for a considered passage. The deviation in angular measurements grows parabolically when the probe is moving away from the centre of the channel. The dynamic head is consistently higher by about 5–7% throughout the range of studied locations.

Separation onset on the cylindrical surface of the probe is affected by the wall proximity, therefore, at high probe incidence, when one of the measurement holes is placed near the separation region, the probe readings can be largely affected by the change in separation position. This becomes critical for non-nulling probes working in a wide range of incidences, and the calibration range of such a probe should be narrowed down.

Chapter 5 Probe placed upstream of stators

In this chapter, the probe is placed upstream of a row of stator blades as shown in Figure 4.1 (a), in several circumferential and axial locations. The aim of this chapter is to understand the key factors affecting the probe measurements in this environment and to discover whether and how these measurements can be corrected to obtain a representative value of the undisturbed flow.

First, a series of computational results will be presented at representative flow speeds and flow angles for a set of probe locations in a quasi-two-dimensional setup. The flow parameters such as flow angle and static pressures are compared with the local values of undisturbed flow and possible corrections are proposed. Then, test simulations are shown for the full-span setup, where the probe is immersed at different depths in a blade domain of a real compressor geometry. Finally, a possible strategy for measurement corrections of different the flow parameters metrics is discussed. A list of cases studied in this chapter is shown in Table 5.1.

Table 5.1 List of test cases in Chapter 5

Setup	Locations	Flow conditions
Quasi-2D	10 circumferential 2 axial planes	3 incidences 3 Mach numbers
Full-span	2 radial trajectories	Design point of the multistage compressor

5.1 A flow around the probe upstream of the stator blade row

This section provides the results of CFD simulations of the probe upstream of a stator blade row in quasi-two-dimensional setup. The end walls in this case were defined as free slip. Hub-to-tip ratio was kept above 0.95. Full details were described earlier in Section 3.2.1. The design inlet flow angle for this case is 45°. The raw measurements during the experiment are processed in the following order (see Munivenkatareddy (2016) for reference): first, the yaw angle is defined, and then the total pressure and the dynamic head which results in the static pressure. The pitchwise range of probe locations was chosen as 10–90% of the pitch, where 0% and 100% are axially upstream of the leading edges. This range is sufficient to capture the interaction of the probe with the surrounding blades.

The schematic of the probe head is shown in Figure 5.1 (a). The probe has three holes, and the angle between the upstream flow and the central hole axis is the probe's angle of attack. One side of the probe is facing the pressure side of the blade channel, and the other is the suction side. In this section the flow goes with design incidence for a given blade row, and the probe is aligned along the flow with its middle hole. Figure 5.1 (b) illustrates this, showing sample flow streamlines around the probe.

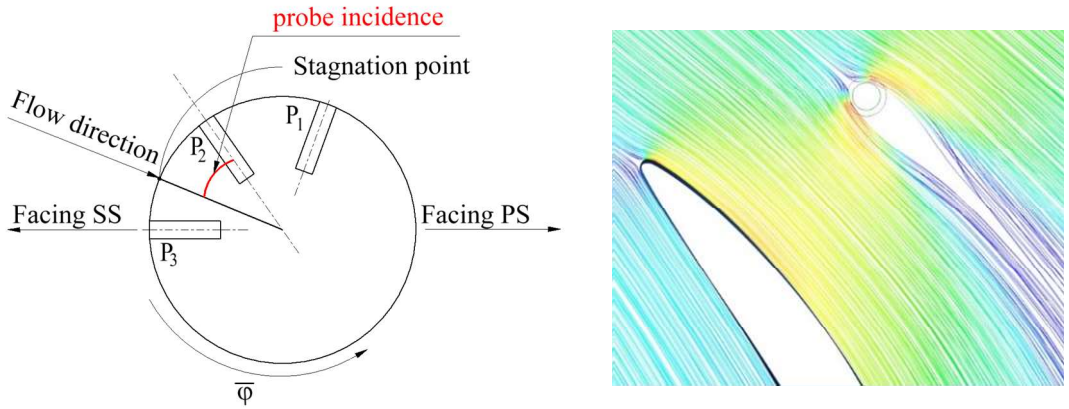

(a) (b)

Figure 5.1 Probe schematic (a) and streamlines around the probe upstream of the stator blade

In Figure 5.2 on the left-hand side, the Mach number contours around the probe at a range of pitchwise locations are presented. The $C_{p_{probe}}$ distributions around the probe are shown on the right-hand side. In this chapter, $C_{p_{probe}}$ is calculated with the local pressures of the undisturbed flow at the location of the probe in the denominator as shown in (5.1.

$$C_{p_{probe}} = \frac{(P - P_{s,local})}{(P_{0,local} - P_{s,local})} \tag{5.1}$$

Figure 5.2 shows the probe in three locations: near the suction side of the blade in Figure 5.2 (a), mid-pitch – (b) and near the pressure side – (c). On the right-hand side, the black lines show the $C_{p_{probe}}$ calibration curve for the freestream jet for comparison, and parameters of the jet are taken from the local parameters of the undisturbed flow at the location of the measurement. The broken blue line represents the C_p distribution for the side of the probe facing the suction side of the blade, and the solid blue line is for the one facing the pressure side of the neighbouring blade. The red dots show the readings of the three probe holes.

Here both blue lines are offset, moving the stagnation point to $\bar{\varphi} = 0$, as in Figure 4.6. The pressure coefficients go below the freestream calibration line in (a), which is explained by the faster local flow near the suction side as a result of a potential field distribution around the blade. When the pressures in the three holes are processed, the measured flow angle is 4.0° away from the pitchwise averaged angle of the undisturbed flow, showing more swirl in the circumferential direction. That means that for zero incidence of the bulk flow, the probe will be measuring almost 4° incidence. The undisturbed flow at the same location has a 3.8° incidence. The difference between the two is within the measurement uncertainty of real experimental work.

At the mid-pitch location in Figure 5.2 (b) the magnitude of the pressure coefficient is comparable to that of a calibration case. However, its gradient on the sides is slightly steeper, and when the readings of the three holes are processed, they result in 1.5% higher measured dynamic head, as is shown later in Figure 5.4. The lines on the probe sides go symmetrically around the stagnation point.

The same distributions are shown for the far-right location in Figure 5.2 (c) where the probe is approaching the pressure side of the stator blade. The probe's wake interacts with the leading edge of the blade, so there is a distinctive asymmetry on the sides. Because of this interaction the measured dynamic head is 24% lower than the average one at the inlet. The stagnation point in this case is shifted by 1.8°.

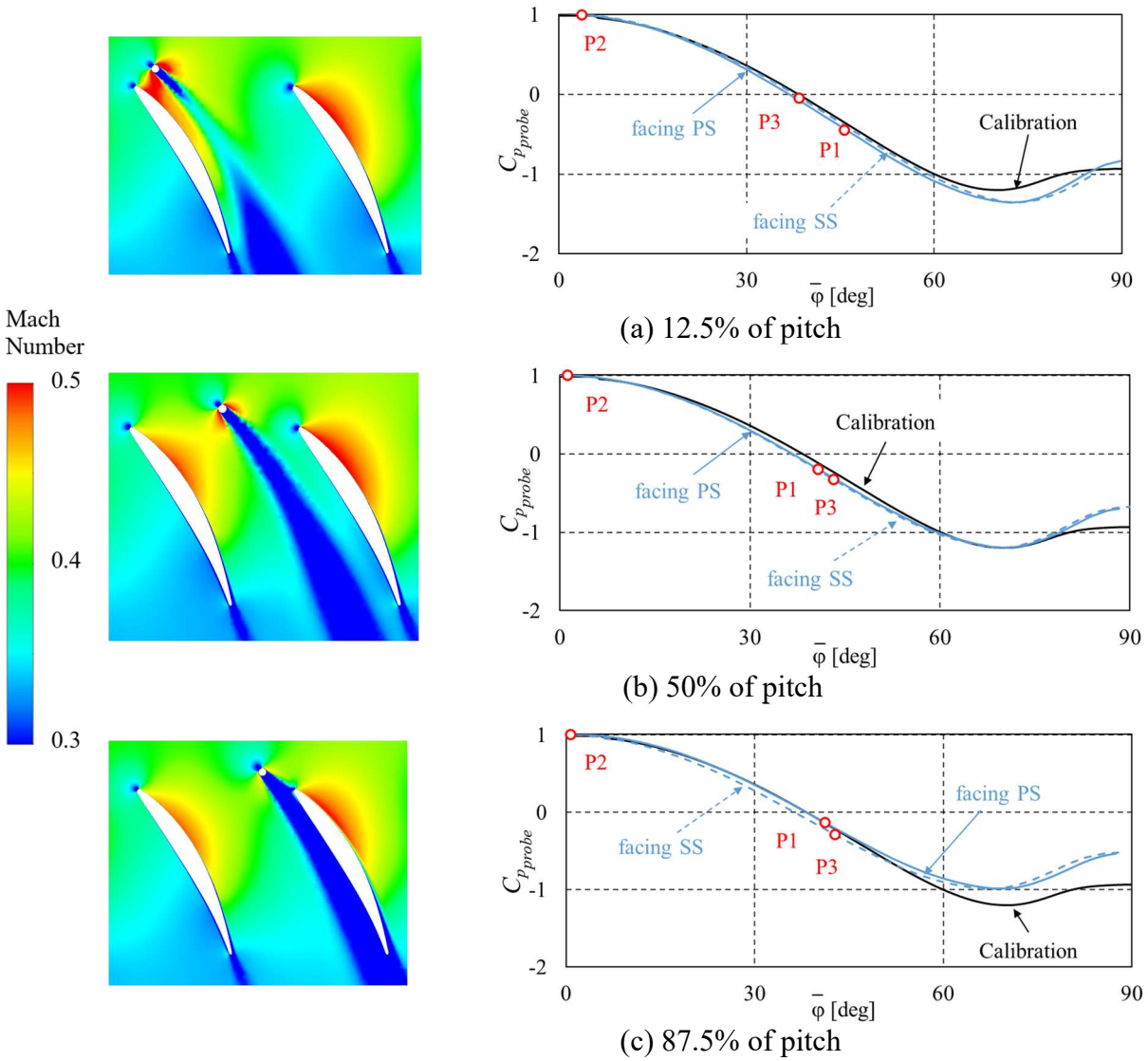

(a) 12.5% of pitch

(b) 50% of pitch

(c) 87.5% of pitch

Figure 5.2 Mach number contours around the probe in proximity to blade suction side (left) and distributions around the probe normalised by stagnation point (right) for the probe near the suction side (a), mid-pitch (b) and near the pressure side of the blade (c)

For the three sets of curves, the peak velocities on the probe sides are reached at separate angular positions, which can be seen by comparing Figure 5.2 (a) and (b) for example, where the minimum Cp values (or maximum velocity) are shown at the angular position of 75° and 70° respectively. This means that if one of the side holes is placed in this region due to high probe incidence in the real flow, the probe will measure false values of the flow angle and the dynamic head. Therefore, the probe orientation is crucial for low measurement uncertainties in such a complicated flow field, and at a probe incidence larger than 20° the measurements could no longer be reliably processed, even if the freestream calibration shows up to 25–30° incidence range for stable measurements.

Case (c) in Figure 5.2 agrees with the experience of Xiang et al. (2016), where the authors pointed out that the probe location near the pressure side causes the probe's wake to join the leading edge of a downstream blade, which is beneficial to overall losses associated with the probe immersion. However, it is unclear whether such a flow topology is beneficial to the measurement uncertainties.

5.2 Sensitivity analysis

When flow physics is presented, it is important to discuss the sensitivity of the probe readings to its location as well as the flow conditions. The range of these parameters is given in Table 5.2 together with some geometrical values, reproduced from Chapter 3.

Table 5.2 Flow conditions and geometrical parameters of the model

Parameter	Value	Unit
Pitchwise locations of the probe	10 – 90	[% of pitch]
Axial distance between the probe centre and the LE	1 and 2.5	[of d_{probe}]
Probe diameter to blade pitch	5	[%]
LE thickness to blade pitch	4	[%]
Incidence range	-5 – +5	[deg]
Inlet Mach number	0.4 – 0.8	-

5.2.1 Sensitivity to probe position

Circumferential location

Figure 5.3 shows a flow angle distribution along the circumference of the blade row for an undisturbed flow with Mach number of 0.4 and zero incidence to the blades. Locations upstream of the leading edges in the axial direction are at 0 and 1.0. The suction side of the blade is on the left and the pressure side is on the right. The horizontal axis presents a pitchwise direction. The schematic velocity diagrams are shown to define the meaning of positive and negative values on the vertical axis of the plot. On this graph, a zero value on the vertical axis is equal to the mass averaged flow angle at the inlet plane; the positive values mean that the flow is directed more towards the circumferential direction, in line with the turbomachinery theory, where the positive incidence means more increased flow turning in the blade passage. The negative values on the plot represent a more axial-directed flow. The formula for $\Delta\beta_I$ is as follows:

$$\Delta\beta_I = \beta_{Ilocal} - \beta_{IMFA} \tag{5.2}$$

Figure 5.3 (b) shows the solid line as Figure 5.3 (a) together with the probe measurements of the flow angle in solid circles. The empty circles are given for the angular position of the stagnation point on the probe's surface.

Measured values follow the general trend of the potential field. In proximity to the suction side at 5% of pitch the probe measures more negative incidence compared to the undisturbed local value. At 12% the values are within 0.5°. Between 10–80% of pitch the probe measures increased incidence compared to the undisturbed flow. The peak error in this region is 1.3°. When approaching the pressure side, the measurements have a notable shift in the trend compared to the undisturbed flow field: measured values show more negative incidence. This is due to probe wake interaction with the blade leading edge, as shown in Figure 5.2 c).

The angular position of the stagnation point presents the bulk flow direction around the probe. It can be seen that a significant portion of the potential flow field distribution is captured by the position of the stagnation point itself; however, the asymmetry on the probe's sides contributes up to a degree of difference. In addition, because of the flow asymmetry the offset between the probe measurements and the stagnation point's angular position is nonuniform along the pitch.

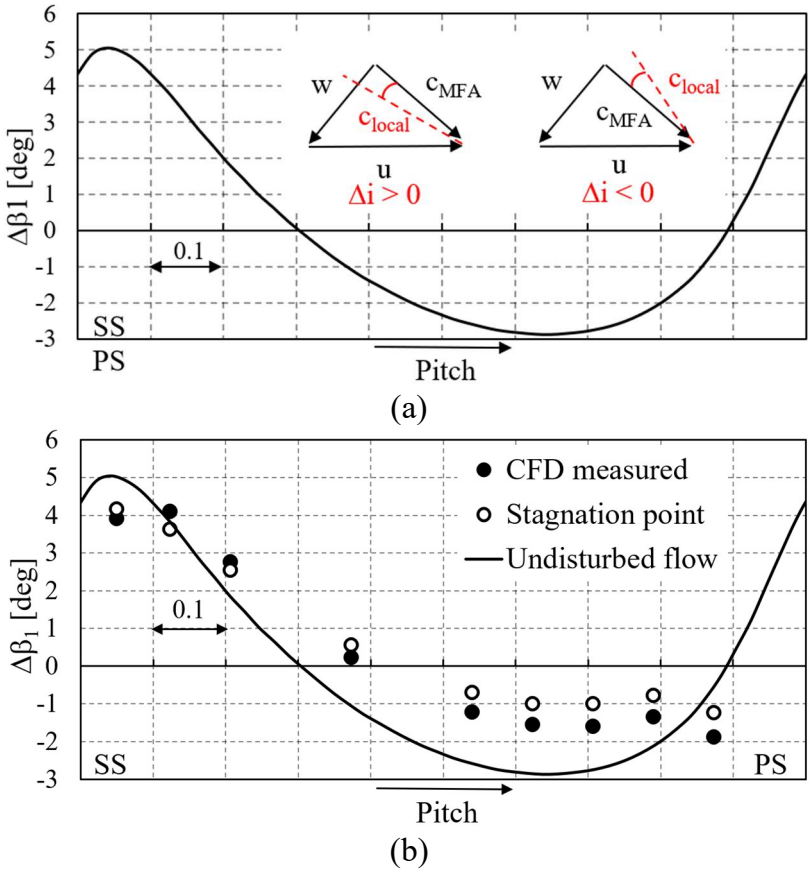

Figure 5.3 Flow angle distribution upstream of the stator at Mach 0.4 and zero blade incidence and the probe measurements at the same axial plane (a) and vector orientation schematic (b)

The difference in the angular position of the stagnation point and the measured angle shows that the false angular readings are caused not just by the change in the bulk flow, as was previously thought (see Coldrick et al., 2004a), but also by the flow asymmetry around the probe. In their paper Coldrick et al. placed the probe only in the middle of the passage and reported a similar difference of 0.8°; however, this difference is the result of two mechanisms combined.

Figure 5.4 shows $C_{p_{flow}}$ distribution along the pitch upstream of stators for undisturbed flow compared to probe measurements shown in circles.

$$C_{p_{flow}} = \frac{(P - P_{s,ave})}{(P_{0,ave} - P_{s,ave})} \tag{5.3}$$

Zero on the vertical axis means that the local pressure coefficient of the flow (C_{pflow}) equals to the mass flow averaged one. Values lower than zero mean that the dynamic head is larger. Intuitively, this chart has the same principle as C_p distributions around the probe, where the value of 1.0 means the total pressure of the flow and zero velocity, and the value of 0.0 is for the freestream flow static pressure. Similar to Figure 5.3, the general potential field pattern is captured well, with a 5% overestimation of the dynamic head at 12% of the pitch and a 5% underestimation at 78% of the pitch. At 55% of the pitch, the measurement agrees within 1% with the local flow value; however, both numbers give a 5% larger dynamic head than the average flow due to the potential flow field effect upstream of the stator.

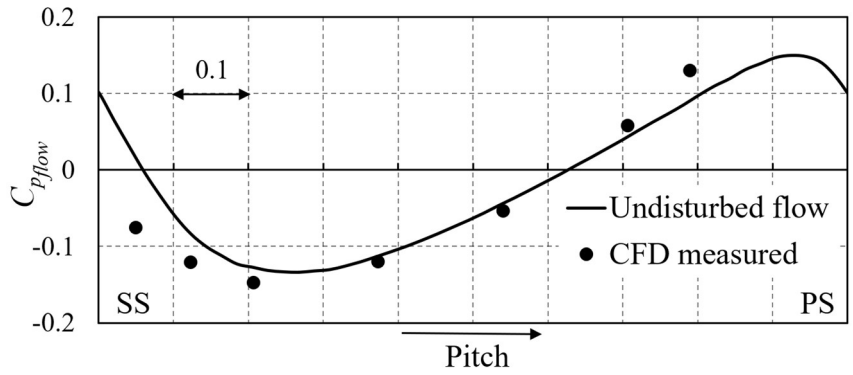

Figure 5.4 C_{pflow} distribution upstream of the stator and the probe measurements at the same axial plane

Axial location

Figure 5.5 (a) shows the two axial locations where the probe was placed during the study. Plane 1 is drawn at the probe axial location near the casing, which is at 13% of the stator chord away from the blade leading edge, which is about 2.5 times the probe diameter. Plane 2 is drawn to account for the bending of the holding stem under the aerodynamic force. This bending leads to an anticipated axial move of the probe by up to 1.5% of the probe's diameter so that Plane 2 is positioned further downstream, at 1 probe diameter upstream of the stator leading edges. Circumferential offset is applied to the readings in Plane 2 in a way that the probe is shifted along the vector of the inlet metal angle, as shown in Figure 5.5 (a).

The pitchwise distribution of the flow angle is shown in Figure 5.5 (b).

For these conditions, the flow angles vary between -5° and +12°, where '0' means the mass-flow averaged value at each axial location.

Parameters at Plane 2 in proximity to the blade's leading edges have steeper gradients, as shown in blue in Figure 5.5 (a). However, the probe 'measurements' do follow the trend in both cases with a comparable level of an offset in the mid-pitch, where the 'measured' values are higher by 2–4°. At Plane 2 the probe is immersed further downstream inside the channel, so the probe's wake interaction with stator leading edges is not seen at 10% and 90% of pitch, and all the measured flow angles are off to one side from the undisturbed flow.

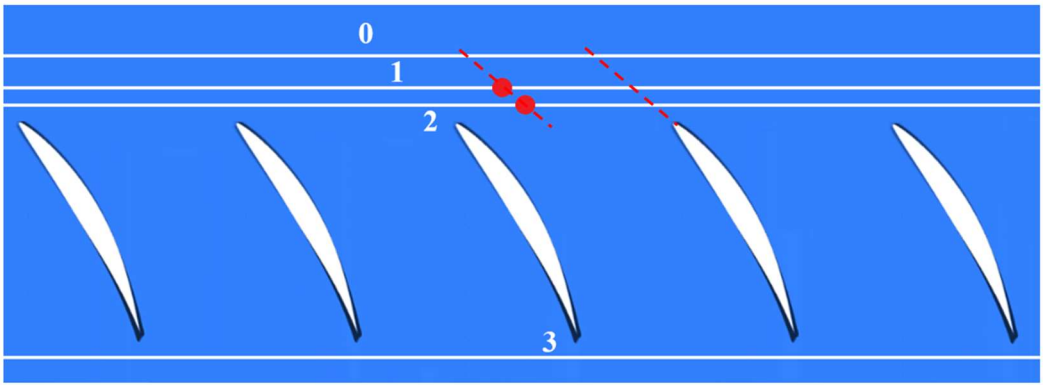

(a)

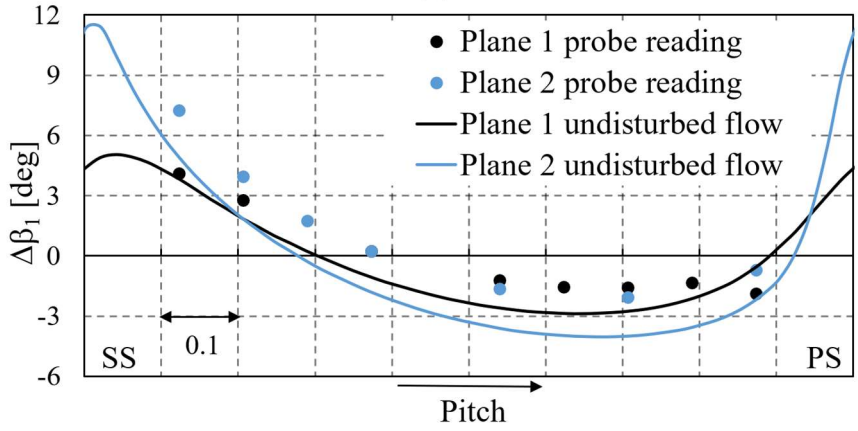

(b)

Figure 5.5 Schematic representation of the probe location (a) and pitchwise distribution of the flow angle upstream of the stator in undisturbed flow compared to probe readings (b)

One of the questions during data processing of real experimental results is whether these locally measured flow values should be compared/corrected to the local flow values, which can then be processed towards the mean value by the flow field calculation, or instead, whether

they can be corrected straight to the mean flow values following the shown trends. To answer this, the next section provides similar plots of the flow angles and the C_p coefficients for various flow conditions.

5.2.2 Sensitivity to flow conditions

5.2.2.1 Flow angle

A range of +/- 5° of the upstream flow incidence was taken to cover both unseparated and separated conditions in the blade channels. For the upstream measurements the downstream separations do not cause a significant change in measured values. However, with increasing incidence, the pressure gradient in the circumferential direction becomes steeper, and it is important to understand whether this can affect the probe readings and possible corrections. Figure 5.6 shows measured and undisturbed values of the flow angle and pressure coefficient at a range of blade incidences. Here, a zero incidence means the design flow angle for a particular blade row, and a positive incidence of '+5' means the positive incidence on the stator blades, causing higher flow turning in the blade channels.

In proximity to the suction side of the blade, the probe measures a similar or lower incidence compared to the undisturbed local value. In the case of a negative average flow incidence (-5°) the measured values are lower in the pitch range between 0 and 20% from suction side. This is because of the downstream effect of the flow around the blade suction side, as shown in Figure 5.7 (b).

For the positive incidence, the local flow angle varies between -5° and +7° compared to the averaged flow, and the difference with the measured values is the largest among the three lines. It is important to note that the interaction of the probe's wake and the leading edge starts further from the pressure side, so even when the probe is at 80% of the pitch, the flow angle measurements 'flip' across the line of the undisturbed flow and show more of an axial flow direction. This means that if a designer wants to have universal corrections insensitive to the blade incidence, pitchwise probe locations after 75% of pitch should be avoided. Figure 5.6 (b) shows the difference in pressure coefficient. In this case the trend is differs for according to the

incidence case: for +5° the dynamic head is underestimated by up to 8%, whereas for -5° it is overestimated by 2-7%.

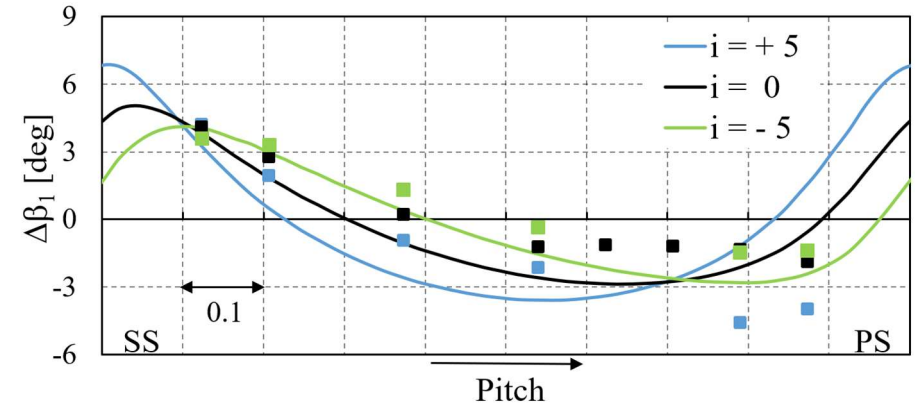

(a)

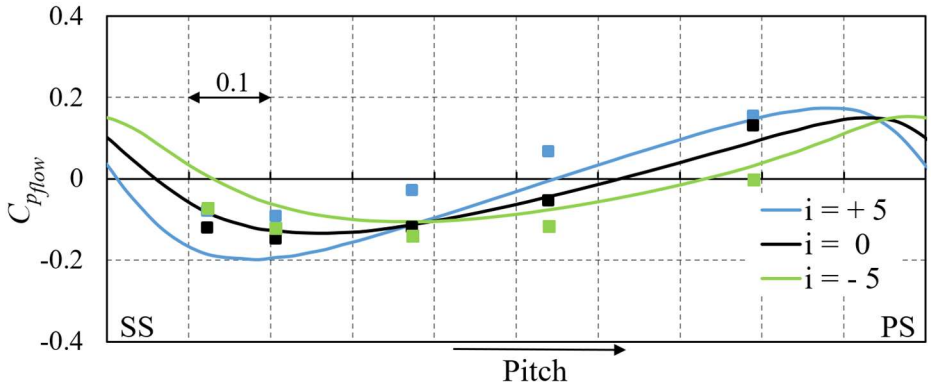

(b)

Figure 5.6 Pitchwise distribution of the flow angle upstream of the stator (a) and $C_{p_{flow}}$ coefficient (b) for selected flow incidences

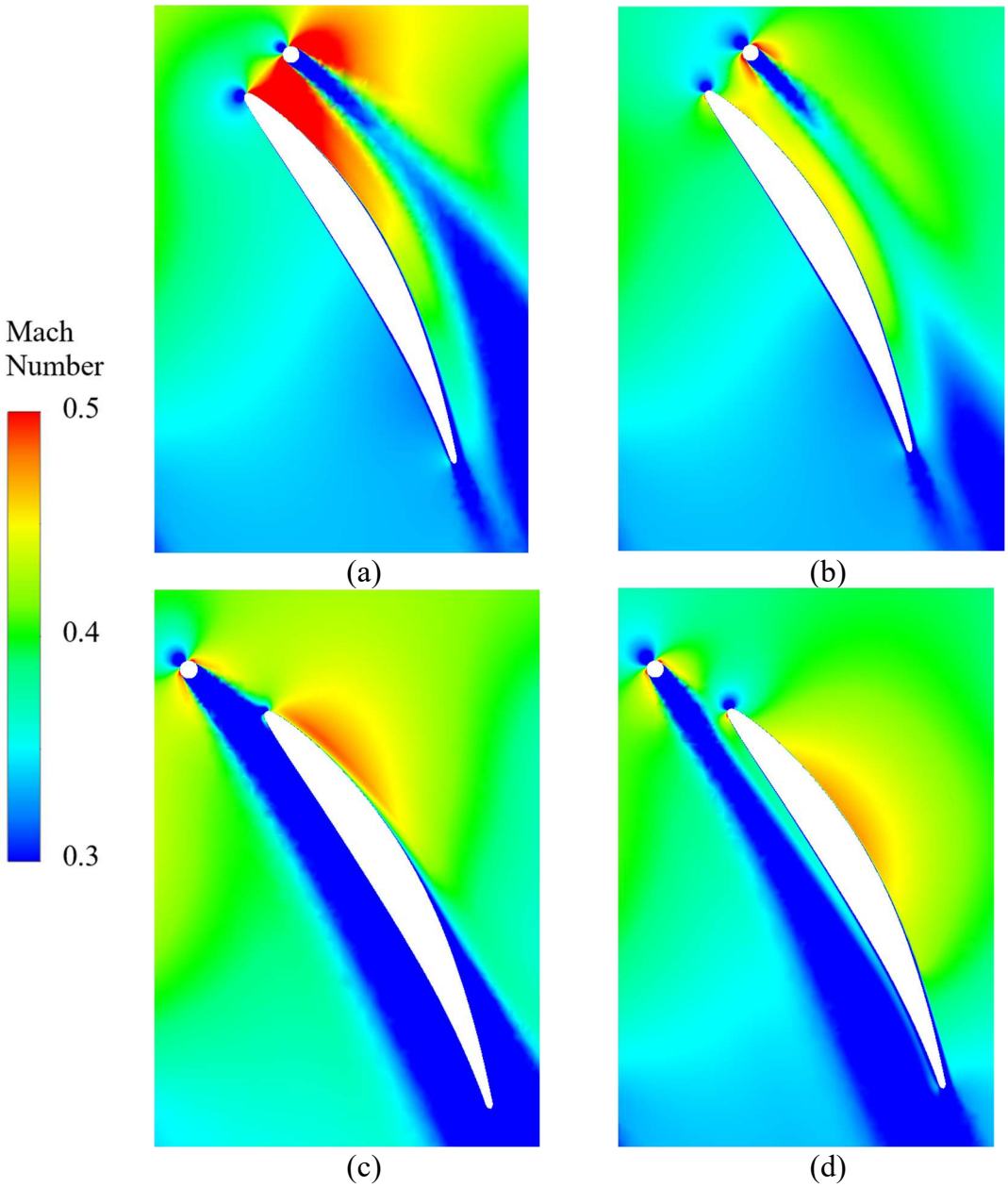

Figure 5.7 Mach number contours around the probe upstream of the stator blade row: (a) probe location at 10% of pitch and +5° flow incidence and (b) -5°; (c) probe location at 90% of the pitch for +5°, and (d) -5°

Flow Mach number contours are presented in Figure 5.7 for two probe locations and two incidences. The case of positive incidence with the probe near the suction side is shown in Figure 5.7 (a), whereas Figure 5.7 (b) is for the negative incidence; c) and d) are for two incidences when the probe is near the pressure side. In Figure 5.7 (a) the probe blockage in

combination with the flow direction causes additional acceleration between the probe and the suction side and also causes higher diffusion towards the trailing edge of the blade. At negative incidence a downstream part of the suction side acts as an asymmetrical contraction to the flow field around the probe, similar to the case presented in Chapter 4. This is why the green points go below the green line at 12% of the pitch in Figure 5.6 (a) and then at between 20 and 90% of pitch the points go above the line. For zero incidence, in the range of 12–85% the points are also above the line, and for the case of +5° the points are above the line between approximately 10 and 60% of the pitch.

Figure 5.7 (c) shows the flow around the probe in proximity to the blade leading edge and its pressure side at a positive bulk flow incidence of +5°. The probe wake in this case is significantly expanded and flows around the leading edge of the blade from both pressure and suction sides. For comparison, in case Figure 5.7 (d) with negative bulk flow incidence the wake is compressed and goes around the leading edge under the pressure side only. Probe wake interaction with the blade leading edge explains why in Figure 5.6 (a) the shift in trend between overpredicting and underpredicting the local flow incidence happens at varying pitches depending on the average flow direction: for positive incidence this effect starts at about 70% of the pitch, whereas for negative incidence the shift is not yet seen at 88%.

5.2.2.2 Flow Mach number

The flow field is further complicated when high-speed subsonic flows are presented in the field. Flow angles at various Mach numbers are shown in Figure 5.8 (a) and the *Cp* values are in Figure 5.8 (b). The undisturbed local pressure values are shown by lines, and probe readings by symbols. For all the flow conditions of interest, the measured flow angles are consistent with the undisturbed flow within 2°, and the shape of the trends is similar for all the lines. In fact, the three series of measured values are closer to each other than the three lines of the undisturbed flow. In addition, the magnitudes of flow angle variations are similar: within ±5° from the averaged angle. The main difference is at the ends of the lines, near the blade walls: the points cross the lines at multiple pitch positions as a result of changing potential field, so that for a Mach number of 0.8 the measured values are just slightly above the undisturbed flow

with no effect on the readings from the pressure side of the blade (within the studied range of locations).

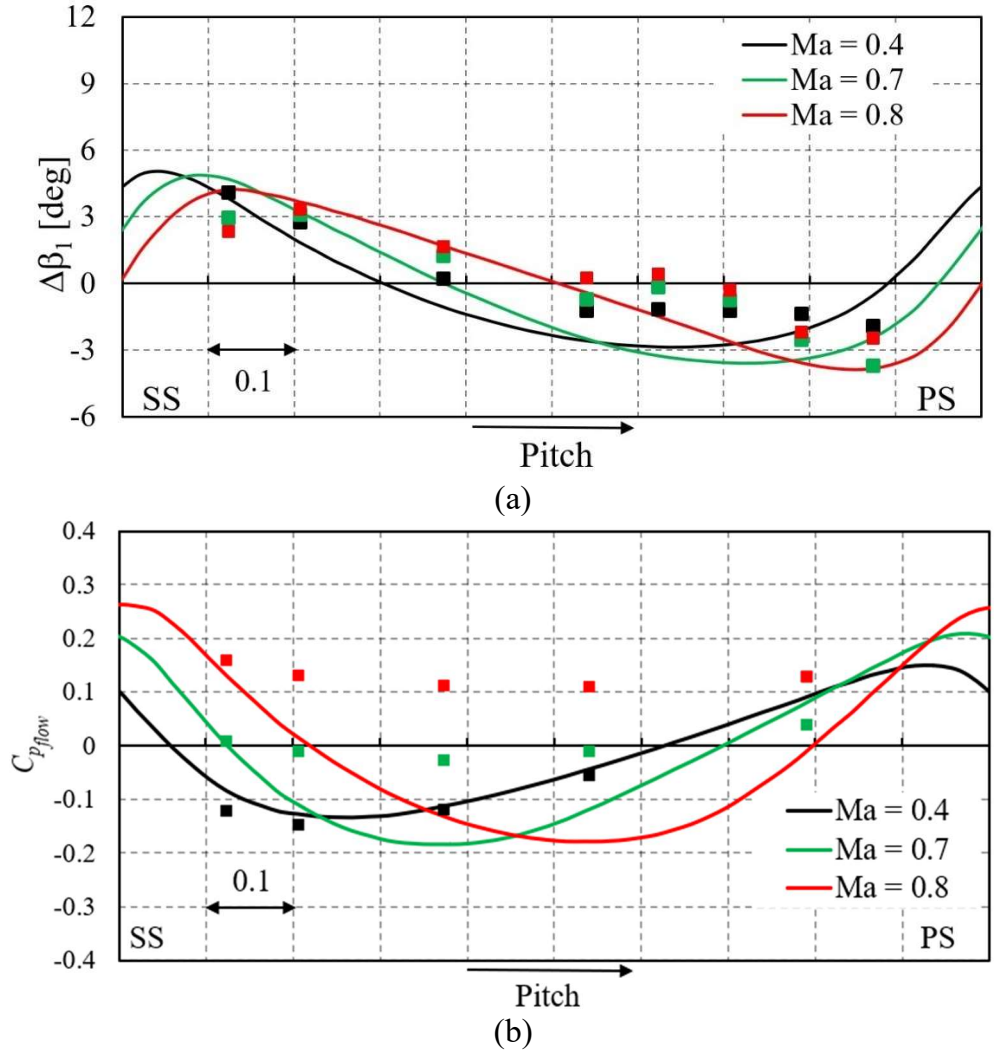

Figure 5.8 Pitchwise distribution of the flow angle (a) and $C_{p_{flow}}$ (b) upstream of the stator for a range of flow Mach numbers

It can be seen that for all operating conditions the difference between the measured flow angle and that of the undisturbed flow at the point of measurement follows the same trend of overestimating values in the middle of the passage. This can be used to develop a correction procedure for measured values which will be independent of the inlet flow conditions. Then the local values can be transferred to the representative pitchwise averaged value with the use

of CFD, and since the flow distribution upstream of stators is mainly a potential effect, the CFD gives reliable distribution.

Measured values of the C_p shown in Figure 5.8 (b) rise in line with the Mach number as it increases, which means that the measured flow speed will be lower than that in the undisturbed flow. The values also become more uniform along the pitch, which does not follow the undisturbed flow field pattern. The changes in *Cp* distribution are the result of reaching critical flow conditions around the cylinder (Zdravkovich 1997): it is known that when the freestream Mach number upstream of the cylinder approaches the value of 0.7, the peak velocity on its surface reaches the speed of sound and the probe blockage grows nonlinearly. Upstream of the blade passage, these transonic flow regions significantly increase the blockage effect from the probe, and the flow is close to the choked conditions. This also causes more significant flow redistribution to the neighbouring channels.

Figure 5.9 illustrates the difference in blockage between subcritical (Mach 0.4) and critical (Mach 0.7) cases. In this figure, red means that in that location the undisturbed flow is faster than the one with the immersed probe, and the difference exceeds 30% of the freestream inlet Mach number. The coarseness of the plots is caused by interpolation between two meshes. From the CFD post-processing, in the second case the probe wake is 15% wider and the Mach number is more than 30% lower than in the undisturbed case compared to 10–15% for the low-speed case. Similar differences can be seen near the suction side of the blade at the location of peak flow velocity.

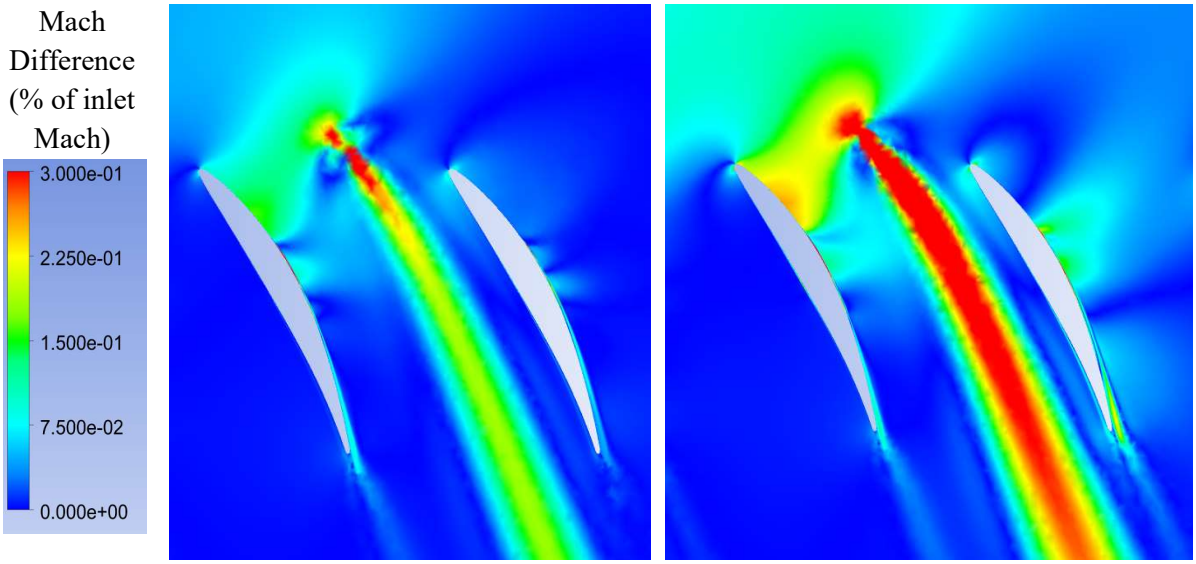

(a) (b)

Figure 5.9 Mach number differences between cases with and without the probe at Mach 0.4 (a) and Mach 0.7 (b)

In Figure 5.10 the $C_{p_{probe}}$ distributions are shown for the subcritical (blue line) and critical (red line) upstream flow conditions: Mach 0.4 and 0.7 respectively. The two black lines are shown as a freestream calibration references at local undisturbed values of the Mach number at the location of the measurement. Figure 5.10 (a) is for the probe near the suction side of the blade and Figure 5.10 (b) is for the central position. The $C_{p_{probe}}$ values are also calculated for the local parameters of the flow.

When approaching a critical Mach number, the C_p distribution line goes above the one for subcritical conditions. However, this effect is accounted for during calibration, and the two black lines are shown to prove that. What is not captured during calibration is the increasing probe blockage effect, especially at the centre of the passage. The three pressure readings will result in the measured dynamic head being 10–20% lower than to the undisturbed local value (see Figure 5.8 (b)). A series of calculations near the critical Mach number have shown that the deviation of the measured values from the undisturbed ones grows parabolically after Mach 0.6.

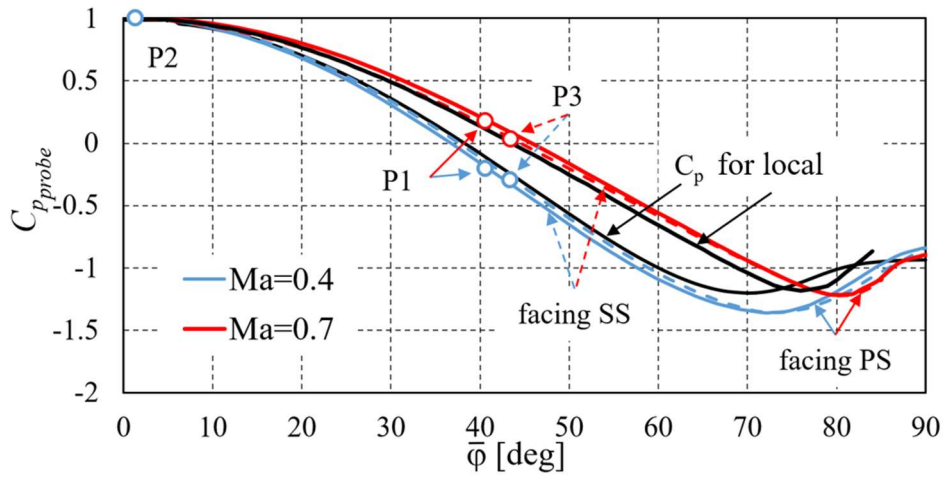

(a)

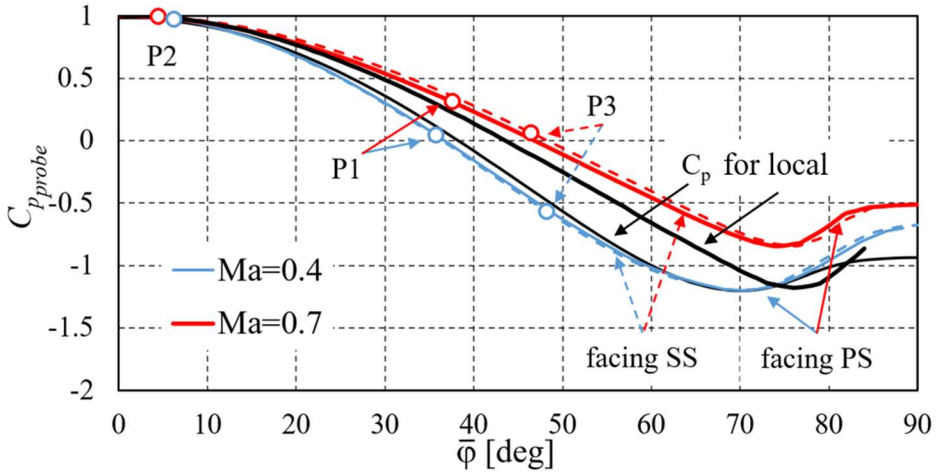

(b)

Figure 5.10 Cp distribution around the probe at selected Mach numbers for the probe at 12 % (a) and 54% (b) of the pitch

5.3 Correction for the presence of the probe

In the previous section, CFD-measured values, as well as the distributions of the undisturbed flow were compared against the pitchwise averaged flow parameters (zero on the vertical axis of the figures). For the locations near the middle of the passage, it was shown that most of the difference in the averaged flow is caused by the flow field distribution around the blades. The

aim of this section is to account for the presence of the probe in the flow field when measuring local flow parameter as it would be in the undisturbed flow.

As a result of the whole set of simulations, Figure 5.11 shows the differences between the probe measurements, simulated in CFD, and the local values of the flow for the range of operating conditions from Table 5.2. In Figure 5.11 the vertical axis shows the difference between the local undisturbed flow and the CFD-measured one, so zero on the vertical axis means an undisturbed flow value. The colour and symbol scheme on the figure covers nine operating conditions: three incidence angles at three Mach numbers each.

Between 0.2 and 0.7, the differences between the measured and local flow angles fall within a 2° range. Therefore, within this region of locations, the corrections for the flow angle measurements can be applied independently from the flow conditions. Away from this region, the probe interaction with the walls becomes significant and the readings become sensitive to the upstream flow conditions, so the corrections can no longer be independent from operating conditions.

The correction of the probe readings to the local flow values can be less sensitive to the flow conditions when the probe is near the centre of the passage, and a simple parabolic correction curve can reduce the probe reading uncertainties to within a ± 1° range. The approximate correction function for a given set of conditions and geometry could be written as follows:

$$\Delta\beta_{1corr} = \theta^2 C_2 + \theta C_1 + C_0 \qquad \theta \in (0.2; 0.7) \tag{5.4}$$

Where $\Delta\beta_{1corr}$ is a correction value to be subtracted the measurement to obtain a local value of the undisturbed flow; θ is a relative circumferential position of the probe from 0 to 1. C_2, C_1 and C_0 are the correction line coefficients. For the line shown in Figure 5.11 the coefficients are -7.1, 7.3 and -0.1 respectively.

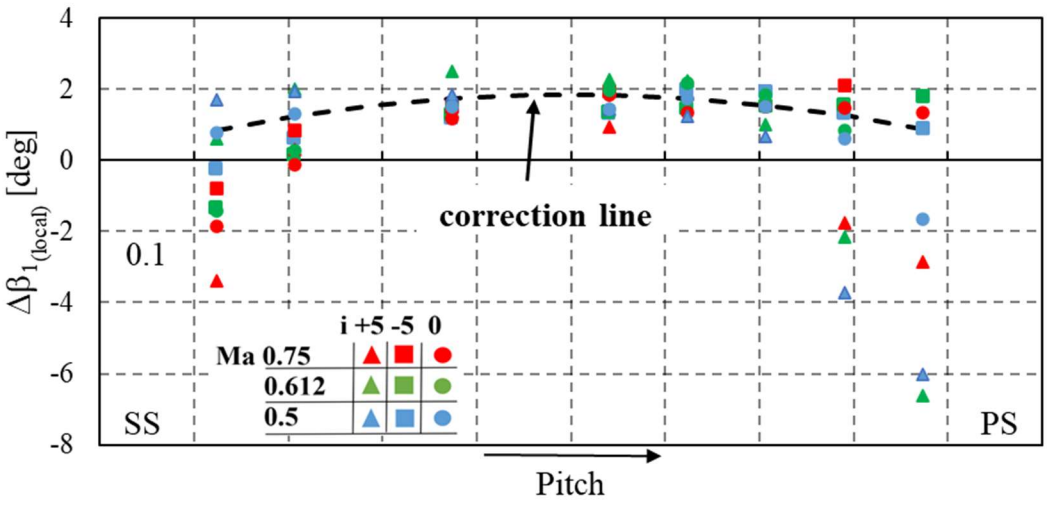

Figure 5.11 Flow angle differences between local values of the undisturbed flow and the probe readings at the same locations (zero on the vertical axis means the measured value equals the undisturbed one)

The range of 20–70% of pitch is equivalent to a distance from the blade wall of four probe diameters from the suction side, and six from the pressure side, which is two-to-three times bigger than the sensitivity range reported by Lee and Yoon (1999). The main reason is in the interaction of the vortical structure—in this case the probe wake—with the curvilinear surfaces of the downstream blade, which was not considered by Lee and Yoon in their setup.

The difference between the measured and local values of $C_{p_{flow}}$ is more case-dependent. Figure 5.12 (a) is a result of processing Figure 5.6 (b), and Figure 5.12 (b) is a result of processing Figure 5.8 (b). The graph shows the difference between the measured value of the $C_{p_{flow}}$ and the undisturbed flow. The differences are shown for a pitchwise location of 0.375 as an example. In Figure 5.12 (a) the differences are shown as a function of bulk flow incidence upstream of the stator blades and in Figure 5.12 (b) these differences are shown for varying upstream flow Mach number. Equation 5.3 defines the difference between measured and local $C_{p_{probe}}$. Equations 5.4 and 5.5 represent examples of the correction curves for a particular circumferential location used during this work. During experimental data processing, the

coefficients for Equations (5.5(5.8 were stored in the three-dimensional matrix for the circumferential locations of the probe, flow incidence, and upstream Mach number. When the corrections are calculated, the resultant local value of the flow can be obtained according to Equation 5.6.

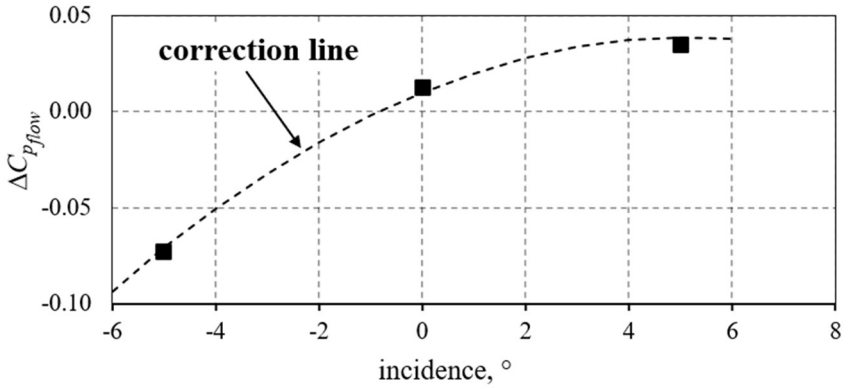

(a)

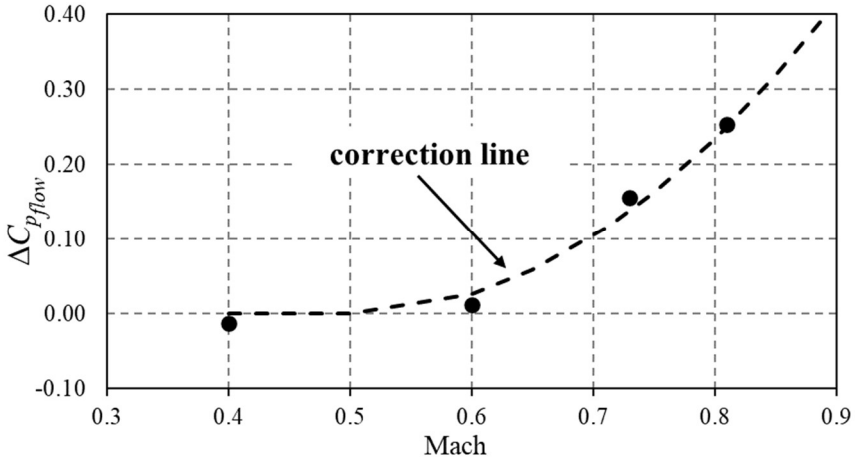

(b)

Figure 5.12 $C_{p_{flow}}$ differences between local values of the undisturbed flow and the probe readings at the same locations for the three incidences (a) and 0.375 of the pitch with increasing Mach number at zero incidence (b)

$$\Delta C_{p(0.375)} = C_{p(measured)} - C_{p(local)} \tag{5.5}$$

$$\Delta C_{p_i(0.375)} = 0.00105 \cdot i^2 + 0.011 \cdot i + 0.01 \qquad i \in (-5; 5) \tag{5.6}$$

$$\Delta C_{p_{Ma}(0.375)} = 2.6 \cdot Ma^2 - 2.6 \cdot Ma + 0.65 \qquad Ma \in (0.5; 0.8) \tag{5.7}$$

$$C_{p_{flow}(local)} = C_{p(measured)} - C_{p_i} - C_{p_{Ma}} \tag{5.8}$$

The correction of static pressures requires the knowledge of the flow angle at the inlet and the estimation of the Mach number. The flow angle is the first parameter obtained during data processing, and the correction for the angle is based on the probe's location only, so this data becomes available prior to pressure corrections.

Estimation of the flow Mach number can be based on the multistage CFD simulation of the compressor. This method was used in the current project and the simulated and measured values of the Mach number gave the uncertainty of the $C_{p_{flow}}$ values to within 2%. During a measurement campaign, the Mach number can be iterated: first, raw measured pressures are used to obtain a first guess of the Mach number, then the Mach number correction is used to obtain a corrected value of the $C_{p_{flow}}$, based on the updated Mach number that is calculated. This routine is less reliable as for some probe locations it tends to diverge, so a CFD simulation at the operating point of interest was found to be convenient.

Next, the difference between measured and local values will be discussed. This is done in the same sequence as the raw data of three-hole pressure probe readings is processed: first, the yaw angle, then the stagnation pressure and the dynamic head.

Flow angle measurements follow the general trend of the potential field upstream of the stator blades. It was found that the differences between the readings and the local flow angles at the probe location are less dependent on the flow condition, and all the points fall into the narrow region of ±1°. When comparing against the averaged value, the difference can reach up to 10°. Therefore, processing the measured values of the flow angles as local ones is more universal. The parabolic correction curve was described in Equation 5.2. In that case for the 20–70% of pitch, a measurement uncertainty of within ±1° from the local value of the flow angle can be expected. This is found to be the case for all the probe locations and flow regimes studied.

After correcting the reading to the local flow value, the latter should then be transformed to a representative pitchwise average number. Since the local flow distribution upstream of the stator is mainly caused by the potential field, the correction from local to mean flow value can be done by CFD simulation in the same way as coloured lines refer to the zero value in Figure 5.8 or similar plots.

Total pressure readings in front of the stator blades can be measured throughout the whole range of conditions studied. The spread of the measured values was well within 0.1% of the dynamic head. This can be explained by the uniform upstream total pressure due to the averaging downstream of the rotating blades. In addition, the middle hole of the three-hole pneumatic probe, which is mainly responsible for the total pressure measurement, is located upstream of all the loss sources of the stator blade row, therefore the impact of probe location is comparatively low.

Static pressure readings are sensitive to the flow angle and Mach number. A 5° incidence can cause the pressure measurements to deviate within ±5% from the local value, and if the uncertainty in the flow angle is ±1°, after the correction of the flow angle the measured pressure uncertainty will be within ±1% of the dynamic head after the correction.

For a flow Mach number lower than 0.6, the measured values follow the general trend of the potential field. At higher flow speeds the probe blockage significantly grows and affects not just the blade channel where the probe is immersed, but also the neighbouring channels. The dynamic head, therefore, is underestimated by more than 30%. Under these conditions, the differences are more uniform along with the pitch.

5.4 Measurement correction procedure

A schematic representation of the proposed measurement corrections procedure is shown in Figure 5.13. It has two steps: in the first, the measured value from the probe reading is converted to the local value of the undisturbed flow at the probe location. The second step is to convert the local value of the flow into a representative pitchwise-averaged flow parameter. In Figure 5.13 this procedure is shown for the probe location of 12.5% of the pitch.

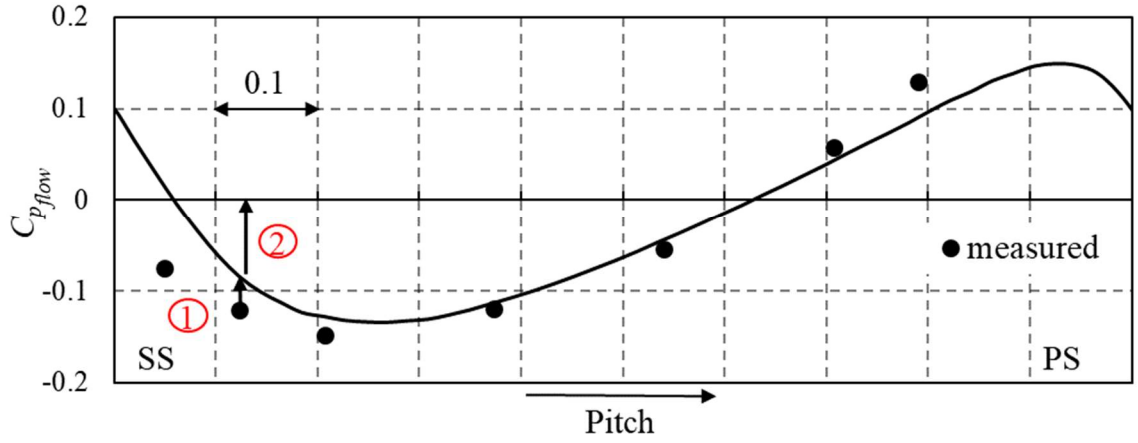

Figure 5.13 Schematic of the measurement corrections: (1) correcting measured value to the local value of the undisturbed flow, (2) calculating representative pitchwise-average value

The procedure relies on the knowledge of two flow fields: the one around the probe at location and flow conditions of interest, and the undisturbed flow field at the measurement plane in a real (in this case multistage) simulation at the right operating point. The former can be simulated for a range of locations and flow conditions expected during an experiment in a two-dimensional simplified setup, whereas the latter can be obtained from the multistage simulations used in the design process. The complete procedure is shown in Figure 5.14 with first and second steps expanded into bigger blocks. The routine for measurement corrections of the multistage axial compressor can be performed as follows:

1. Calculate a two-dimensional flow field at a location of measurements both with and without immersed probe. Cover the anticipated range of probe locations and flow conditions. In the presented research the ranges are significantly expanded to gain physical understanding of the processes and the limitations of the method. To do this a matrix of 10 locations by 9 flow conditions with some intermediate points for refined interpolation was studied for each measurement plane. For the real applications the number of simulations can be reduced.

2. Build a matrix of correction coefficients for Equations (5.4(5.8. For yaw angle measurement, the correction for circumferential position only is sufficient to obtain the remaining uncertainty of ± 1°. For static pressure measurements a three-dimensional matrix should be calculated: for each probe location, corrections for inlet flow incidence and then inlet flow Mach number are calculated. For all corrections, second-order, best-fit approximations were used.
3. Define the probe location along the circumference. Calculate the difference between the measured and the undisturbed flow angles using equation 5.2 and coefficients from the previous step. Calculated values of corrections are then added to the measured values. The resultant value represents the local flow angle value of the undisturbed flow at the location of the probe. This operation is illustrated as number 1 in Figure 5.13.
4. Use a representative multistage CFD simulation of the compressor at the operating point of interest to obtain circumferential distributions of the flow angle, as well as total and static pressures at selected spans at the measurement plane .
5. Calculate the difference between the pitchwise averaged value of the flow angle and the local one at the position of the probe. Add this difference to the corrected measured local flow angle from Step 3. This operation is illustrated as number 2 in Figure 5.13, where the black line represents the circumferential distribution, and zero at vertical axis is the average value. Now the pitchwise averaged flow angle value can be used in the design system; it can also be used to calculate corrections of static pressure measurements.
6. For static pressure measurement corrections, for a known probe location the corrections to the static pressure can be calculated using equations (5.5(5.8 using coefficients from Step 2 and known pitch position. First, the correction for the inlet flow incidence is applied, and then for the Mach number.
7. For Mach number corrections, an initial guess of an undisturbed Mach number is needed. In the current research, this was obtained from the representative multistage compressor CFD simulation. Otherwise, during experiment this guess can be calculated from the raw measured static and total pressures. For cases when the inlet Mach number is below 0.6, corrections for the Mach number can be omitted.

8. Check if the probe is at the location or flow conditions of high uncertainty. For locations beyond the recommended range (in this work it is 20–70% of the pitch), the data should be treated with care.

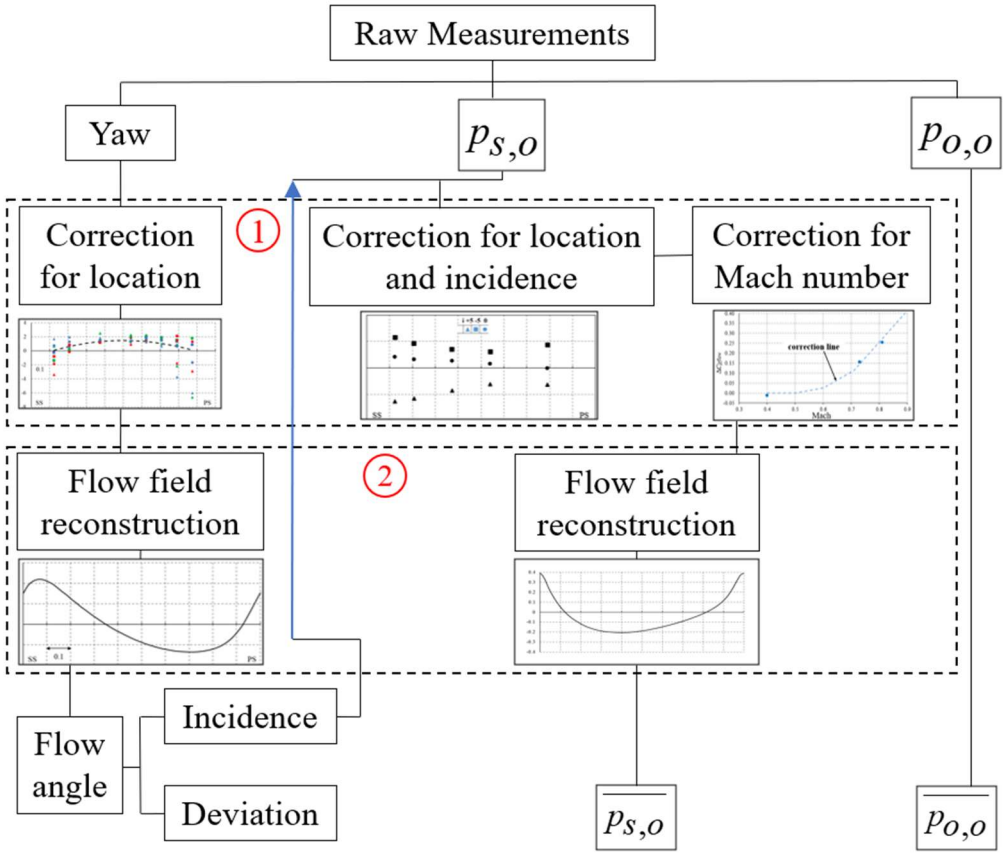

Figure 5.14 Corrections procedure for the probe measurements

This method is valid when probe blockage does not cause major radial redistributions of the flow: if probe blockage values are in the order of 5% of the blade pitch, two-dimensional corrections can be used.

The procedure was found optimal for experiments in multistage axial compressors designed with a repeating stage concept and for spanwise traversing at variable pitch locations of the probe. In this case, the number of 2D simulations in Step 1 of the method to cover the range of real flow conditions and probe locations is significantly smaller than 3D simulations of the full-span blade passages with various immersions and pitch locations of the probe.

If only a few individually designed stages are traversed at one or two radial lines, it might be more effective to simulate specific probe positions and flow conditions at full-span setup without the need for generalisation.

5.5 Measurements along the span

This section compares the circumferentially averaged and local parameters of the undisturbed flow at probe locations with the values measured by the probe moving along the radial trajectory at a given measurement section. To do this, several representative positions at mid-span, near the hub and near the casing, were simulated in a full three-dimensional setup. The actual probe and the stem were simulated inside the stator domain at the known pitchwise and axial position and immersion. The boundary conditions were taken from multistage compressor simulations.

Figure 5.15 shows the view on Stator 1 from the upstream with the probe placed at one of the locations of the real traverse, and the radial trajectory is shown in the broken red line. Similarly, the broken blue line shows another traversing trajectory for the second probe. The relative position of the probe is shifting towards the suction side when immersing downwards, so for example, when the probe enters the flow path near the casing at 34% of pitch (counting from the suction side), it reaches the hub at around 24% of the pitch. This is due to the blade twist according to the designed swirl distribution in the stage. At each probe location, the raw simulated probe measurements are shown first, then the correlations from section 5.3 are used to convert the measured values into the local ones, then the flow field from the three-dimensional setup is used to obtain pitchwise averaged value. The total pressures were processed without corrections, and the static pressure corrections were applied in the same way as the flow angle.

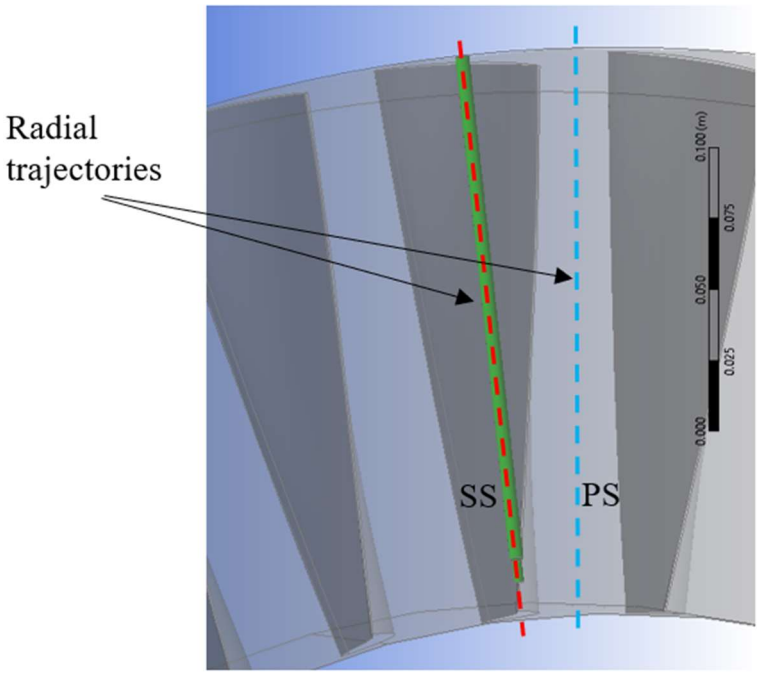

Figure 5.15 A probe simulated upstream of the stator domain, immersed at 90% of the span at a pitchwise position of the real probe.

Figure 5.16 (a) shows the spanwise distribution of the flow angle in terms of blade incidence. Zero on the horizontal axis means zero incidence into the blade row at a given span. The black solid line in Figure 5.16 (a) represents the circumferentially averaged value at each span location. The broken blue and red lines are the local values of the undisturbed flow from 3D CFD setup where the colours correspond to the trajectories from Figure 5.15. Two sample measurements simulated with the immersed probe are shown in dots for the location at midspan and pitchwise locations of 29% and 71%, counting from the pressure side.

In Figure 5.16 (b) the two-dimensional distribution along the pitch is shown for the full-span setup at mid-span slice. The black line here represents the local undisturbed flow value, and the points give the readings of the simulated immersed probe.

For 29% of pitch, the measured value is 1.42° larger than the averaged undisturbed value, whereas local undisturbed value is 0.32° lower than the averaged one. When applying Equation 5.2 for a given pitch, the correction value is 1.62°, meaning that the corrected local value would be 0.12° higher than the undisturbed one:

$$1.42° - 1.62° = -0.2°; \quad -0.2° - (-0.32°) = 0.12°$$

For the blue points the difference is: -3.4° for the measured value compared to the averaged, and -5.03° - for the local. The amount of correction from Equation 5.2 is 1.72° which when applied to -3.4° results in -5.12°, or 0.09° lower than the local value. This shows how the corrections from Equation 5.2 can be applied to obtain local undisturbed flow angle from the measurements. It is important to note that Figure 5.16 (b) is built for a full three-dimensional setup, but the corrections are calculated from the two-dimensional cases summarised in Section 5.3 and these corrections improved the uncertainty from 1.7° down to ±0.1°.

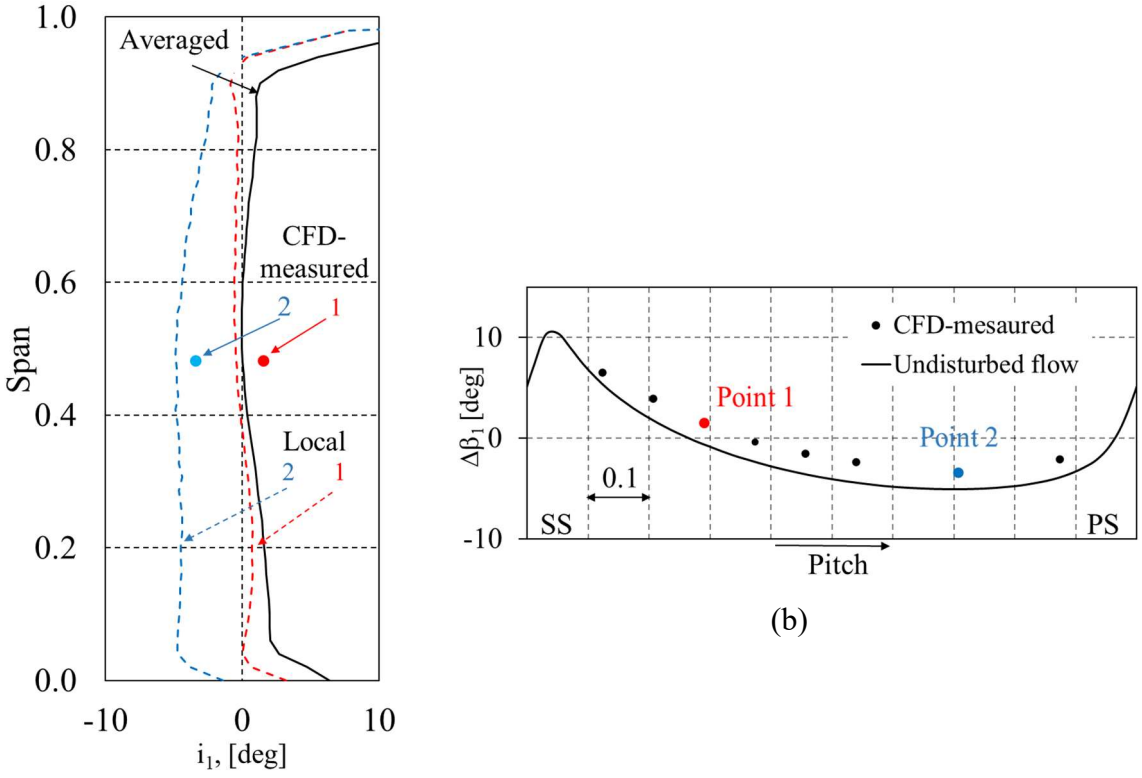

Figure 5.16 Spanwise distribution of the flow angle at given trajectories and pitchwise averaged (a) and pitchwise flow angle distribution at middle span and the probe readings at two traverse locations (b)

Figure 5.17 (a) shows the pressure measurements upstream of the stator for the same trajectories and two spanwise locations of the probe. Again, the broken lines show the local values of the undisturbed flow and the points of the same colour show the measurements of the

simulated immersed probe at given locations. The black line shows the pitchwise averaged value. Zero value at the horizontal axis is equal to the C_{pflow} value of the flow at the mid-span.

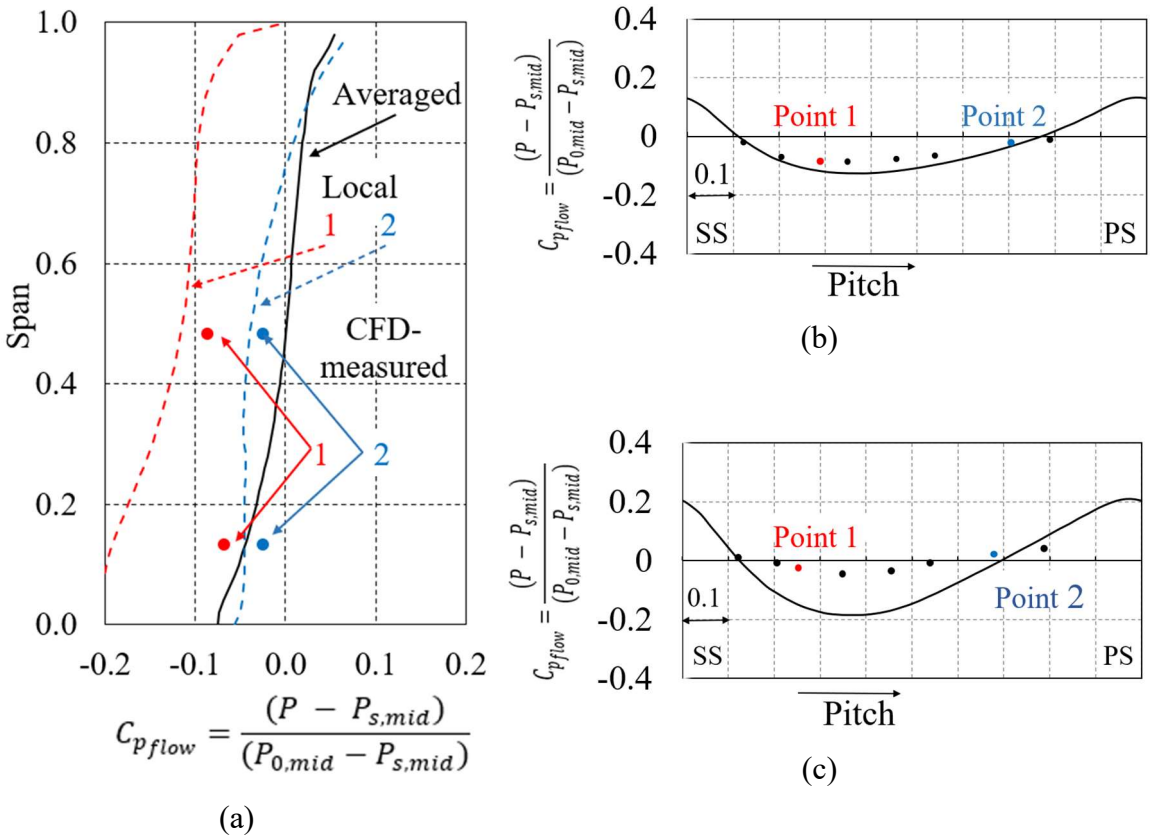

Figure 5.17 Pressure upstream of the stator at two radial traversing trajectories and the circumferentially averaged values, together with two sample measurements from 3D CFD (a), and circumferential distributions for two given spanwise locations: 50% span (b) and 14% span (c)

The two radial positions of the measurements are now shown for 14% and 50% of the span. This is to illustrate the difference in measurement corrections when reaching the critical Mach number: at the midspan the value is 0.652 and at the 14% span it is 0.712. Figure 5.17 (b) and (c) show the circumferential distributions of the C_{pflow} values at each given span and the probe measurements at the same span and selected locations along the pitch. Zero on the vertical axis equals pitchwise averaged C_p at the given span.

The correction procedure from Section 5.4 can now be applied for the C_p values of the flow. As shown in Figure 5.16 (a), the average flow incidence at the measurement plane is 0° at mid-span and 1.6° for 14% of the span. Table 5.3 provides correction coefficients for Equations 5.4–5.5 at given pitch locations and flow conditions. Table 5.4 compares raw and corrected values with the undisturbed ones. Mach number values along the span are taken from the multistage simulation—the same conditions that were used for the full span simulation with the immersed probe. The corrections are then subtracted from the measured values as shown in Equation 5.6.

Table 5.3 Coefficients for Equations 5.4–5.5 at given pitch locations of the probe

Locations	Corrections for incidence				Corrections for Mach			
	C_{2i}	C_{1i}	C_{0i}	$\Delta C_{p_{probe}}$	C_{2Ma}	C_{1Ma}	C_{0Ma}	$\Delta C_{p_{probe}}$
Traverse #1	-0.0008	0.0088	0.014		6.05	-6.85	1.92	
50% of span				0.0140				0.0336
14% of span				0.0260				0.1098
Traverse #2	0.00001	0.0059	0.0011		2.91	-3.58	1.11	
50% of span				0.0011				0.0024
14% of span				0.0104				0.0265

Table 5.4 $C_{p_{flow}}$ values of undisturbed flow and the measured values

Span	50%		14%	
Pitch	29%	71%	25%	76%
Averaged value	0		-0.043	
Local undisturbed	-0.115	-0.033	-0.196	-0.037
Measured	-0.082	-0.031	-0.069	-0.022
$\Delta C_{p_{probe}}$ for incidence	0.014	0.001	0.026	0.010
$\Delta C_{p_{probe}}$ for Mach	0.034	0.002	0.110	0.027
Corrected value of C_p	-0.130	-0.034	-0.205	-0.059
Difference between the measured corrected and undisturbed values	-0.015	-0.001	-0.09	-0.022

At the midspan and subcritical Mach number, the measured $C_{p_{flow}}$ is 3.3% higher than the local value, meaning that the predicted dynamic head will be 3.3% lower. At the same time,

the local C_{pflow} is 11.5% lower than the pitchwise average. For 71% of the pitch the measured value is 0.4% higher than the local undisturbed one, which, in turn is higher than the pitchwise average by 3.5% of the dynamic head.

For the Mach number of 0.712 and 26% of pitch (the pitch is now corrected following the radial line of the probe trajectory), the probe measures a value close to the average one, whereas the local undisturbed value is 19.3% lower. For 67% of the pitch the differences are still within 4%, because in Figure 5.17 (c) the distribution line of undisturbed flow values crosses zero and the measured values were found to be in proximity to the ones in the undisturbed flow. As a result, the corrected values are within 2.2% of the dynamic head from the local ones, compared to up to 13% difference without correction. The highest uncertainty is for the 14% span and 67% pitch.

Local C_{pflow} values are then transferred to the averaged ones using the local undisturbed flow value, shown as black lines in Figure 5.17 (b) and (c). For each circumferential position the value on the black line is subtracted from the local value of the flow, which in case of the undisturbed flow will transfer all the points along the circumference down to the horizontal line at zero on the vertical axis. Since the operation is linear, any error in calculation of the corrected measured value will be translated into the error in the pitchwise averaged one.

Figure 5.16 and Figure 5.17 show the measured values only. In Figure 5.18 the measured and corrected values are shown for multiple points along the span. Figure 5.18 (a) and (c) show the same distributions as Figure 5.16 and Figure 5.17 with more points on them. Figure 5.18 (b) is the total pressure distribution shown in the form of C_{pflow} coefficient where 1.0 at the horizontal axis means the total pressure at the midspan.

As a result, measured flow angles, which were up to 5° away from the pitchwise averaged were corrected to lie within 1° of the pitchwise averaged values. The total pressure was not corrected, and it proved to be within a range of 1% of the dynamic head away from the pitchwise averaged values.

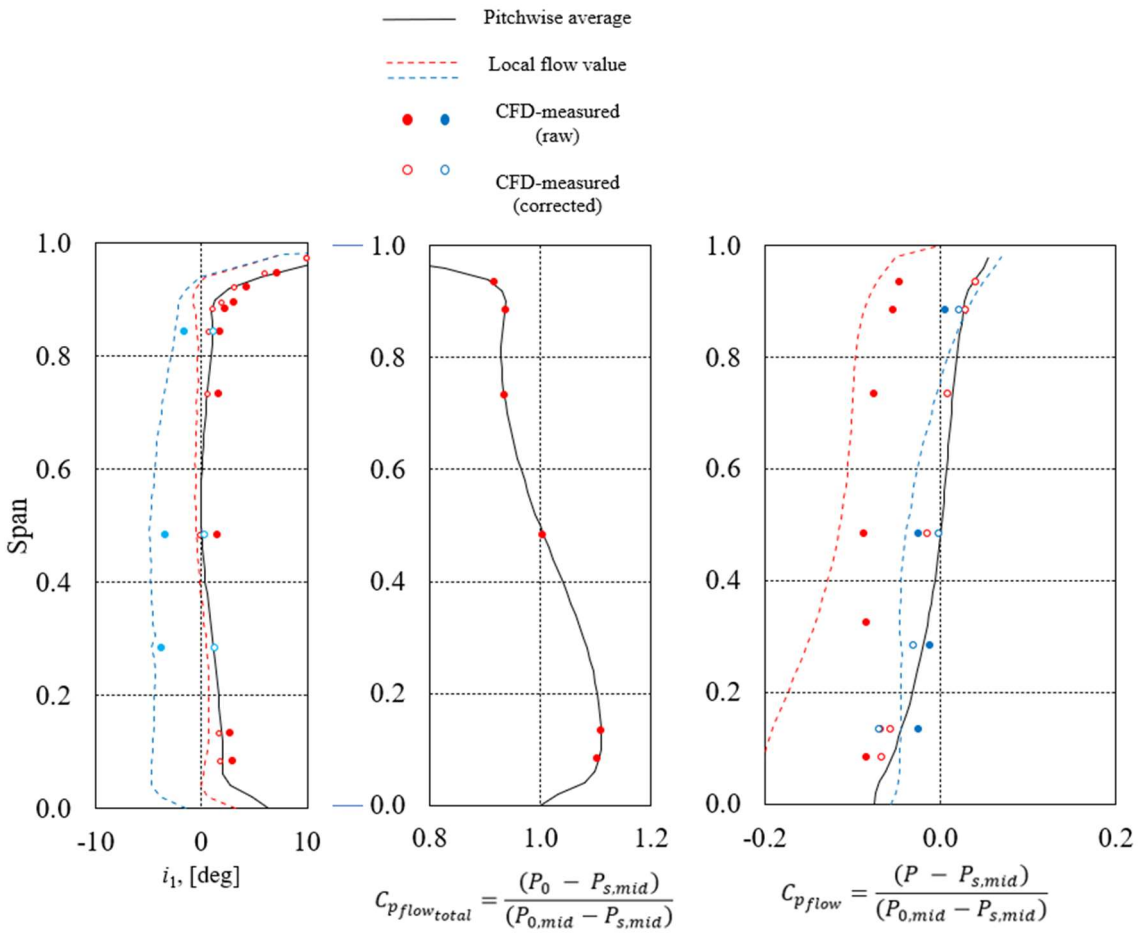

Figure 5.18 Measured raw and corrected values along the span at two traversing trajectories: flow angle (a), stagnation pressure coefficient (b) and static pressure coefficient (c)

The measured static pressures, if considered without corrections, would show a negative or zero pressure gradient along the span, which is particularly well seen with red dots at the bottom half of the span in Figure 5.18 (c). This contradicts the nature of the flow: the swirl downstream of a rotor implies a strong positive pressure gradient to satisfy radial equilibrium. When corrected, both blue and red dots align with the line of the undisturbed flow within 2.5% of the dynamic head at mid-span. However, the applied corrections were found to be very sensitive to the fine position of the probe and the real geometry of the channel, so when similar correlations were used for other blade channels, the uncertainty of the pressure readings rose

to 5%, which is still less than that of the raw data. Therefore, for static pressure corrections, every blade row operating near the critical conditions must be simulated at given flow conditions to obtain the right correction value. The example in Figure 5.16–Figure 5.18 shows how the correction procedure can be used to give sensible results even in the constrained environment of real gas turbine engines.

5.6 Concluding remarks

In this Chapter, the mechanisms affecting the probe measurements were explored. When the probe is immersed upstream of the stator, it measures the local parameters of the distorted flow in an environment different from the probe calibration facility.

The probe acts as a blockage to the flow; in particular it changes the flow direction and causes the flow to redistribute to the neighbouring channels. When the probe is in the middle of the pitch, for the case studied, the bulk flow around it has a 2–3° higher flow angle than in the undisturbed flow.

The difference between the calibration and real flow environments, referred to here as a flow asymmetry around the probe, causes a 1–2° change in the measured angle when the three pressure readings are processed with the freestream calibration coefficients. For the middle of the passage, this effect brings the measured results closer to the ones of the undisturbed flow. The side holes of the probe are affected the most. This limits the sensitivity range of the probe to ±20° compared to ±25–30° at freestream calibration.

Proximity to the blade surface causes extra acceleration near the probe surface and shifts the separation point further down its circumference. These effects lead to increased uncertainties of the measured flow angle and pressure, especially at high blade incidences. For example, when the probe is placed near the pressure side of the blade, its wake can interact differently with the leading edge of the blade depending on the angle of the upstream flow. The correction for these effects is limited by the uncertainties in CFD modelling of the large vortical structures around and downstream of the probe.

The low measurement uncertainty region is 20–70% of the pitch, and the parabolic correction can be applied to the flow angle measurement to obtain a local parameter of the undisturbed flow. When applied, the difference between measured and local flow angles was

reduced to ±1°. Static pressure measurements need to be corrected for the probe's position, the inlet flow angle, and the Mach number. The initial difference with the undisturbed values can be more than 20% of the dynamic head. When the corrections are applied, for subcritical flows the uncertainty is reduced to ±5%.

Chapter 6 Probe placed downstream of stators

In this chapter, measurements downstream of stator blade rows are considered. In the first part the flow features affecting the probe measurements are discussed. Then a set of quasi-two-dimensional simulations are presented to understand at what probe locations along the circumference the measurements can be trusted and corrected if necessary, and to understand the key mechanisms affecting the measurement uncertainties. This is followed by full-span simulations of the probe downstream of Stator 1. It will be shown that even in presence of large corner separation zones in the stator, the measurements in a wide region at the middle of the blade channel can have low uncertainties.

The list of the test cases studied in Chapter 6 is given in Table 6.1. For simplicity, only one radial traverse is shown in this chapter, however the findings are supported by full-span calculations with the probe at all the planes of the real measurements.

Table 6.1 List of test cases in Chapter 6

Blade row	Locations	Flow conditions
S9 downstream	5 circumferencial Quasi-2D	3 incidences 3 Mach numbers (9 total)
S1 downstream	1 radial trajectories 5 locations along the span	1 operating point of the compressor

6.1 Differences with measurements upstream of stators

When the probe is immersed downstream of a stator blade row of a multistage compressor, there are several fundamental differences to the measurements upstream of stators that make it hard to obtain reliable readings and make use of this data.

First, the probe upstream of the stator sees circumferentially averaged flow in front of it. In this case, for steady flow measurement total pressures and flow angles have constant values along the circumference of the stator. Static pressure distribution reflects the potential pressure field of the downstream blades. Downstream of the stator, the flow before the probe is not circumferentially averaged, and the total pressure and flow angle will not be uniform. However, the static pressure distribution will be uniform, except in blade wake regions.

Second, the flow upstream of stators is dominated by potential flow field effects and the rotor wakes, and leakage flows are effectively time averaged, whereas downstream of stators there are still potential field effects. But it is the vortical structures that play a significant role in the flow field, and the probe interaction with the boundary layers, separation zones and blade wakes introduces further complications and uncertainties in measurements. The reliability of CFD modelling of the viscous effects is also less robust than that of the potential field, so a case-to-case comparison between the real measurements and the CFD at each particular probe location and operating point can be less accurate.

In addition, for a multistage compressor, the limitations in space make circumferential traversing downstream of stators difficult, and this process is commonly used for laboratory-scale research compressors. Even if it was technically achievable, the flow parameters measured in proximity to the blade wakes cannot be treated as undisturbed flow values, which will limit the practical use of this data. Moreover, for industrial gas turbines tested on site, milling a wide circumferential slot in proximity to stator blade roots raises serious concerns about structural integrity and the lifecycle of the casing during further engine operation after the tests.

6.2 Two-dimensional setup

Figure 6.1 (a) shows a typical flow in a stator blade channel. The red line shows the axial plane where the probe is immersed, which is at 10% of the blade chord. Figure 6.1 (b) and c) show respectively the flow angle distribution along the circumferential direction and the distributions of $C_{p_{flow_{total}}}$ – a measure of local total pressure divided by the pitchwise average:

$$C_{p_{flow_{total}}} = \frac{(P_0 - P_{s,ave})}{(P_{0,ave} - P_{s,ave})} \tag{6.1}$$

The flow is moving more axially near the suction side and more in a circumferential direction closer to the pressure side. The dynamic head of the flow can be considered equal to $C_{p_{flow_{total}}}$ as the static pressure distribution is within 3% uniform along the circumference, and the flow speed is the square root of the dynamic head. The flow speed is uniform along the pitch with slightly higher values near the suction side; however, the main flow feature here is the drop in dynamic head in blade wakes. Similar to the figures in Chapter 4, the measuring points on these graphs are CFD-measured and the line represents the undisturbed flow values.

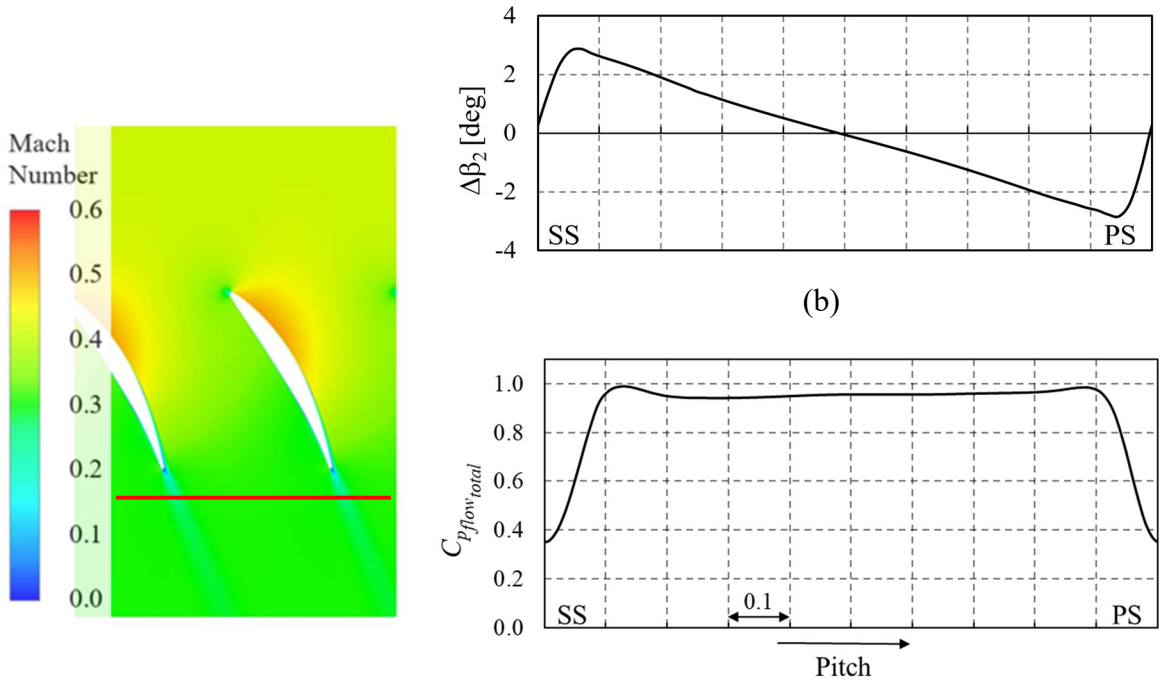

(a) (b) (c)

Figure 6.1 Typical contours of Mach number in stationary blade row (a) and circumferential distribution of the flow angle (b) and the $C_{p_{flow_{total}}}$ value (c) downstream at a distance of 12.5% of the pitch downstream of the blade row

Figure 6.2 shows the streamlines (left-hand side) in the channel and around the probe, and the $C_{p_{probe}}$ distributions around it (right-hand side). Here, the probe is oriented along the designed flow direction. The streamlines show that the probe's blockage interacts with the upstream flow, causing the streamlines to deflect. Near the suction side, the additional blockage causes most of the flow to go around the probe towards the pressure side, which reduces the local flow angle compared to the undisturbed case. When the probe is approaching the pressure side, the flow around it is being pushed towards the wake region, and at some point, the local flow will be deflected towards the circumferential direction (see Figure 6.2 (c) left).

The black lines in Figure 6.2 on the right-hand side represent $C_{p_{probe}}$ distribution at the freestream calibration with the same Mach number as in the undisturbed flow at the location of the probe. This line is given here for reference, so the reader can visually compare the actual pressure distribution around the probe with the one from the freestream jet of equivalent averaged velocity. All three $C_{p_{probe}}$ distributions show extra velocity on sides compared to the calibration curve based on local parameters. What is more important, is that the reading of the central hole p_2 somehow exceeds the value of 1.0, which means that the total pressure will be measured larger than the average one. This is due to the fact that in the core subsonic flow there are no major loss sources and the local total pressure downstream of the stator will be close to the values upstream, whereas the averaged total pressure will have to include the wake region, therefore it will be somewhat lower. Using the total pressure upstream of the blade row for reference can therefore provide values less biased by the size of the wakes and the probe position in proximity to them.

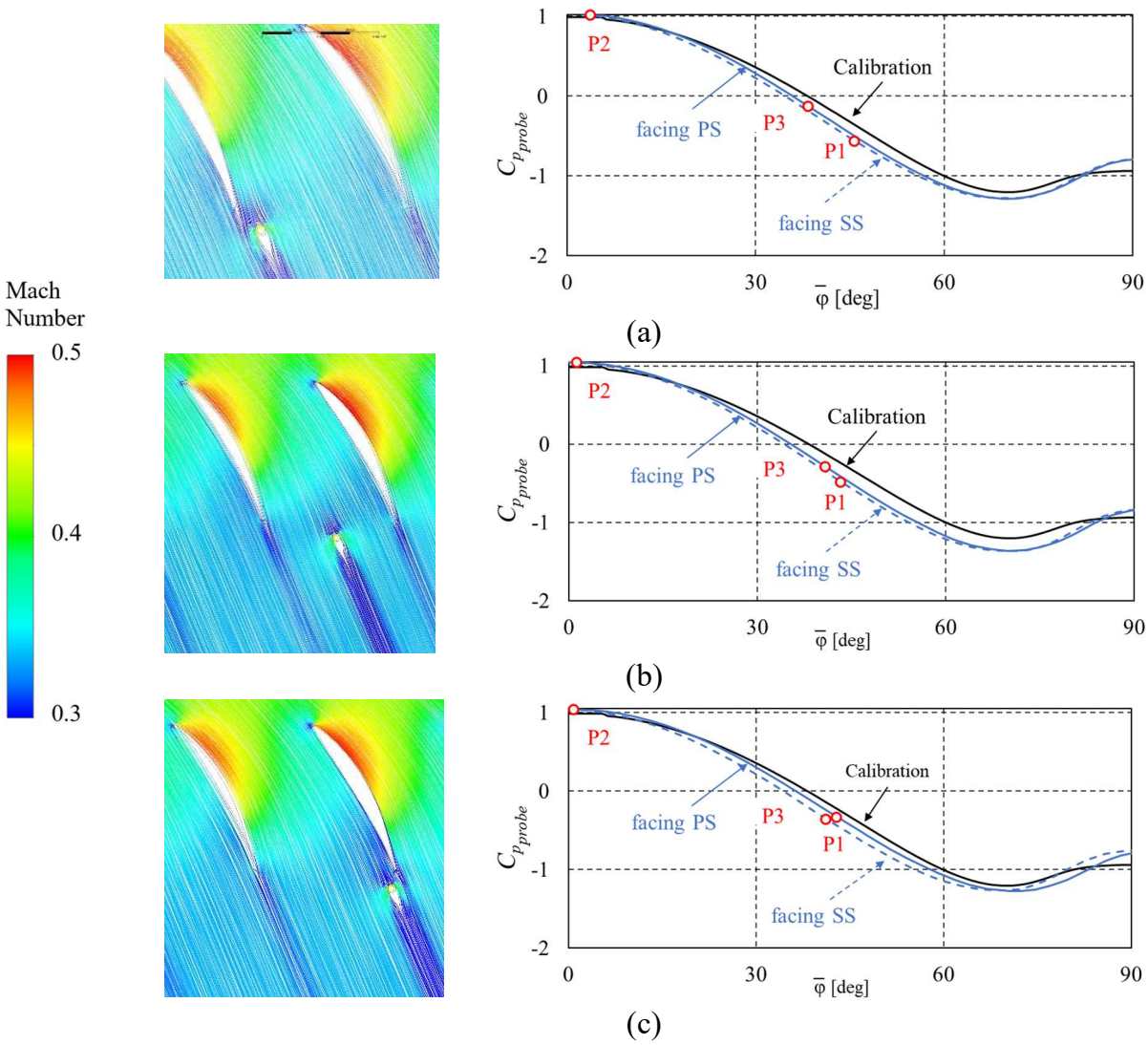

Figure 6.2 Streamlines around the probe downstream of stator blades (left) and $C_{p_{probe}}$ distributions around the probe (right) for the probe near the suction side (a), mid-pitch (b) and near the pressure side of the blade (c)

Figure 6.3 shows the flow angle distribution along the pitch for the undisturbed flow as a solid line and the probe measurements at given locations in black dots. Zero at the vertical axis means the mass flow averaged value, and the positive values mean more axial flow. Near the suction side, the undisturbed flow is more axial until 5% of the pitch where the wake effects take place. However, the probe deflects the flow in the circumferential direction; therefore, it measures less axial flow, or in turbomachinery terms the probe will be measuring extra

deviation downstream of the blade passage. In proximity to the pressure side the same happens due to the flow being pushed towards the wake. However, in the whole range excluding the point at 95% of the span, the measured angle is within ±1° from the mass flow averaged one.

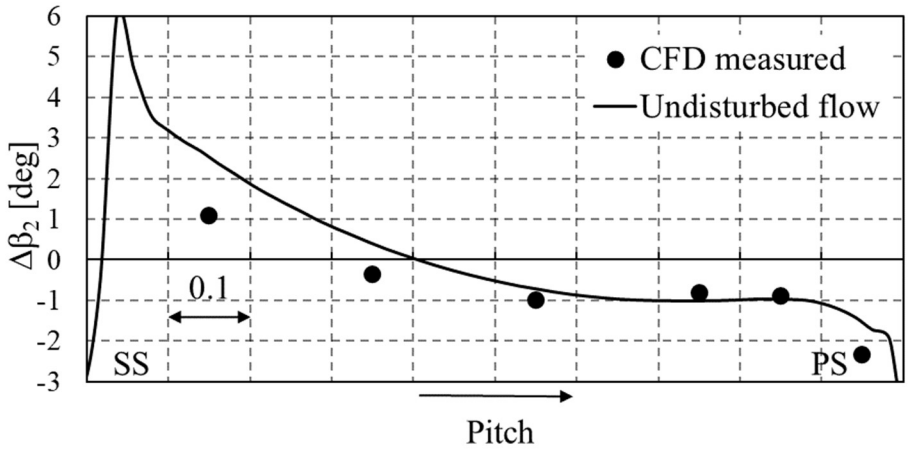

Figure 6.3 Flow angle distribution downstream of the stator and the probe measurements at the same axial plane

The pitchwise pressure distribution downstream of stators is largely dependent on the size of the separation zones, therefore it is preferable for the measurements to be transferred straight to the pitchwise averaged values directly, without using CFD simulations. Calculations at selected flow conditions are provided in the next sections to assess the validity of this approach.

Measured and undisturbed values of the total pressure are shown in Figure 6.4. Here, a value of 1.00 means the total pressure of the undisturbed flow upstream of the stator. The solid line shows an undisturbed flow field with the dots as the probe measurements. The broken line at 0.981 is the mass flow averaged total pressure downstream of the stator. Apart from the probe location of 15% of the pitch, the rest of the measurements show the values within 0.5% of the dynamic head away from both local and inlet averaged total pressures. However, the conversion directly into the mean value would simplify the data processing and the total pressure away from the blade walls can be treated as the total pressure of the core flow and expected to be equal to that at the blade inlet. This can be used as a measure of consistency of the experimental data during the real testing: if the measured total pressure downstream of

stator does not agree with the one measured upstream, this can be a signal that the probe is affected by the vortical structures, and the measurements at this location cannot be trusted.

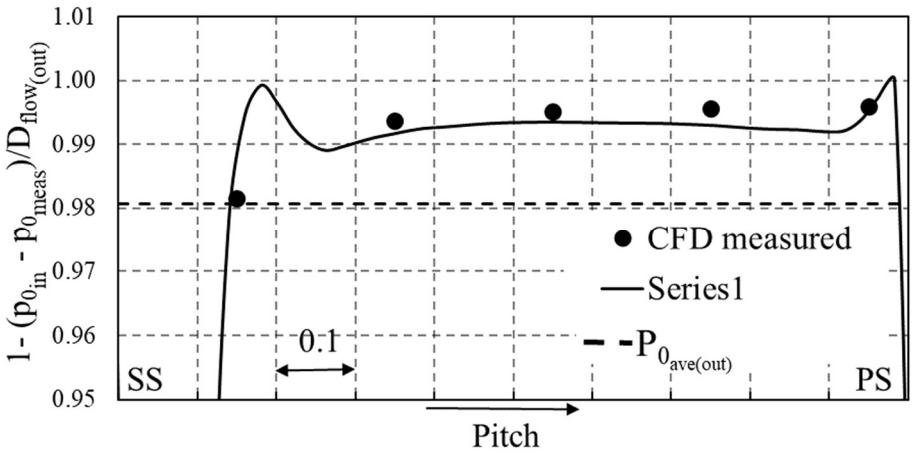

Figure 6.4 Total pressure distribution downstream of the stator and the probe measurements at the same axial plane

The values of $C_{p\,flow}$ as representative of the static pressure are shown in Figure 6.5. Here, a value of 0.0 means the averaged C_p downstream of the stator, and positive values mean higher pressure and lower dynamic head. The measured values follow the trend with a 2–4% overestimation of the dynamic head. In this case the difference in the averaged value reaches up to 7% and conversion directly to the mean value can be problematic.

Considering that the probe-diameter-to-pitch ratio is about 5%, then the overestimation of the dynamic head is comparable to the probe blockage, although the mechanism of such a difference is not straightforward. As was shown in a simplified case in Chapter 4, when the probe is immersed in a channel with solid walls, it causes a blockage and results in a faster speed around the probe. For a set of geometrical parameters identical to the case of a downstream probe, the blockage should cause an increase in dynamic head by 7–8%. Probe interaction with the complex flow field reduced this difference down to 4%.

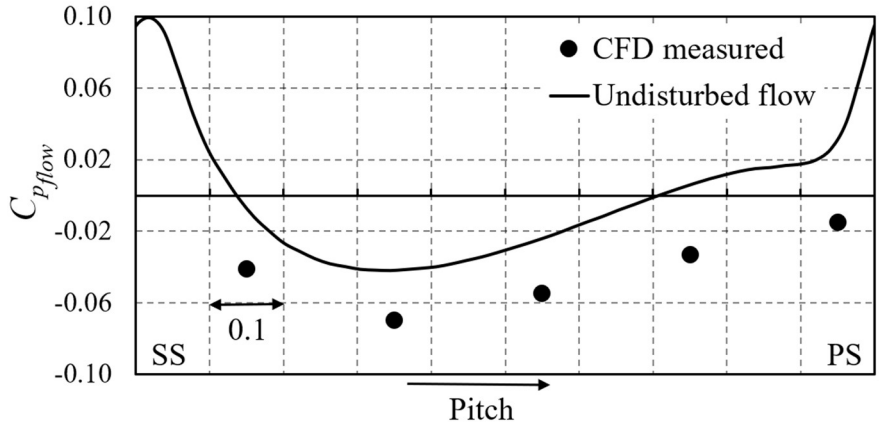

Figure 6.5 $C_{p\,flow}$ distribution downstream of the stator and the probe measurements at the same plane

This difference is illustrated in Figure 6.6 in terms of a delta in the Mach number of the undisturbed flow and the one with the probe:

$$\Delta Ma = Ma_{undisturbed} - Ma_{probe} \tag{6.2}$$

Red indicates values when the undisturbed flow is faster than the one with the probe. The light blue colour in the blade channel of interest shows that there is about a 0.0125 difference in the Mach number, which means about 3% of the undisturbed flow Mach number downstream of the stator. With an increasing Mach number, the probe blockage is expected to grow; the probe will be measuring higher static pressure, and the readings will be more uniform across the pitch, similar to the observations in Chapter 5, Figure 5.9.

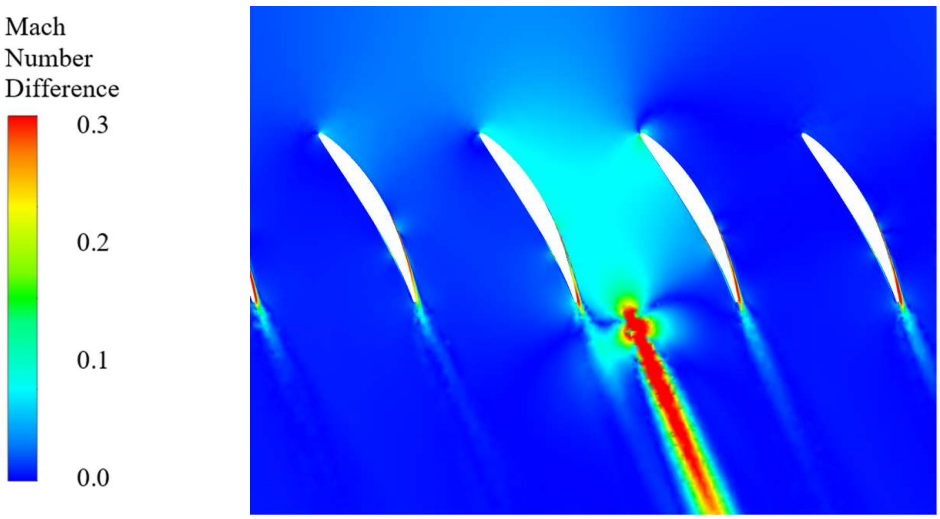

Figure 6.6 Difference in Mach number across the blade channel without and with the probe. Red indicates faster speed in the undisturbed flow compared to the one with the probe

In summary, for the measurements downstream of stators at design flow conditions the measurements of the flow angle along the pitch fall into one line with a ±1° offset from the mass flow averaged value. The total pressure measurements in the core flow give the numbers very close to the inlet total pressure and the dynamic head is overestimated by the values of 1–3%, which is comparable to the area blockage of the probe. In the next section the flow in the blade row will be studied at a high incidence

6.3 Probe placed in separated flows

In previous sections of the chapter, the flow downstream of stators was investigated at the design operating point with no major separations on the suction side. Figure 6.7 shows the flow angle distributions in the same way as in Figure 6.3, but for the operating conditions with the presence of a separation zone on the suction side. This was achieved by applying boundary conditions with a 7° incidence at the stator inlet. To understand the reasons for the measurement deviations, Figure 6.8 shows all three pressure readings of the probe independently. The measurement at 15% of pitch is omitted from the consideration due to its unrealistic value — all three pressure holes are placed in the separation region and all three points measure values

within 10% of the dynamic head; the measured angle is more than 30° away from the undisturbed value. At a 35% pitch the measured angle is 2° more than in the undisturbed flow, and this point does not follow the general trend. The value from the middle hole, P_2, which would normally be close to the total pressure, is falling towards the other two readings when approaching the suction side. This means that the probe is placed in the separation region and the pressure around it essentially equals the static pressure in the field. At 35%, the P_2 reading is already lower than the average inlet total pressure by 20% of the dynamic head.

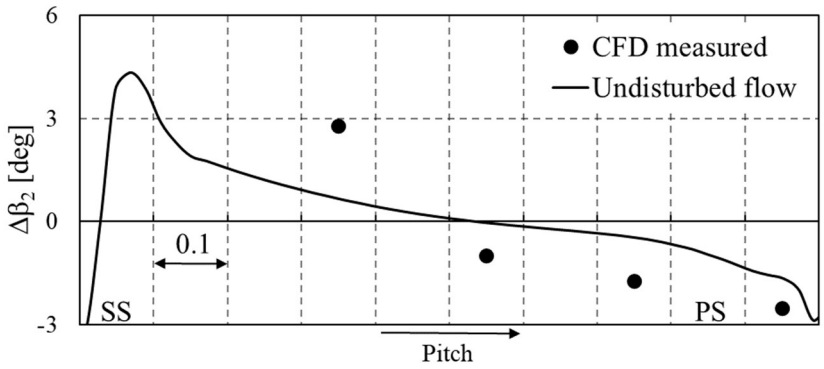

Figure 6.7 Flow angle distribution downstream of the stator and the probe measurements at the same axial plane for the case of flow separation on the blade suction side

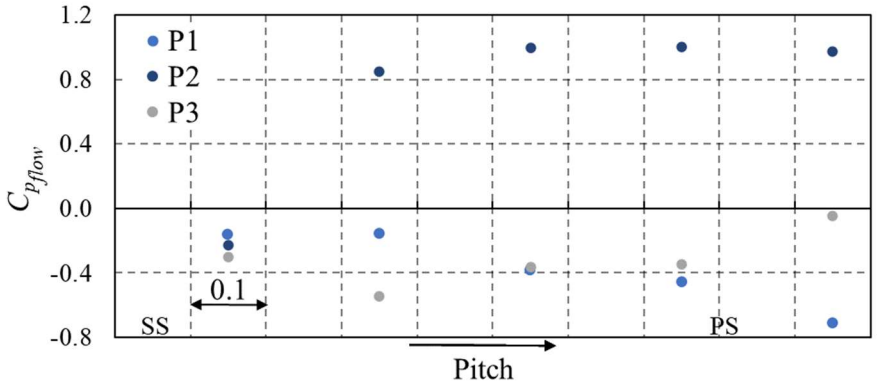

Figure 6.8 Pressure readings on three holes of the cylindrical probe

In a real measurement environment of a multistage axial compressor, the probe's pitchwise position will vary while the probe moves along the span, so for an experimental engineer the readings of the central hole, p_2, can be used to judge the reliability of the data. If the measured value is lower than the stator upstream total pressure by more than the anticipated total pressure loss in the core flow, then the measurements are likely to be of high uncertainty.

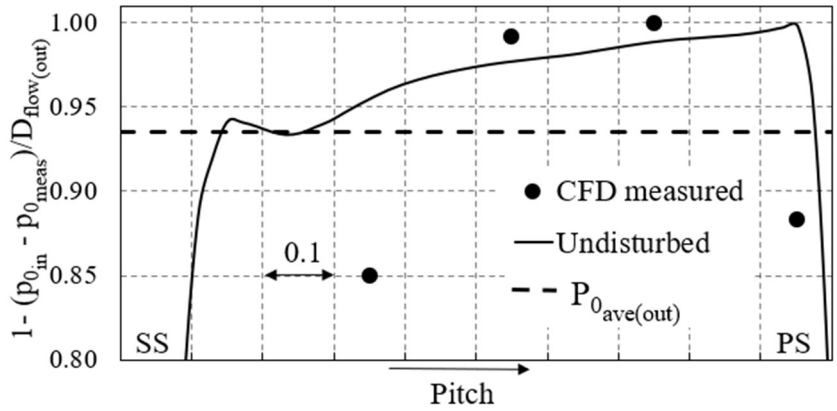

Figure 6.9 Pitchwise distribution of the total pressure downstream of the stator in the case of flow separation on the blade suction side

Figure 6.9 shows the total pressure distribution along the pitch between the two stator blades. Only two readings—55% and 75% of the pitch—show values close to the inlet total pressure and the values follow the general trend of the undisturbed flow. It is important to note that, while measuring a significantly lower total pressure at 35% and 95% of the pitch due to probe interaction with the wake, the measured angle errors are similar to those in the freestream (±2°). A series of calculations have shown, however, that the measured angle in such regions is highly uncertain, as all three pressure readings can be close to each other and the error can exceed tens of degrees.

CFD-measured C_p values of the flow are shown in Figure 6.10 with the solid line to represent an undisturbed flow and the points are the probe measurements processed with the freestream calibration coefficients. Overall, the values show a 6–10% larger dynamic head than the undisturbed flow. As shown in Figure 6.8 when the probe is inside the separation region, all three holes measure the pressure close to the static pressure in the channel. However, due to

the presence of the probe, the static pressure in such a channel with and without the probe will be different and, for example, the measured pressure at 35% of the pitch is more than 20% lower than the undisturbed value.

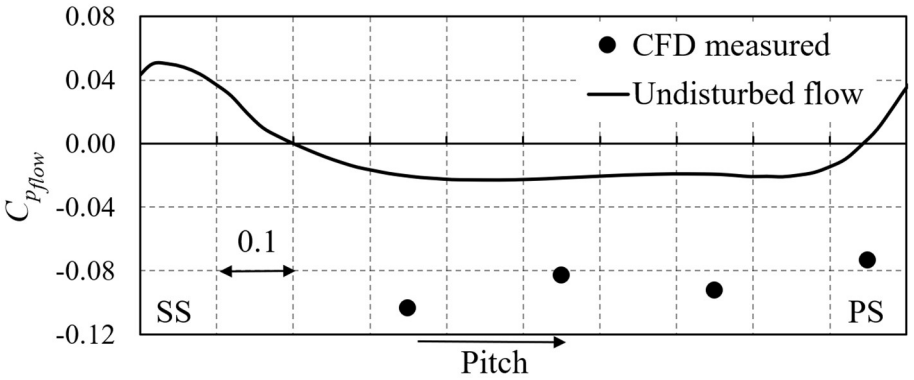

Figure 6.10 $C_{p\,flow}$ distribution downstream of the stator and the measurements at the same plane in the case of flow separation on the blade suction side

When measurements were taken in the separated flow downstream of stators, the readings could no longer be used for comparisons against CFD calculations, or to make any decisions regarding compressor design. Two questions arise: first, how the measurements in the separation zone can be identified during the experimental campaign, and second, what would happen in a three-dimensional flow when the probe is away from the separation, but the stem interacts with it?

6.4 Measured and local undisturbed flow parameters

As a result of the simulations at representative probe locations and flow conditions, Figure 6.11 shows the differences between CFD-measured and local values of the flow. Now the vertical axis shows the difference between the average flow value and the ‘measured’ one, so zero on the vertical axis means averaged flow. The probe measurements downstream of the stator are within a comparable distance from both the local values and the average ones. For example, measured flow angles are within 1–2° away from both local and averaged values.

The range within which the measurements are least affected by interaction with the blade walls, lies between 30% and 80% of the pitch, which is slightly different from the upstream measurements studied in Chapter 5. This is because of the stronger vortical structures on the suction side, which are not seen when the probe is measuring upstream.

The major contribution to the measurement uncertainty is the interaction with the wake region when the probe is either near the suction side or the pressure side of the blade. In both cases one of the side holes is measuring pressures far away from its freestream calibration performance so that the resulting measured flow parameters become unrealistic; the error could exceed tens of degrees in the flow angle and reach up to 100% of the dynamic head. This becomes especially critical when the flow conditions are close to separation on the suction side because the presence of the probe can change the flow pattern from stalled in the undisturbed case to unstalled with the probe.

Flow angle measurements follow the general trend of the flow field downstream of stators. In Figure 6.11 (a) such conditions are at a high positive incidence of the blade row (triangles for all three Mach numbers) and high outlet Mach numbers (all red symbols). For other flow conditions, measurements between 30 and 80% of the pitch can be referred to as the representative average value within a $\pm 1^{o}$ uncertainty.

Total pressure measurements downstream of the stator blades can be performed in the same region at the mid-pitch, and the measured values will be close to that upstream of the blades. This is due to minimal pressure losses occurring in the core flow. When the probe is approaching either side of the blade passage, its readings become unreliable due to one of the holes being largely affected by the separated flow, so even if full two-dimensional traversing in both pitchwise and spanwise directions was technically possible, it would not be physically correct to integrate the measured values into a representative total pressure loss coefficient. Therefore, the spanwise traversing downstream of the stator cannot be used to measure mass-flow-averaged stator losses. Instead, it can only be used as a measure of the flow conditions at the point of the measurement, and if the measured total pressure is within 1% of the upstream value, then all three probe holes are placed in the unseparated flow with no major loss sources present at a given blade passage, so the other two flow metrics, namely the flow angle and the static pressure, can be trusted within acceptable uncertainty.

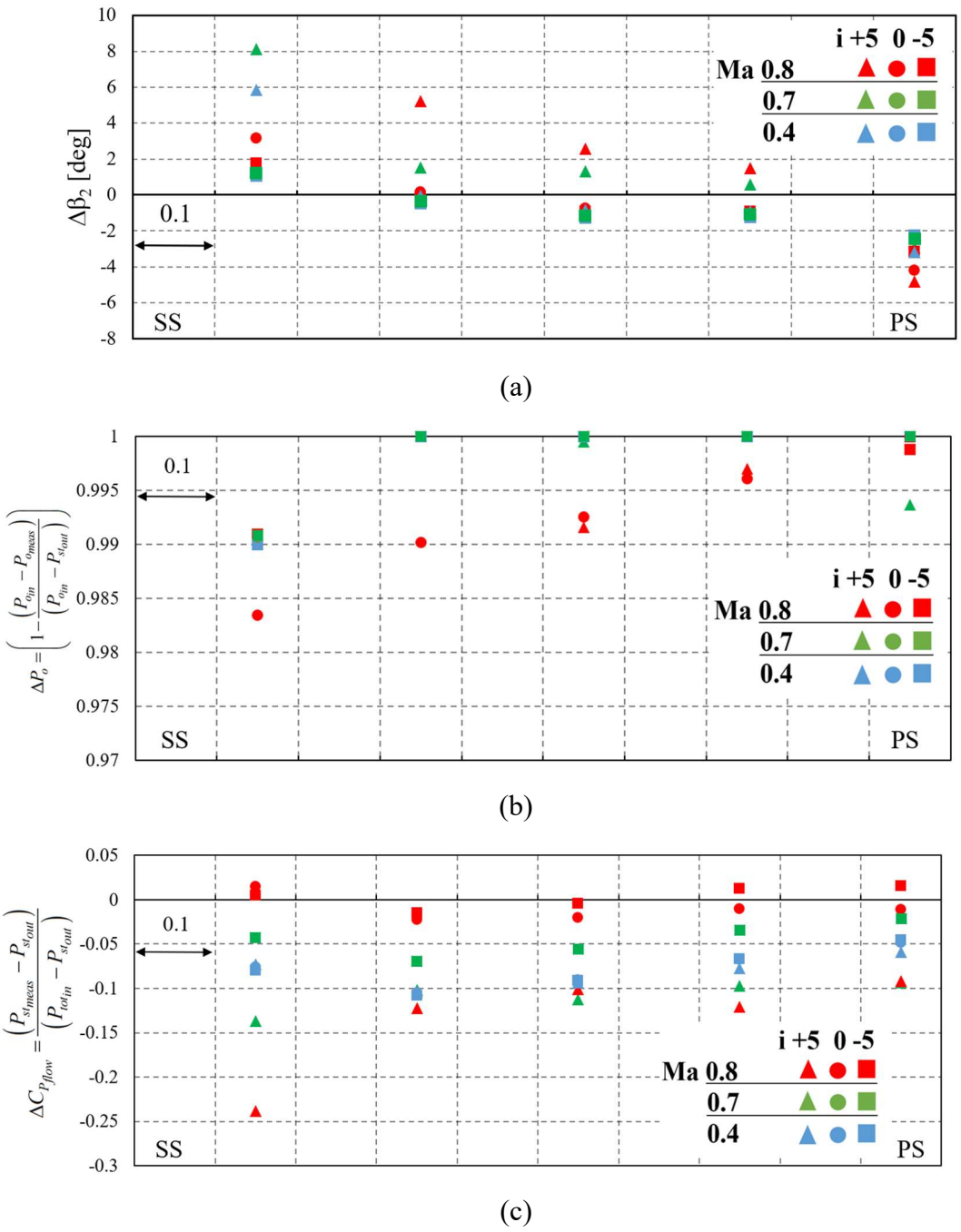

Figure 6.11 Probe measured values along the pitch: the flow angle (a), total pressure (b) compared with the average flow values downstream of the stator and the static pressure (c), compared with the local value of the flow

Static pressure readings are also sensitive to the flow conditions in the passage. The static pressure measurements become unreliable at a high incidence, where the given blade passage

is stalling. However, for the unseparated flow conditions, the measured static pressure results in about a 3–10% larger dynamic head, most of which can be explained by the probe blockage (probe diameter in this case is 5% of the passage width at the outlet). Providing that in a given stator blade row the real value of the blockage can be estimated with the use of a CFD, the measurement uncertainty can be reduced from up to 12% down to below 2%. This is an important improvement, since with the reduced uncertainty the designer can estimate the velocity of the core flow and therefore estimate the blockage in the passage.

6.5 Measurements along the span

In this section, a full-span case is modelled for Stator 1 to estimate the measurement uncertainty in the constrained environment of the multistage compressor. The flow pattern considered in this section is shown in Figure 6.12 and has major corner separations between the casing and suction side, as well as between the hub and the suction side. The probe is moving radially down and in Figure 6.12 is shown measuring at 10% of the span. The stator at this stage is shrouded, so the end wall at the bottom is stationary. The main question is regarding the accuracy of the probe readings along the span if such separations occur. This is especially important for the old designs of the compressor blades, where the three-dimensional effects—in particular the corner separations—were not specifically addressed, so in some cases, the blade rows could work along the compressor operating line with moderate corner separation zones.

For the two-dimensional simulations in the previous section, the probe was considered as a cylinder of infinite length going throughout the computational domain, and the calibration coefficients were obtained from Chapter 4 without the tip flow effects. In this section, for the full-span simulations, the probe calibration coefficients do account for the flow around the probe tip.

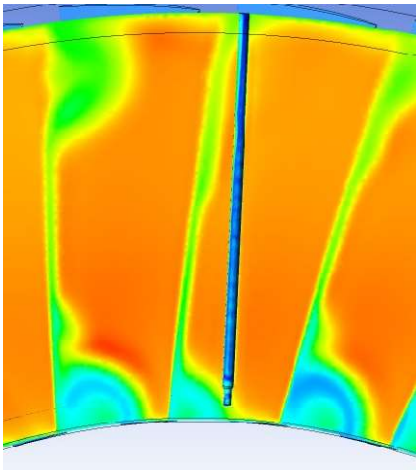

Figure 6.12 A simulation of the probe and the stem downstream of the stator blade row experiencing corner separations

In one of the traversing positions, at 15% of the pitch counting from the suction side, the probe starts near the blade suction side at the casing and reaches the hub at the middle of the passage. On its way it passes the corner separation near the casing, which extends for about 15–20% of the span, then it moves through the core flow, and near the hub it approaches the separation region without entering it. Nevertheless, the probe readings could be affected considerably. The hub separation is more extended in the blade-to-blade and less in the spanwise, compared to the tip corner.

Figure 6.13 shows the measured and corrected values for the traverse along the span with the static pressure corrected according to Section 5.4, and flow angles corrected in a similar way but directly to the pitchwise averaged values without conversion to the local ones. The red line shows the local properties of the undisturbed flow along the probe's traversing path, and the black solid dots show the probe readings at several locations along the span. The black empty dots show the corrected values of the reading, and the black line is for the pitchwise average flow parameter from the CFD.

Figure 6.13 (a) shows the flow angle measurements. For simplicity, only three points are shown at 80% of the span and above to show the general trend. At 80% of the span the angular reading shows more than a 10° offset from the flow value, which is not realistic. The reason for such deviated readings was shown earlier in Figure 6.8, where at least one of the three pressure tappings reached the separated region and the data processing algorithm resulted in a

large error. This can be further supported by Figure 6.13 (b) in which the total pressure measurements are shown. At 80% of the span, the measured total pressure is lower by 40% of the reference dynamic head at midspan than both the undisturbed and averaged values at this location. This means that at least one side hole and the middle one are placed in the region of separated flow.

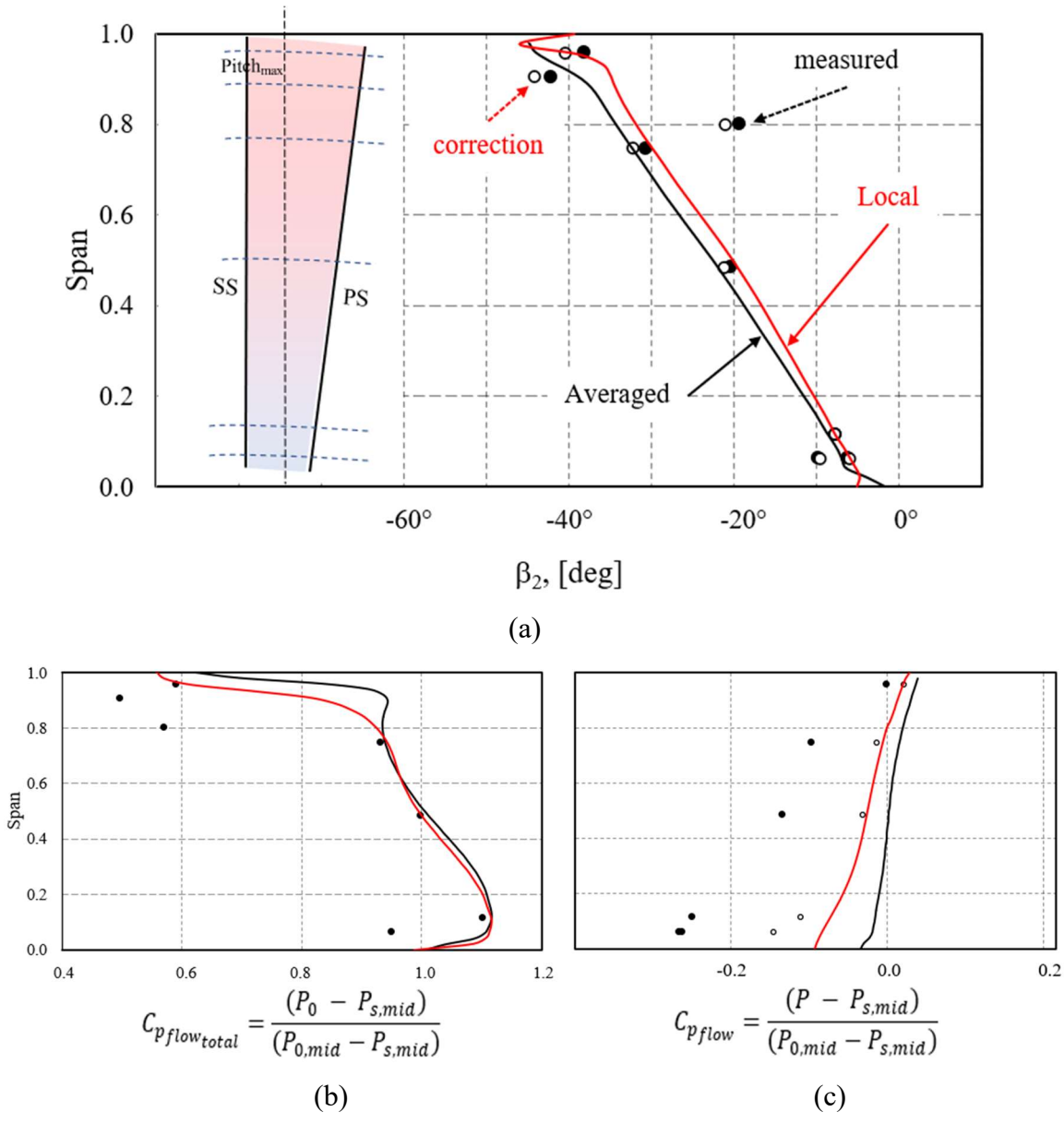

Figure 6.13 Probe measurements along the span: stator exit flow angle (a), total pressure (b) and static pressure (c)

Interestingly, when the probe is placed closer to the casing—at 90% of the span—the angle measurements are within 3–5° of the average, and at 95% it is essentially equal to the local flow value. Without a further understanding of the reasons behind such a good agreement, the researcher could take these results as reliable and proceed with further comparison against the design intent. However, the total pressures in Figure 6.13 (b) are about 30–40% away from the undisturbed flow value. This tells us that the probe is likely to be within the separated region and that the close-to-expected measured angles are a sequence of three fault readings.

Below 80% of the span, both flow angle and total pressure follow the general trend, and the values are close to the pitchwise average with not much circumferential non-uniformity in the middle of the passage, where the traverse is placed. For the locations below 10% of the span, both readings deviate by more than 5° and 10% of the dynamic head in both total and static pressures. This is due to the interaction of the probe and the hub corner separation as shown in Figure 6.12. These findings agree with Lopes et.al. (2022) that the presence of the probe modifies the pitchwise distribution of aerodynamic quantities at the endwall locations.

Figure 6.13 (c) shows the static pressure distributions along the span. The empty dots here show the measurements corrected to the local measured values. The second step – correction from local values (the red line) to the averaged ones (black line) – can be done using full multistage simulation. With the applied corrections the measured values are shifted towards the local values of the flow. Above 20% of the span, the agreement with local values is within ±2% of the reference dynamic head. Near the hub, the flow redistribution due to the probe immersion causes an additional increase in the flow speed, therefore indicating that the assumption of two-dimensional probe blockage is not valid near the hub wall.

6.6 Applications to industrial testing

The mechanisms affecting the probe measurements downstream of stators were studied in previous sections and the limitations for such measurements were set. The probe placed downstream of the stator blade row can provide reliable measurements of the local flow under certain conditions. Apart from the wake region, the core flow is rather uniform in a pitchwise direction, and the probe measurements follow the trend of the core flow within 1° for the flow

angle, and 0.5% of the dynamic head for the total pressure. The static pressure would be measured to include up to 10% of errors, most of which can be explained by the probe and stem blockage, seen earlier in Chapter 4. However, in proximity to the walls, or when the probe is interacting with the separation zone on the blade suction side, the measurements can significantly differ, especially when one of the probe holes is placed in the separated region.

When the corrections were applied to the full span setup, the difference with the undisturbed flow values were found to be well within 1° for the flow angle and well within 2% for the static pressure.

As a result of this Chapter, Figure 6.14 shows the region where the spanwise traversing could be used to measure the real flow downstream of stators. Figure 6.14 (a) shows the simulation of the probe immersed downstream of Stator 1 at near-stall conditions with distinctive corner separations at both end walls. Figure 6.14 (b) is a schematic representation of the low-uncertainty region.

Near the end walls this area is limited by the presence of corner separations. Even if the probe is not placed in the separated region itself, but next to it, the amount of blockage it introduces causes significant distortion of the separated region. This causes large uncertainties of the measurements, the correction of which is more design- and operating-point- dependent than the freestream correction. Near the blade walls, the range is limited by the possibility of linear correction towards the representative average values. When approaching the suction side, the interaction with blade wake and separated flow on the blade suction side can lead to a non-linear correction. Simulations show that starting at 15% of the pitch the measurements can be corrected and starting from 35% the values of the flow angle can be treated as circumferentially averaged within ±1° uncertainty.

Total pressures after 35% of the pitch are measured within 0.5% away from the stator inlet value at a given radius, which does not include pressure losses in the stator. The value of the total pressure therefore can be used as a signal of whether the other two flow metrics—the flow angle and static pressure—can be considered at all. When approaching the pressure side, the interaction between the probe and the blade wake becomes critical after 75–80% of the pitch, when the core flow is pushed towards the low-pressure region of the wake.

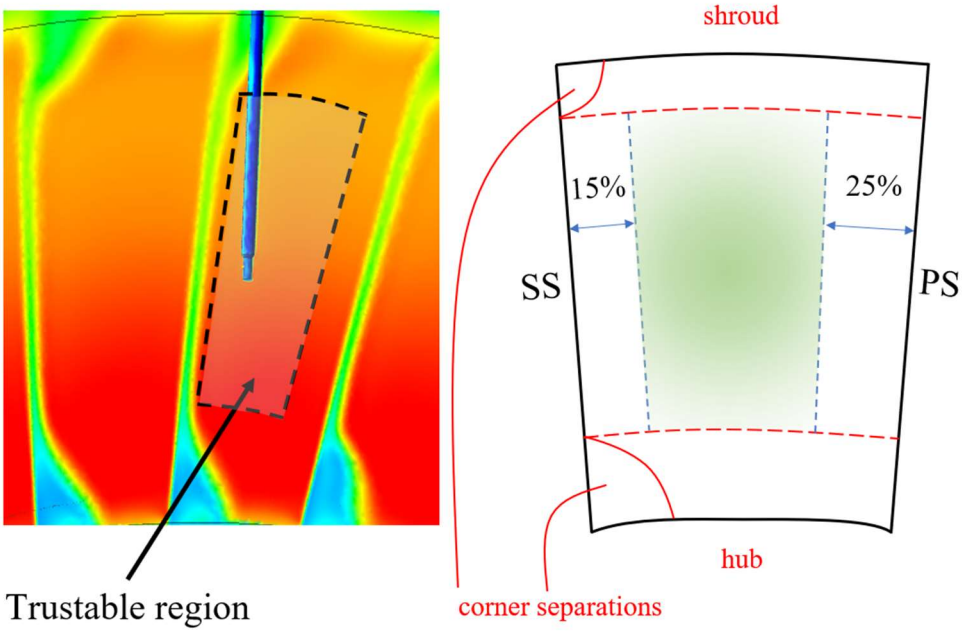

Figure 6.14 Schematic representation of the low-uncertainty region for spanwise traversing downstream of stators with the flow structures (a) and reference dimensions (b)

Another important question of this chapter is how the experimental engineer can identify the high-uncertainty region. When the probe is approaching the separation region on the suction side of the blade, normally the pressure in the side tapping facing the separation will drift from what would be in the clean flow. This will result in unrealistic values of the measured flow angle; the difference between this and the design value could exceed tens of degrees. At the same time, the measured total pressure can still be within a few percent away from the one in the undisturbed flow since the middle tapping can still be unaffected by the blade separation zone. In this case, the measured flow angle becomes unrealistic, but the total pressure does not.

The opposite can happen when the probe is fully immersed into the separation region, which in turn can differ from the same region of the undisturbed flow. When the probe is fully placed in such a region, the flow angle can have realistic values within a few degrees away from the design values, because the pressure difference on the side holes, which define the angle, will be small. This is because both tappings can measure static pressure in a separated region. Therefore, the measured flow angle will effectively be equal to the angular orientation of the probe. However, the total pressure in this case would be significantly lower than in the core

flow, as the middle tapping will also be measuring the pressure close to static in the separation region.

Therefore, it is important that during the spanwise traversing downstream of the stators both the flow angle and the total pressure are monitored and also that these parameters are compared with multistage CFD simulations to assess the adequacy of the experimentally measured values.

Using fine spatial resolution for traversing will help find the boundary of an uncertain region accurately. This enables the maximum sized certain region to be used.

6.7 Concluding remarks

In this chapter the mechanisms affecting the probe measurements downstream of the blade passage were explored. The key difference with measurements upstream of stators is the presence of large vortical structures such as blade wakes and separation zones. When the probe is in proximity to such zones, it significantly changes the flow field in the passage and the measurements can no longer be trusted.

Based on the identified limitations, the low-uncertainty region was described for the measurements downstream of the stator. Within this region the uncertainties associated with the probe immersion were reduced to ±1° for the flow angle, as well as ±0.5% and ±2% of the reference dynamic head for total and static pressure correspondingly. It was also shown how the processing of all three measured parameters together can allow the experimental engineer to identify the high-uncertainty region during the measurement process on site.

Chapter 7 Processing of the real measurements

During spanwise traversing of a multistage industrial compressor, when the raw probe readings are being processed with the freestream calibration coefficients only, the results can be misleading to the designer due to the uncertainties caused by the interaction between the probe and blade potential fields. Therefore, it is important to establish the procedures to correct these measurements and to evaluate the measured data, so that the latter can be reliably used for compressor assessment.

This chapter addresses two questions: how the measurement corrections can be applied to the real experimental results taken from the multistage axial compressor in the most reliable way, and how this data can be cross-checked for consistency during the experimental campaign. A set of real experimental data sets processed in this chapter is given in Table 7.1. Correction challenges are presented for stator upstream cases only. Stator 8 downstream measurement is only used at the mid-span for analysis of physical consistency of the difference between the measurements and CFD simulation.

Table 7.1 List of test cases in Chapter 7

Blade row	Locations	Flow conditions
S9 upstream	1 radial trajectory Full span	Compressor design OP
S1 upstream	1 radial trajectory Full span	Compressor design OP
S3 upstream	1 radial trajectory Full span	Compressor design OP

The consistency of the measurements is verified against fundamental physical principles, such as conservation of mass, radial equilibrium and added work. For this, the measured values are processed into an integrated mass flow and velocity components. It is shown below that the uncorrected measurements show a significant variation in calculated mass flow along the measurement sections in a range of ±15%. When the measurements are corrected based on the

flow conditions and probe location for every section, the variability of the results falls to within ±4% of the inlet value.

7.1 Measurement correction procedure

For a compressor designer, the most convenient representation of a compressor's detailed performance is the pitchwise-averaged flow parameter distributions along the span. Such distributions can be compared against the mean line design values and one- or two-dimensional design code results. Same spanwise distributions are common in multistage CFD practice, and therefore this is a convenient way to compare the measurements with other parameters in the design system.

Therefore, this section aims to address two questions: how the real measured results can be translated to the local values of the undisturbed flow at the location of the probe head, and then how these corrected values can be translated to pitchwise averaged ones.

7.1.1 Probe location inside the compressor

As shown in Section 3.1, the traverse can only move in the radial direction, so it is not possible to adjust the pitchwise position between the blades to account for the blade twist and three-dimensional design when the probe moves along the span.

Figure 7.1 shows the two cases that are considered here. The simple case in Figure 7.1 (a) is for the typical rear stage of the industrial compressor with no adjustments for the three-dimensional flow. It has a uniform blade profile along the span, and a hub-to-tip ratio of 0.8, so that when the probe is immersed, it stays at the same pitchwise position with an almost-uniform probe-to-pitch ratio. Therefore, a single correction is required for the flow angle, based on the relative pitch location of the probe. In addition, a typical Mach number for such a stage would be subcritical for the cylindrical probe, and the pressure corrections can include only two variables: the location and the flow inlet angle.

Figure 7.1 (b) shows the probe trajectory upstream of the first stator, taken from the real experimental setup. This case is further complicated along the span by the probe varying

pitchwise location, variable probe-to-pitch ratio, and a supercritical flow Mach number at the bottom half of the passage.

These locations have already been explored in Chapter 5; the actual measured values from the compressor will now be processed as an example of the correction procedure. The probe enters the flow path near the casing at 45% of the pitch (counting from the suction side), and it reaches the hub at around 25% of the pitch. The stator blades have a two-dimensional twist without any lean or sweep, so the probe location for measurement corrections can be linearly interpolated between the casing and the hub.

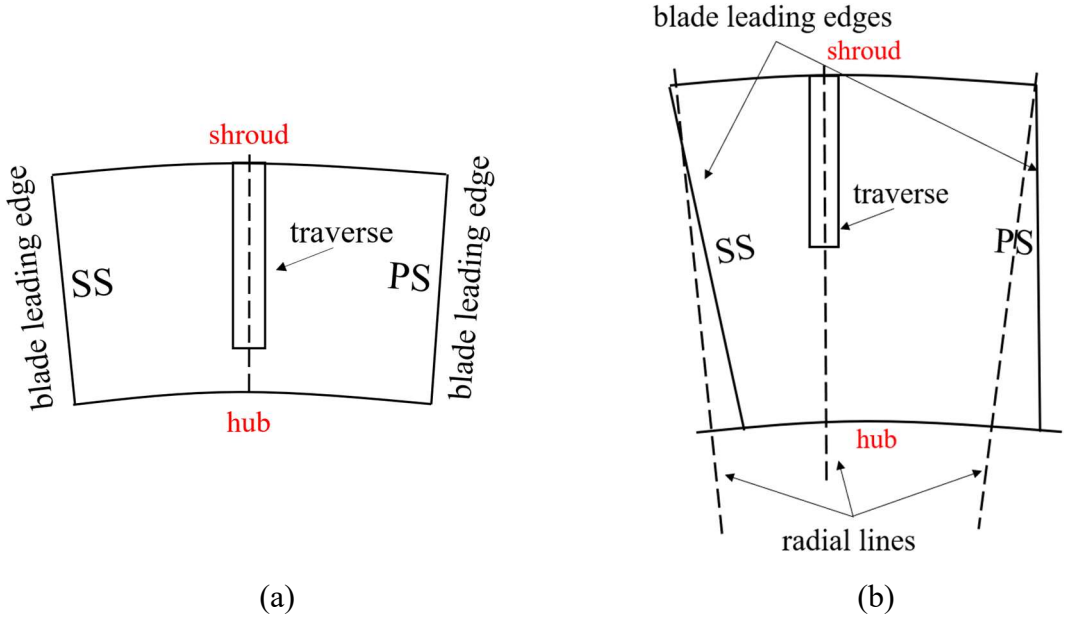

Figure 7.1 A typical traversing location upstream of the stator blade row for the middle and rear stages (a) and the frontal stages (b)

The basic correction procedure will be given for the simple case in Figure 7.1 (a) with further adjustments provided for Figure 7.1 (b). For both cases, full three-dimensional CFD simulations of the probe and the stem at the real locations upstream of stators were performed.

The two-step measurement correction procedure was described in Chapter 5. The first step accounts for the interaction of the probe and the blade flow fields. The second step accounts for the potential flow field of the blade channel to obtain representative pitchwise averaged values of the flow. The correction from local to pitchwise averaged values was done with the use of multistage CFD simulation at the operating point of interest.

7.1.2 Correcting the flow angle measurements

Figure 7.2 (a) shows the photo of the traversing hole, from which the experimental data will be presented. Figure 7.2 (b) is a reminder of the flow angle correction line from Chapter 5 which shows that the angle measurements can be universally corrected in the whole range of studied conditions and that the correction based only on the probe's pitchwise location can reduce uncertainty down to ±1° from the local value of the undisturbed flow. For this case, the pitchwise location of the probe is uniform along the span and equals 54% of the pitch counting from the suction side of the blade, so the expected correction should be +1.5° from the value of the undisturbed flow field.

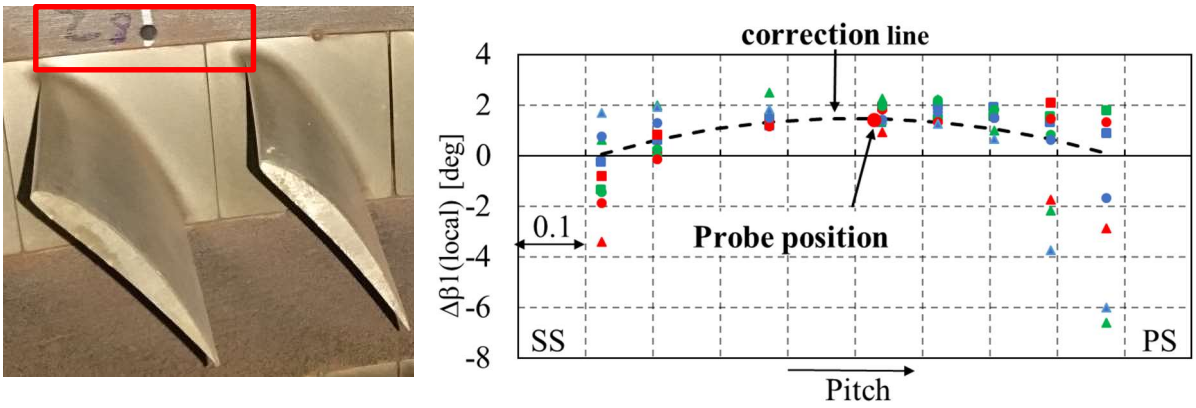

(a) (b)

Figure 7.2 Location of the traversing hole upstream of Stator 9 (a) and a correction value for the measured flow angle based on the pitchwise location of the probe

Figure 7.3 (a) shows the spanwise distribution of the measured flow angles in terms of the blade incidence along the span:

$$i = \beta_{Iblade} - \beta_{IMFA} \qquad (7.1)$$

where both values are taken for a given span position.

Solid black circles stand for the raw measured values, which means the value is calculated by processing the three pressure readings of the probe holes with the freestream calibration coefficients. The measurements indicate an extra incidence of 1.4° uniformly along the span

compared to the CFD simulation. Now the correction procedure can be applied to these values based on the experience gained in Chapter 5.

Figure 7.3 (b) shows the local flow angles in the potential field of the undisturbed flow in a solid line and the readings of the simulated probe when placed at a given pitchwise position. This line is extrapolated from Figure 5.6 for the blade row incidence of -2.5°, since this blade row was originally taken as a model for sensitivity study in Chapters 5 and 6. The blade is radially uniform, so the probe's pitchwise location is constant along the span, and the stator incidence varies along the span within ±1°. Therefore, a single-value correction can be applied uniformly for all the data points along the span.

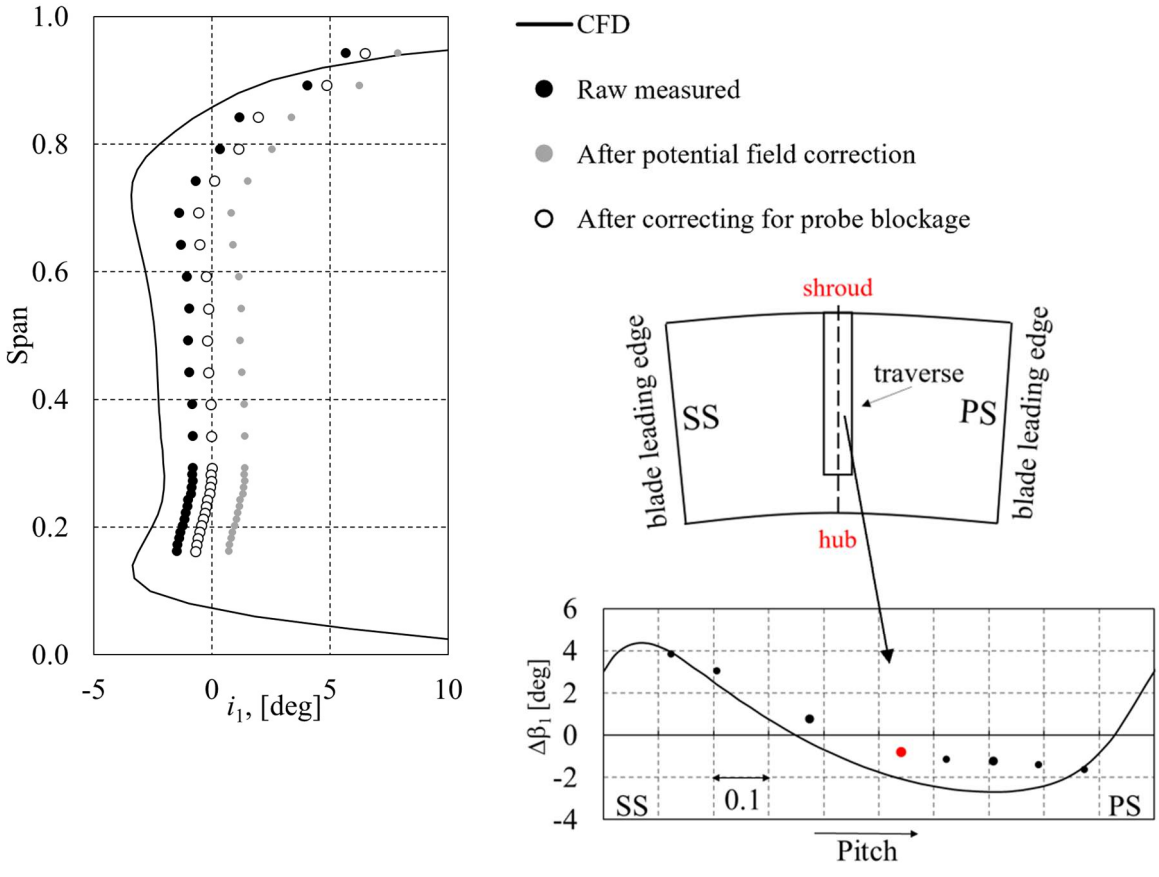

(a) (b)

Figure 7.3 Spanwise flow angle distribution with corrections (a) and the results of potential flow field simulation together with simulated probe measurements (b)

In Figure 7.3 (b) for the position of 54% of the pitch, the flow angle of the undisturbed flow would be -2.2° from the pitchwise averaged value. Therefore, if an experimental engineer were to treat the real probe measurements from Figure 7.3 (a) as the local ones, he would have to shift the solid circles in Figure 7.3 (a) by almost 2° to the right (see the grey circles). This would mean 3.6° of extra incidence to the stators which, as will be shown later, would raise questions regarding the consistency of such measurements. However, when the reading is corrected to the presence of the probe (Figure 7.2 (b) the resulting value is shifted by 0.8° towards the positive incidence. After corrections, the experiment shows a 2.2° positive incidence compared to the multistage compressor simulation, which is further away from the multistage CFD. The viability of such a difference will be examined in the next section.

7.1.3 Correcting the pressure measurements

Figure 7.4 shows the raw measurements of the total and static pressures along the span upstream of Stator 9 compared to a multistage CFD simulation. In Figure 7.4 (b), between 20% and 70% of the span—the agreement for the two data sets of the total pressure—is well within the uncertainty of the measurements. The difference becomes significant in the top 30% of the span, which indicates a significant difference in the tip flow. This can be caused by the geometrical uncertainty (different radial gaps) or the modelling errors in the tip vortex flows.

In Figure 7.4 (a) the broken line shows the undisturbed local value of the flow; black solid circles show the raw measurements, and black triangles show the simulated probe measurements a from full-span CFD setup.

The gradient of the broken line is similar to that of the measurements and, the offset between the two sets is explained by the potential flow field distribution upstream of the blade row. However, CFD-measured values shown in triangles show a slightly different slope and at 20% of the span the difference increase up to 10%. This difference in the gradient is then translated into the representative pitchwise average values, shown in Figure 7.6.

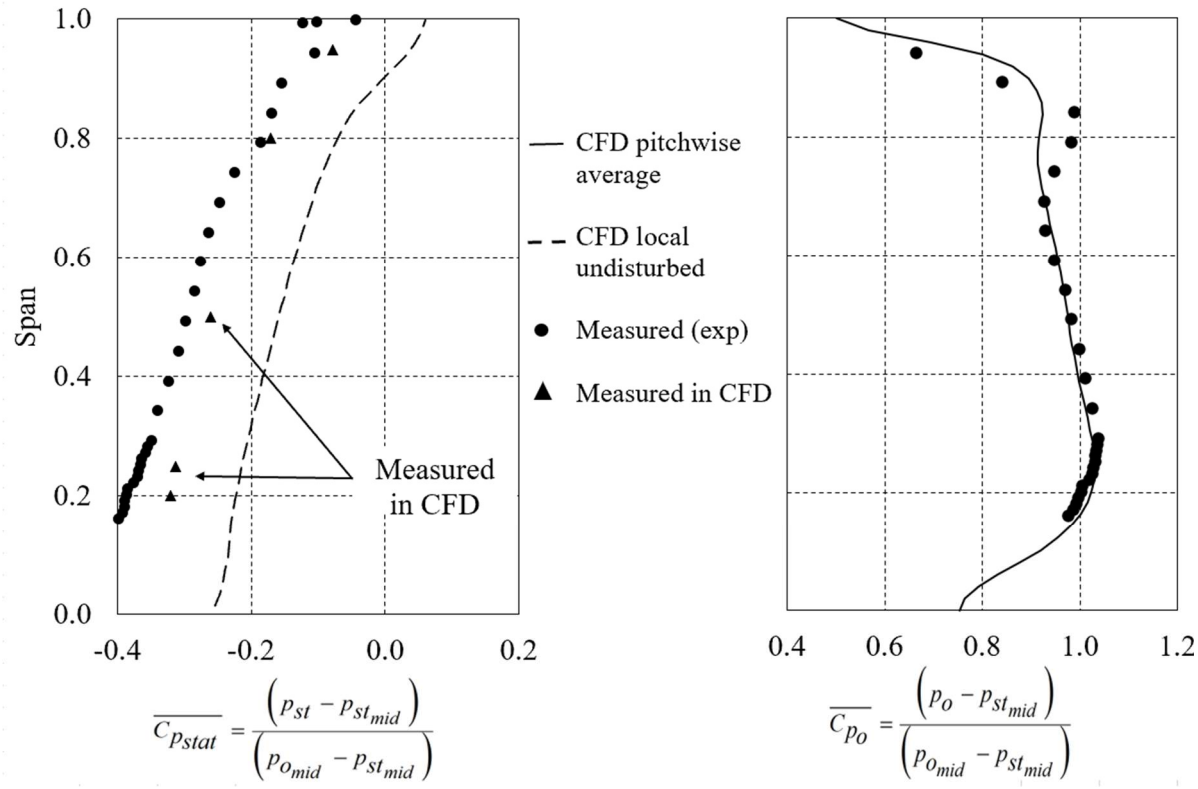

(a) (b)

Figure 7.4 Total (b) and static (a) pressure measurements (raw) compared to the simulation results downstream of Rotor 9

Similar to Figure 7.3 (b), Figure 7.5 shows circumferential static pressure distribution at the location of the probe, where the dynamic head is over 25% larger than the pitchwise averaged and about 7% larger than the undisturbed local value. Since the circumferential position of the probe is uniform along the span, the broken line and solid points distribution should be parallel to each other in Figure 7.4 (a), and the gradients of both lines represent the static pressure gradient downstream of the rotor that follows the radial equilibrium condition.

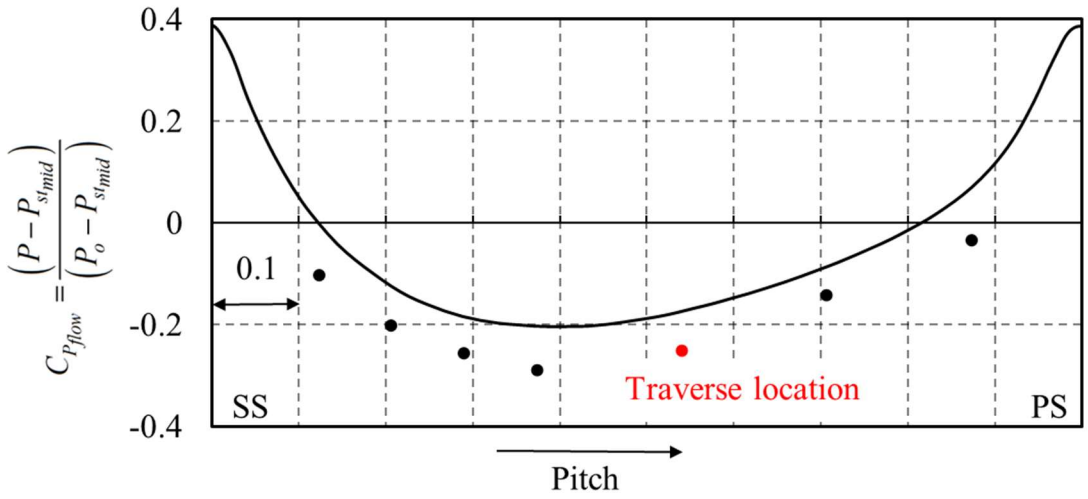

Figure 7.5 Static pressure distribution along the pitch and the simulated probe measurements

In Figure 7.6 only the static pressures are shown with the solid circles to represent the raw measured data, processed with freestream calibration coefficients, and the solid triangles show the simulated probe measurements at the boundary conditions taken from multistage simulation.

It can be seen that the gradient in CFD-measured pressures agrees with the pitchwise averaged profile, and the offset between the two is constant along the span. However, the measured values show differing gradients; when corrected, they do agree with the multistage CFD results at around 80% of the span, but then the measured pressures have a higher gradient towards the hub.

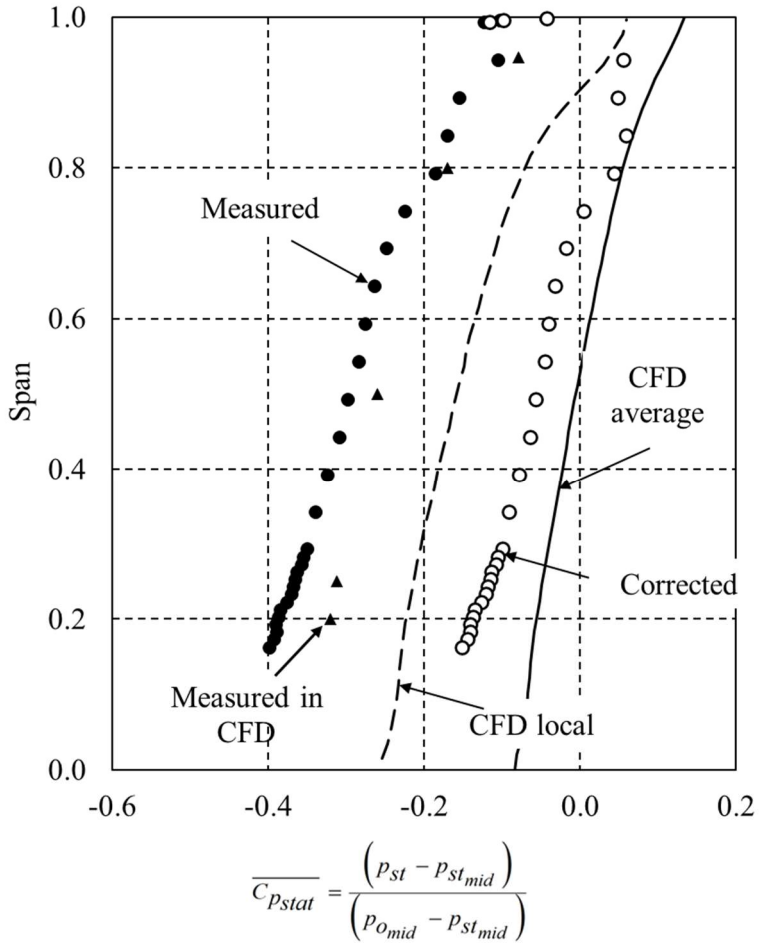

Figure 7.6 Static pressure measurements before and after corrections

7.1.4 Correcting the pressure measurements for frontal stages

At the traversing location shown in Figure 7.1 (b), typical for the frontal stages, the flow behaviour is more complicated. For the hub-to-tip ratio of 0.5 the geometrical blockage near the hub is twice as much as near the casing, and due to the blade twist the pitchwise location of the probe can shift by more than 10% of the pitch. On top of that, in the hub section downstream of Rotor 1 the flow reaches a supercritical Mach number of 0.7.

In Figure 7.7 the procedure from Section 5.4 is applied to the real measurements in two compressor stages of the same architecture: Stages 1 and 3. The flow speed is below critical in Stage 3 (Figure 7.7 (a)) and supercritical at the hub of Stage 1 (Figure 7.7 (b)). In Figure 7.7

(a) measured pressures agree with the undisturbed values, and after correction they show a good agreement with the distribution of pitchwise averaged pressures.

In Figure 7.7 (b) the measurements show negative pressure gradient along the span. This is due to the difference in the probe blockage effect for sub-critical and critical flows; the measured Mach number is over 10% higher at a 90% span, and only 7% higher at the mid-span, so the pressure gradient along the span is not the same for the simulation and the measurements. This is because near the critical Mach number the correction to the measured pressure from Equation 5.4 that accounts for the Mach number is larger than for the subcritical flow. And for given conditions, the measurements become closer to the averaged values when the Mach number increases. The pressure gradient for the corrected values is positive and correlates with the trend of the multistage CFD.

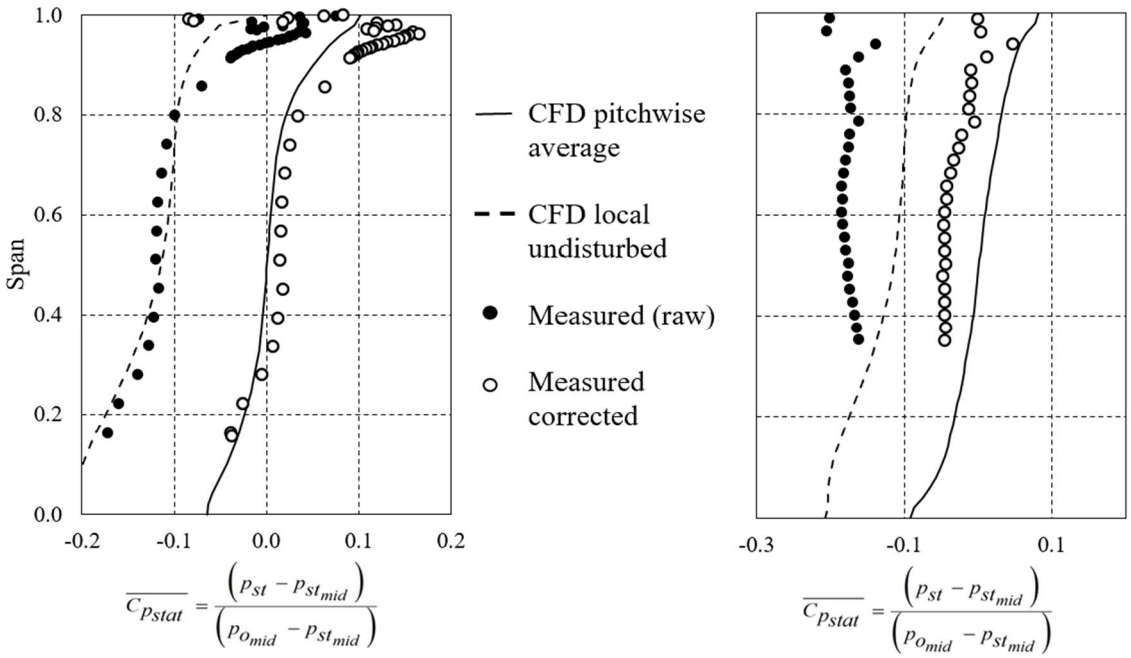

(a) (b)

Figure 7.7 Static pressure measurements along the span for the subcritical Stator 3 (a) and supercritical Stator 1 (b)

As mentioned in Chapter 3, in the compressor of interest, the frontal stages have a designed swirl distribution close to the constant reaction along the span. This results in relatively uniform

pressure distribution downstream of the rotor, achieved by a certain distribution of the flow angle and velocity. Such distribution can be seen, for example, in Figure 7.7 (a), where for the mid-span sections the pressure profile is almost uniform. The same design approach was used for the first stage in Figure 7.7 (b), although both measurements and CFD results show a non-zero gradient throughout the span.

7.2 Consistency of the measurements

Independent validation of the experimental results is one of the most important steps in the data processing routine. Before validation, the measured values need to be processed to obtain lower-order compressor parameters, such as velocity components, mass flow, work input and spanwise gradients of the parameters. This data can then be examined for consistency; for example, the mass flow conservation along the compressor should have the same value, but in addition this data can be compared with other independent sources of information, such as overall gas turbine performance or pressure measurements on the casing. When the measurement corrections are applied, the corrected data should follow the consistency considerations better than without such corrections.

Figure 7.8 shows the process diagram for the experimental data processing, which is discussed below in this section. First, the two measured pressures can be converted to the flow Mach number, and together with the flow temperature, it results in the absolute flow velocity. Combined with the flow angle and known rotor linear velocity U, the velocity diagram can be built. The velocity can also be split into the circumferential and axial components. The density is a result of measured pressure and temperature.

The axial velocity combined with the density and the frontal area of the blade passage provides the integrated mass flow at each measurement location.

The circumferential velocity and the static pressure gradient are the greatest contributors to the radial equilibrium between the blade rows. For the middle and rear stages this condition can be one of the ways to examine consistency. The difference in circumferential components of the absolute velocity upstream and downstream of the rotor together with the rotor linear velocity results in the stage work input, or Euler work. This can be compared with the total pressure rise in the rotor.

If the difference in flow angle and circumferential velocity is observed between the two data sources—experimental and computational—the difference in static pressure gradient should be seen as a sequence of the radial equilibrium equation. This is discussed in the second part of the section. Near the wall, a local change in the radial pressure gradient can be caused by significant radial velocities due to the endwall blockage. However, in the core flow the radial component is within 1% of the axial velocity, and in the current method the radial velocity is omitted from consideration. In the end, the differences in flow angles should mean differing Euler work and stage loadings, and this can be verified against the pressure distributions along the compressor.

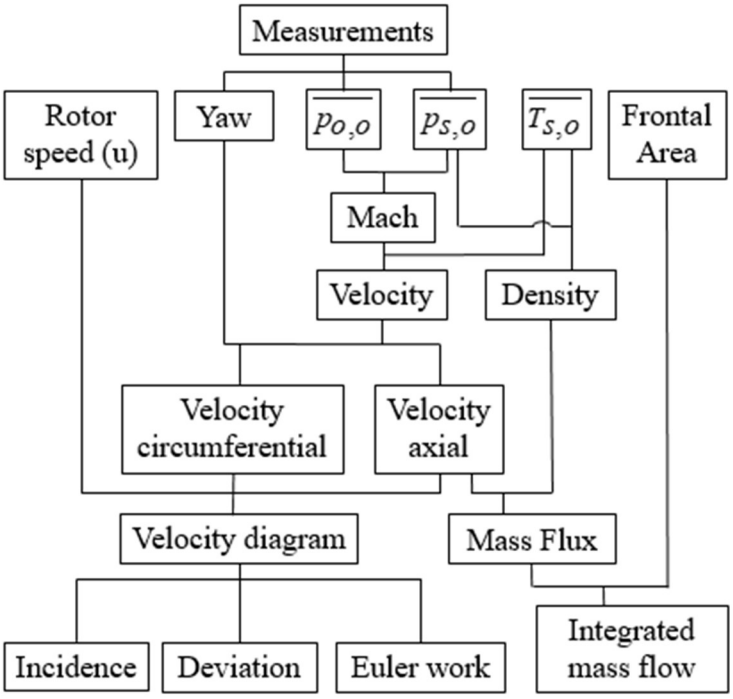

Figure 7.8 Data processing diagram for the measurement results

Sometimes, a comparison with multistage CFD results was found to be convenient early in the process, as it allowed the measured and modelled parameters to be visually overlapped in one graph and the difference to be quickly observed. If the difference was found to be too large, the raw experimental data was examined, and some of the traversing results had to be scrapped. However, in most of the cases, even significant deviations in the experimental results were first corrected for the presence of the probe, and then the remaining differences were found to be

consistent with each other. Later in this section the multistage CFD results will be shown for reference.

7.2.1 Mass flow conservation

The integral mass flow, calculated according to Figure 7.8, can now be discussed. In current calculations the temperature was taken from CFD for the reasons explained later in this section. When the density and the axial velocity are known, the mass flux can be calculated along the span which, for the known swept area, can be integrated into the total mass flow. The mass flow conservation along the measurement sections can then be examined to estimate the adequacy of the measurement results.

Figure 7.9 shows the axial Mach number distribution upstream of Stator 9 for the CFD simulations and the measurements. The axial component of the Mach number is already processed with the input of the flow angle and total and static pressures, and only the temperature value is required for it to be processed into the axial velocity. Therefore, the spanwise distribution of the axial Mach number can reflect all the changes to the integrated mass flow introduced by the measurement corrections and at the same time, it is still a non-dimensional metric, which can make sense to the reader.

The difference in the axial Mach number between raw measurements and the CFD pitchwise average for the range of 20–80% of the span is within 5–12%. When processed into the mass flow, it causes an 8.5% higher mass flow than that measured at the compressor inlet.

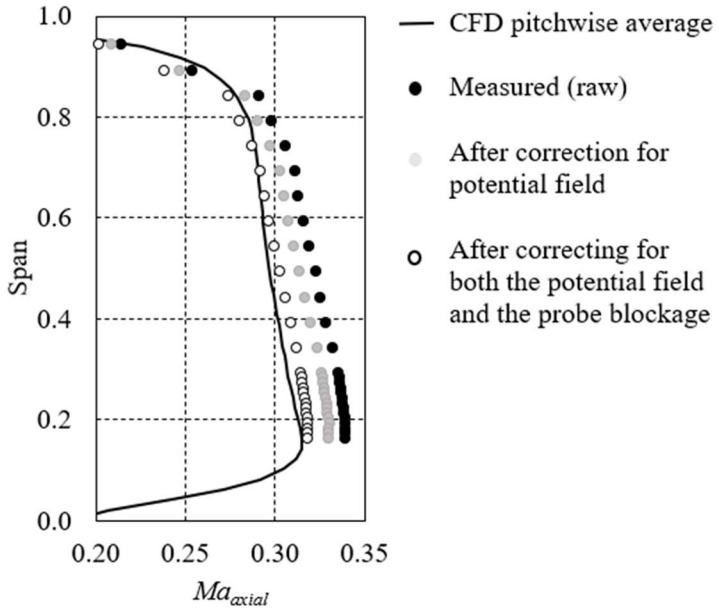

Figure 7.9 Axial Mach number distribution upstream of Stator 9

When the corrections to the potential field were applied, the resulting profile laid significantly closer to the CFD profile, and the integrated mass flow was reduced to 3.1% above the inlet one. When the corrections for the probe presence were introduced, the resulting profile overlapped with the computational one, although with some differences in shape. As a result, the mass flow became 0.8% less than at the inlet. As shown later in this section, the measurement uncertainties and the calculation method cannot provide a total mass flow uncertainty better than ±4%. But the improvement is still observable.

A fuller picture of the effect of measurement corrections can be seen in Figure 7.10 for Stage 1. Here, the region below 30% was not measured to the setup problems of the initial traversing gear, and the extrapolation of the measured profile down to the hub will be discussed separately later in this section. The first two plots, (a) and (b), in Figure 7.10 show the corrected flow angle and static pressure, which were shown earlier in Figure 7.3 and Figure 7.7. The second row of that figure—(c), (d) and (e)—shows the Mach number and its axial and circumferential components so that the reader can follow how the applied corrections affected each of the components of the velocity diagrams.

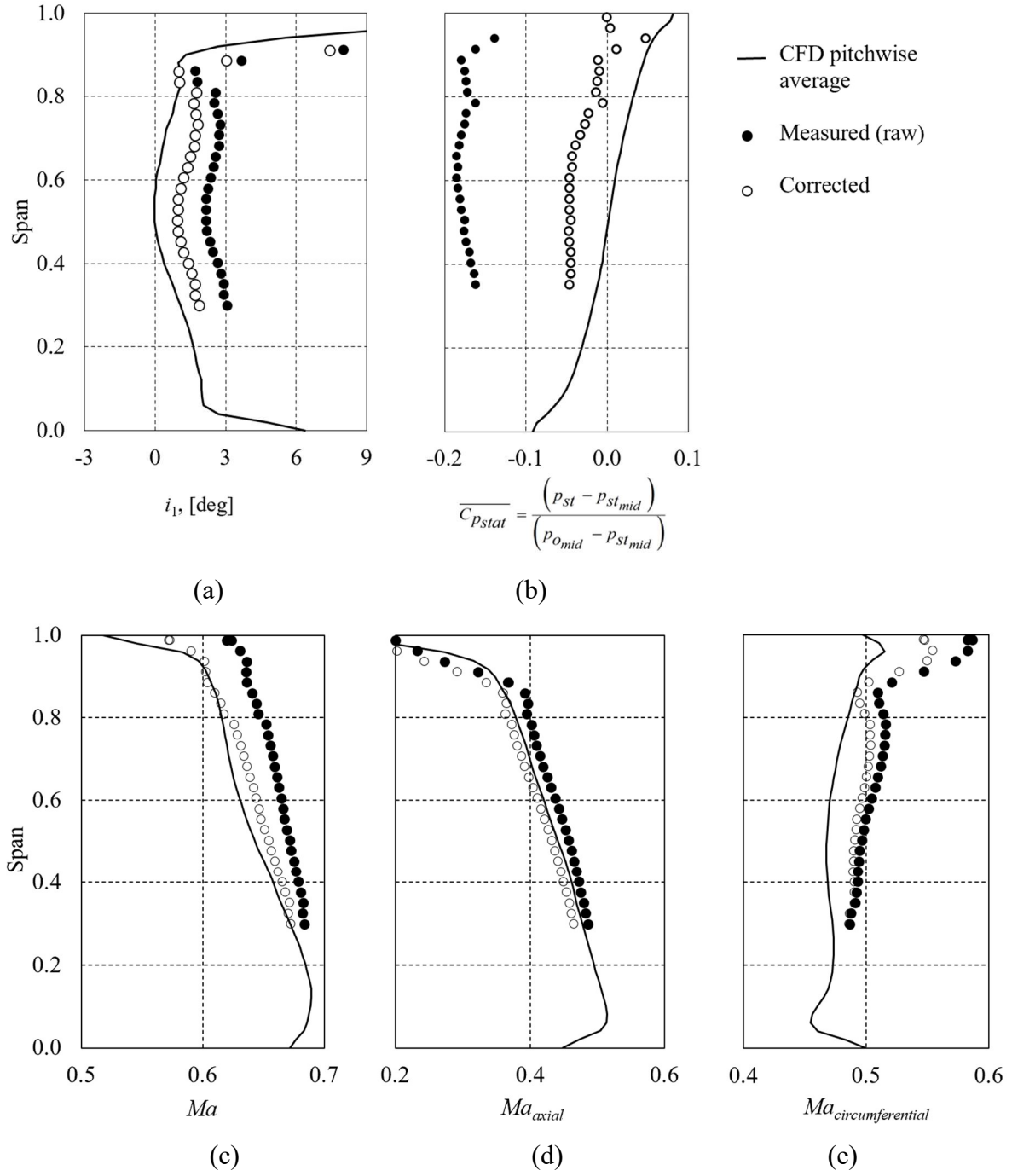

Figure 7.10 Measured and CFD distributions along the span downstream of Rotor 1: flow angle (a), pressure (b), Mach number (c), axial (d) and circumferential (e) components of the Mach number

When the pressure profile was corrected, as shown in Figure 7.10 (b) both the pressure and Mach number gradients along the span fell in line with the CFD results, although with some

offset. The improvement in mass flow, which is mainly the consequence of the axial Mach number distribution, is from over +15% without correction down to +2.7% after the correction.

Figure 7.10 (e) shows the circumferential component of the Mach number, which reflects the flow swirl, and therefore the work added in the stage. Without the correction the expected Euler work—which will be calculated in the next section—would be more than 12% larger than that of a CFD, and after correction it reduced to 3.5%. The remaining difference will be compared to the total pressure rise in the first stage, which is done later in the section. Similar to the Mach number comparison, the biggest difference and the biggest correction in the circumferential component is obtained near the casing.

For all the measurement sections same correction procedure was applied and the joint results are shown in Figure 7.11. Before the corrections, the spread of the values exceeded ±15% from the inlet value, which leaves significant concerns regarding the accuracy of the measured data in general. After the corrections the values still fall within ±4% of the inlet value, which is still excessive for laboratory standards. However, for industrial testing, this can be explained by the sensitivity to the measured flow angle, pressure and required extrapolation of the spanwise profile in proximity to the end walls.

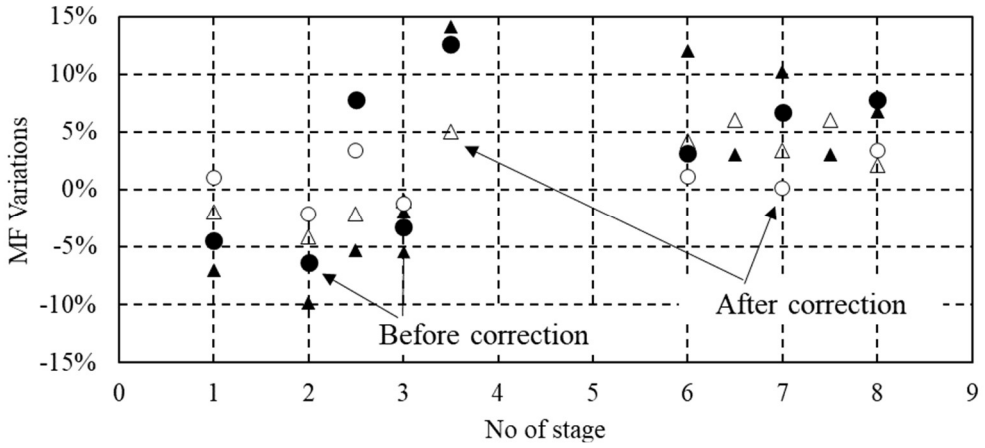

Figure 7.11 Integrated mass flow measurements along the compressor before and after corrections

For on-site experimental work at a real gas turbine engine, the precision of such mass flow calculations can be rather low due to many uncertainties in the process. The purpose of this

section, therefore, was to show that the main uncertainties are caused by the flow angle and the pressure measurements, so that when the measurement corrections are applied, they bring a sensible change to the overall result, and the measured mass flow value moves towards the values defined by the conservation laws. In the next section, the uncertainties in such mass flow calculations will be discussed.

7.2.2 Sensitivity to the uncertainties in mass flow calculations

In this research, the mass flow calculations between the blade rows are used only for qualitative purposes, i.e. to show whether the corrected data brings any improvement towards the mass flow conservation. In this section, the sensitivity of such mass flow calculations is discussed, focusing on measurement uncertainties, uncertainties due to reconstruction of the flow field in the unmeasured regions and due to the use of CFD as a source of the local flow temperature.

Flow angle and pressure measurements

Following the discussion in Chapter 5, the measurement uncertainty caused by the potential field and the presence of the probe can be reduced to ±1° for the flow angle—down to ±5% of the dynamic head—for the pressure. Figure 7.12 shows how the change in the flow angle and the pressure will affect the axial Mach number distributions. Here, the set of computational experiments was carried out, so this is the CFD line which is varied against unchanged measured values. In Figure 7.12 (a) the solid line represents baseline CFD results for the section of interest, and the broken lines are for +1° and -1° of uncertainty. If the angle is wrongly measured by 1° towards the axial flow, the integrated mass flow will be larger by 1.9%. If the error in measurement shows more swirled flow, the mass flow will be lower by a similar amount. In both cases, the uncertainty in the mass flow due to the flow angle is lower than that of the mass flow calculated with the initially measured values.

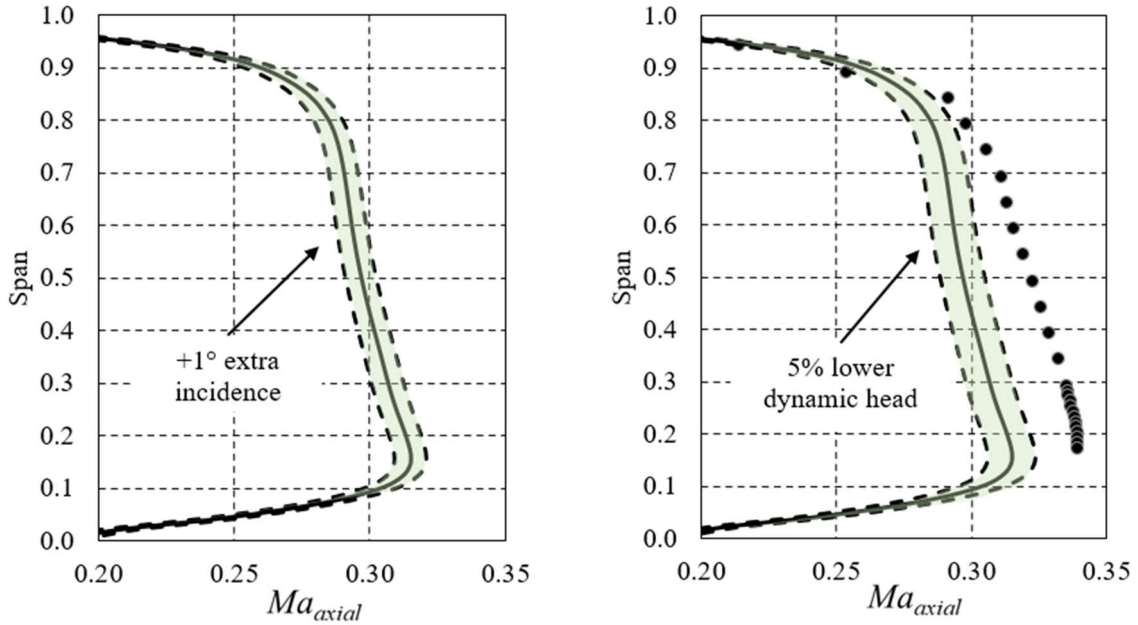

(a) (b)

Figure 7.12 Sensitivity to ±1° uncertainty in the flow angle (a) and ±5% uncertainty in pressure measurement (b)

In Figure 7.12 (b) the sensitivity to the uncertainty in pressure measurements is shown. The pressure affects the mass flow in two ways: calculating the flow Mach number and calculating the air density. As a result, when the pressure measurement is higher by 5% of the dynamic head, it causes a 2.6% reduction in the mass flow. This sensitivity is not uniform along the compressor as it would be a function of the absolute Mach number together with the absolute value of the pressure, but for now, it is sufficient for a basic correlation.

The uncertainties in the angle and pressure measurements can be linearly combined as they independently affect the direction of the absolute velocity vector and its length. As a result, when the measurements are corrected for the presence of the probe in the blade passage, the remaining uncertainty of such corrections can cause an uncertainty of up to 4.5% in the integrated mass flow. Therefore, the spread of ±4% shown in Figure 7.11 can be explained by the uncertainties in these two values only, and further improvement of the measurement techniques will be required if this spread is to be reduced. For the sections downstream of the

stator, the sensitivity to the flow angle is less, since the flow is more axial, and the main factor is the correctness of the pressure measurement.

Temperature

Temperature measurements in real gas turbines are limited due to several uncertainties, such as the heat sink to the traversing gear, radiation to the turbine casing, and temperature redistribution along the casing of the multistage compressor. The initial probe design allowed for temperature measurements; however, due to the setup problems with the traversing gear during the initial testing, the measurements were taken in only a few sections along the compressor, so the data is not sufficient for any suitable consistency checks. This raised the necessity of using the temperature from CFD simulations for the mass flow calculations.

At the same time, the compressor exit temperature was independently measured throughout the experiments, and the agreement with the modelling results stayed within 2% of the total temperature rise. This brings the assumption that even if, for a particular stage, the efficiency and the loading were mis-predicted by a large amount due to the differences in stage matching, the overall distribution along the stages was still balanced in a multistage environment. Therefore, the temperatures from CFD calculations can still be used during the experimental data processing for inter-blade-row measurements, and the uncertainty caused by such use will not be critical.

Assume, for example, that in a particular stage the temperature predicted by CFD is different from reality by 10% of the stage pressure rise. This would mean either a change in the Euler work or stage efficiency by a comparable 10%. For a stage temperature rise in a range of 20–40 K, this would mean a 2–4 K difference. With the temperature in the middle stages around 400 Kelvin, this would mean a 0.5–1% change in calculated air density and 0.25–0.5% in air velocity. The effect of the temperature on the density and velocity is the opposite: The higher temperature causes a higher flow speed for a given Mach number, but at the same time, this means linearly reduced air density. This illustrates that even for the significant miss-prediction of the air temperature by CFD, its effect on the overall uncertainty in the mass flow calculations between the blade rows will be less than 0.25–0.5%, which is significantly lower than the effect of the probe blockage on the flow angle and pressure measurements.

Extrapolation in the unmeasured region

Due to the risk of probe damage, the last 5–10% of the span was not measured for all the sections. In the frontal stages, the immersion was limited by the initial setup, and sometimes the measurements had to stop at 30–40% of the span. For the latter cases, the calculations of the integral mass flow were not carried out, although the measurements were still corrected in the same manner, so that they could be used for other purposes.

Figure 7.13 explains how the spanwise distributions were extrapolated in the unmeasured regions for the integrated mass flow calculations. A solid line represents a CFD-calculated distribution of the axial velocity at a given section and the black circles are the measurements. Line 1 continues the unmeasured part of the measured distribution with the same gradient as the measured line until it reaches the span where the endwall boundary layer is predicted in the CFD. To account for the CFD uncertainties near the endwalls, the two extreme scenarios were calculated: One assumes that the boundary layer at the hub does not exist (line 2), and the other that it starts right below the last measured point (line 3). For line 2, the integrated mass flow is larger by 1.3% than that of line 1, and for line 3 it is lower by 4.5%. Despite evident differences in the three lines shown, the difference in integrated mass flow is modest, due to low contribution of the hub area to the total swept area of the section, especially for low hub-to-tip ratio frontal stages. Therefore, even when measurements are not available in the hub region of the section, extrapolation of the boundary layer profile obtained in CFD can be used for integrated mass flow calculations.

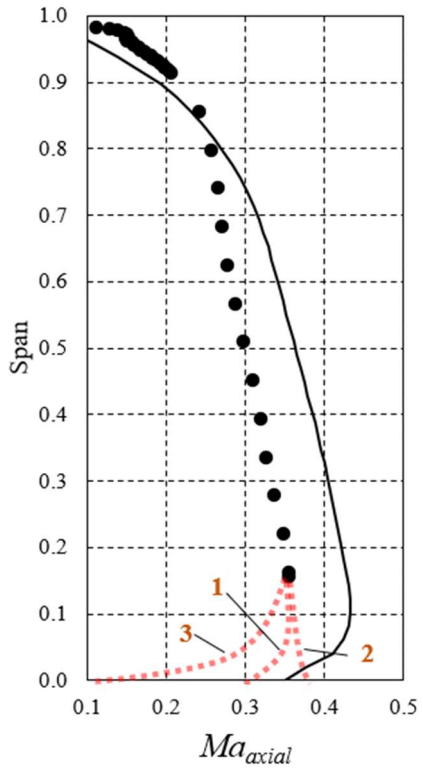

Figure 7.13 Extrapolation of the axial Mach number profile along the span in the unmeasured region for consistency estimation. 1: offset of the CFD profile, 2: linear extrapolation, 3: boundary layer starts at the last measured point.

In Figure 7.14 the spanwise measurements for Stage 9 are taken down to 15% of the span, and the beginning of the endwall flow is visible from the total pressure distributions (Figure 7.14 (a) and agrees with the one predicted by CFD. Therefore, the spanwise distribution can be continued in line with the CFD profile, and the uncertainty of the integrated mass flow can only be caused by the slope of the line. Here, for the unknown region, this uncertainty is well within 1% of the mass flow, estimated by the same approach as in Figure 7.13.

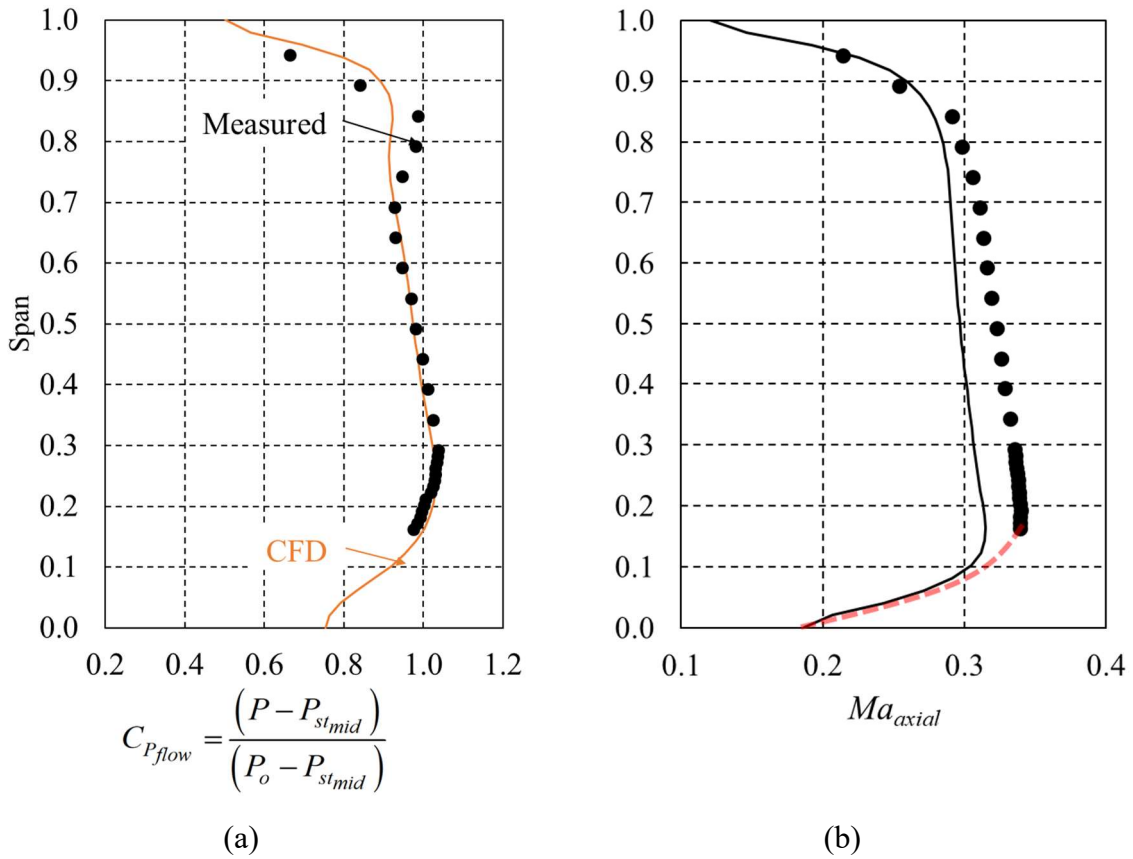

Figure 7.14 Spanwise distributions of the total pressure (a) and the axial Mach number (b) upstream of Stator 9

7.2.3 Radial equilibrium

Downstream of rotors the flow is highly swirled and the centrifugal forces from the flow are counterbalanced by the pressure gradient along the radius. The higher the swirl, the larger the pressure gradient. For the rear stages with a high hub-to-tip ratio and untwisted stators the radial equilibrium condition can be simplified as shown in Equation 7.2.

$$\frac{1}{\rho}\frac{dp}{dr} = \frac{V_\theta^2}{r} \tag{7.2}$$

Where ρ is the air density, $\frac{\mathrm{d}p}{\mathrm{d}r}$ is the radial pressure gradient, V_θ is the circumferential component of the absolute velocity and *r* is the radius of the section. Each side of the equation can be calculated for both the CFD and the experiment. However, due to the high sensitivity to the measurement noise and due to the presence of the radial flow near the end walls, the two components are not exactly overlapping.

For simplicity, Figure 7.15 shows the pressure distribution along the radius downstream of Rotor 9. This was previously shown during the correction procedure in Figure 7.15. Here, another pressure distribution is added for the CFD case when the simulated flow angles agree with the measured ones. When the flow is turned by 2° more in the rotor, the pressure gradient grows to a level similar to that in the experiment.

The pressure gradient for the extra swirled flow is 25% higher, which is visible from the slope of the broken curve in Figure 7.15. Therefore the pressure gradient, especially downstream of rotors, can be a valuable means for consistency checks in the core flow.

For the frontal stages of the compressor of interest, the other important contributors to the radial equilibrium—the meridional velocity and the meridional curvature of the flow [Denton (1978)]—start playing a significant role. This is because in the frontal stages the flow has strong meridional curvature due to the geometry of the blade channels (for example, a steep increase in the hub radius). These factors, together with the expected measurement uncertainties at near-critical Mach number, made it barely possible to use the pressure gradient for consistency check in the frontal stages, and therefore the frontal stages are not discussed here.

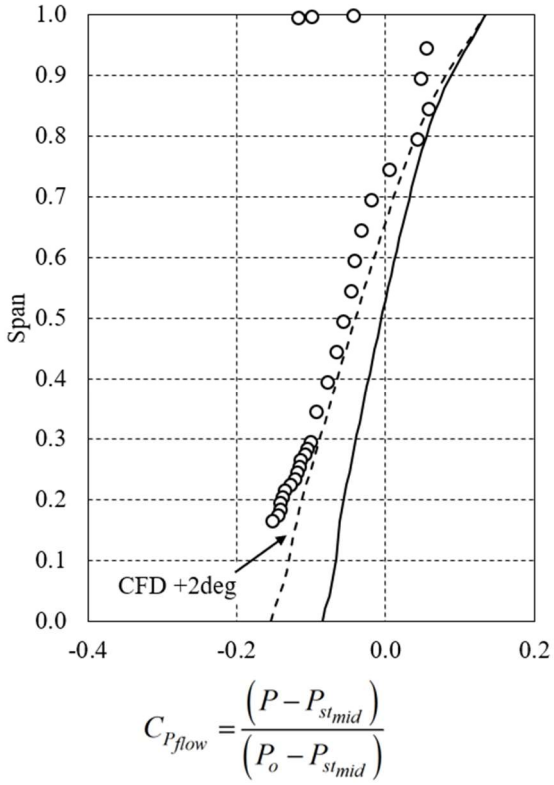

Figure 7.15 Spanwise distribution of the static pressure downstream of Rotor 9

7.2.4 Euler Work

In Chapters 5 and 6 it was found that the total pressure measurements can be reliably used without any corrections for the unseparated regions of the flow. As a result, a distribution of stage loadings in terms of the total pressure rise is the most reliable metric when compared with the design intent or CFD simulations. When the traversing is performed along the span, such distributions can also indicate differences in the endwall flows and redistribution of the flow along the span.

At the same time, the total pressure rise can indicate the added work to the flow, providing the efficiency estimations during the modelling are sufficiently close to reality. Therefore, the total pressure rise can be used as a consistency check for the angle and the pressure profiles. This can be done by building up a schematic representation of the velocity vectors upstream and downstream of each rotor; this, in turbomachinery practice, is known as velocity diagrams.

First, consider the comparison of the measured total pressures with the ones from the CFD upstream and downstream of Rotor 9 in Figure 7.16. The total pressure distribution upstream of Rotor 9 is in Figure 7.16 (a); downstream is in Figure 7.16 (b), which is a reminder from Figure 7.4. The absolute flow angle downstream of Rotor 9, Figure 7.16 c), is the same plot, shown in Figure 7.3 in terms of the stator incidence. Here, only the corrected value of the measured angles is shown.

Analysing the three plots, one can see that, despite a relatively close total pressure rise for the experiment and the CFD (within 2%), the actual stator incidence is different, indicating either a difference in the axial velocity component or that in the rotor deviation. To analyse this, a velocity diagram for Rotor 9 can be built.

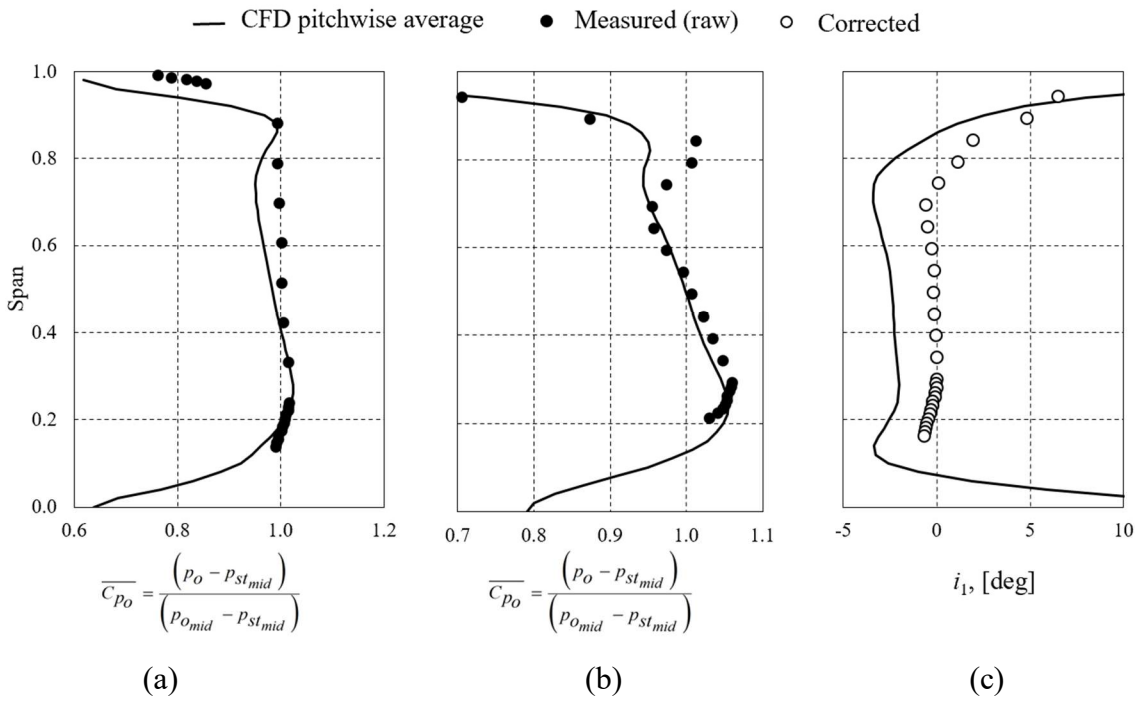

Figure 7.16 Total pressure profile upstream (a) and downstream (b) of Rotor 9 and the incidence angle at Stator 9 (c)

Figure 7.17 shows the velocity diagrams for Rotor 9. The solid lines are for the experimental results and the broken lines are for the simulation. The difference between the α_2 angles is shown in orange.

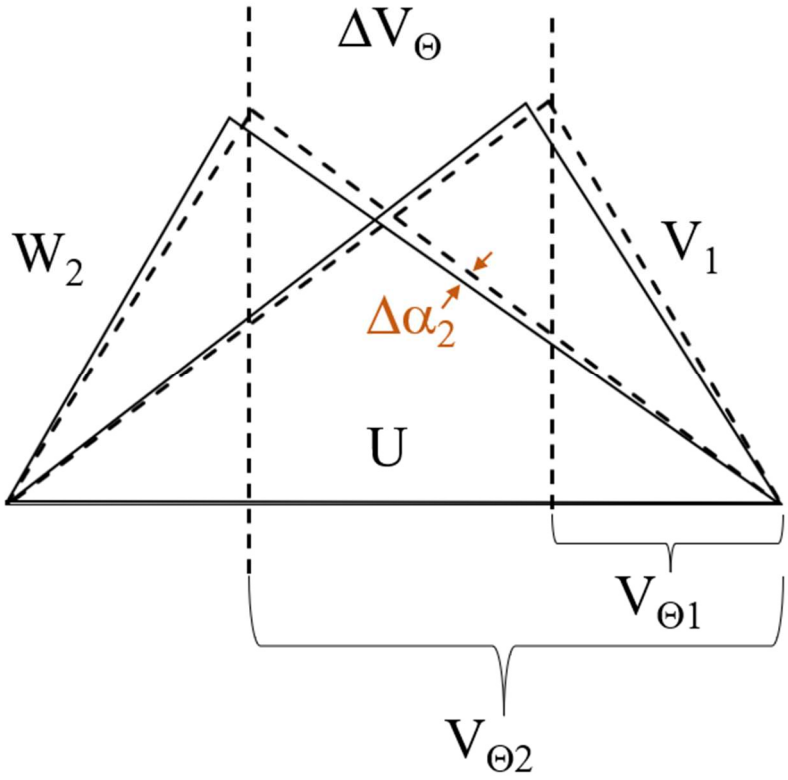

Figure 7.17 Velocity diagram for Rotor 9

The work input from the compressor rotor can be calculated as follows:

$$H_e = u\left(V_{\theta 2} - V_{\theta 1}\right) \tag{7.3}$$

Here, the H_e is the so-called Euler work; u is the circumferential speed of the blade, which is assumed to be uniform along the rotor; $V_{\Theta 1}$ and $V_{\Theta 2}$ are the circumferential components of the absolute velocity upstream and downstream of the rotor. The diagrams in Figure 7.17 for upstream and downstream of the rotor are matched together with the vector of blade speed so that the distance between the tips of the triangles represents the Euler work.

The velocity diagram is highly sensitive to uncertainties, both in flow angles and dynamic heads, especially when the vectors for the relative frame are calculated. For example, 5% uncertainty in the dynamic head upstream of the rotor can cause a 1° uncertainty in the incidence angle and up to 1.5° in the deviation. The 1° uncertainty in the flow angle

measurement in the absolute frame causes about 0.3° uncertainty for the angles in the relative frame. Overall, due to the measurement uncertainties, the image in Figure 7.17 would be less dramatic if all the errors in measurements were acting to one side: towards the CFD vectors. However, a similar situation with the measured flow being more swirled than the one from CFD was observed in multiple measurement sections with four probes and at separate times.

The difference in deviation should be treated with care, as the main reason for the difference between the CFD and the experiment is not caused by the blade incidence. According to the general theory of blade cascade aerodynamics, the deviation angle at the blade exit does not change much within a working range of incidence angles. For Stage 9 the incidence change of 2° will not cause any notable differences in deviation, which was proven by a series of CFD calculations along the stage speed line. Therefore, the observed difference in measured flow angles, which indicates the difference in rotor deviation, is not related to the rotor incidence. Instead, this is rather a modelling error, which was found for a given CFD solver and a family of airfoils used for a given compressor. A similar magnitude of error was reported by Place (1994) for a different set of compressor blades and observed by other researchers.

7.2.5 Casing pressure distributions

One of the most important metrics available to designers during multistage compressor testing is the pressure measured on the casing surface between the blade rows. These pressures can indicate the stage loading as well as the stage reaction, which can allow the designer to see the actual stage matching and better understand each stage's performance.

When the traversing results are available, the casing pressures are still valuable, as a source of consistency check: when the probe is inside the casing hole, all four pressures will be equal to that of the casing pressure sensor (this was especially valuable when measuring rear stages) in order to detect leakages in the traversing system before immersing the traverse. It was also used as a back pressure for the differential pressure sensors, whose range was chosen to be just enough to cover the expected dynamic head in the stages, but not the overall pressure ratio of the compressor.

One of the key design metrics, available from the early stage in the design process is the stage reaction. With an incompressible flow assumption that can be used for rear compressor

stages, the stage reaction can be calculated as the static pressure rise in the rotor divided by that of the whole stage:

$$\Lambda = \frac{P_{R_{ex}} - P_{R_{in}}}{P_{S_{ex}} - P_{R_{in}}} \tag{7.4}$$

At the same time, the kinematic stage reaction can be calculated from the velocity components:

$$\Lambda_{kin} = 1 - \frac{V_{\Theta_1} + V_{\Theta_2}}{2u} \tag{7.5}$$

In the first formula, the reaction can be calculated from the casing pressures, both experimentally and computationally. In the second formula, the velocity components from Figure 7.17 can be used in the middle span. For the high hub-to-tip ratio rear stages the kinematic stage reaction at the middle span is still representative of that near the casing, therefore the two values of stage reaction, calculated independently, can be compared against each other.

In Figure 7.18 the delta casing pressures for the blade rows are shown at the sections, where the experimental data is available. In this case, values larger than 1 mean that the static pressure rise in the CFD is larger than that measured. The horizontal axis shows the number of stages and integer numbers (1.0, 2.0…) are for the pressure rise in the rotor, and the halves (1.5, 2.5 and so on) are for the stators of the same stage. If the measured rotor and stator pressure deltas agree with the simulation, the same is true for the agreement in stage reaction.

However, it can be seen that, for the compressor of interest, the rotor pressure rise predicted in the CFD is larger than the measured one, and for the stator, it is the opposite. This means that the stage reaction is indeed different, which agrees with the observation from the velocity diagrams in Figure 7.17. For example, for Stage 9, the combined change in the rotor and stator pressure rise indicates a change in reaction by 3.5%. When processing the velocity diagrams at the middle span, the stage reaction in CFD is 2.8% higher than in the experiment. This provides evidence that the measured difference in the flow angle is consistent with the other available metrics for the research compressor.

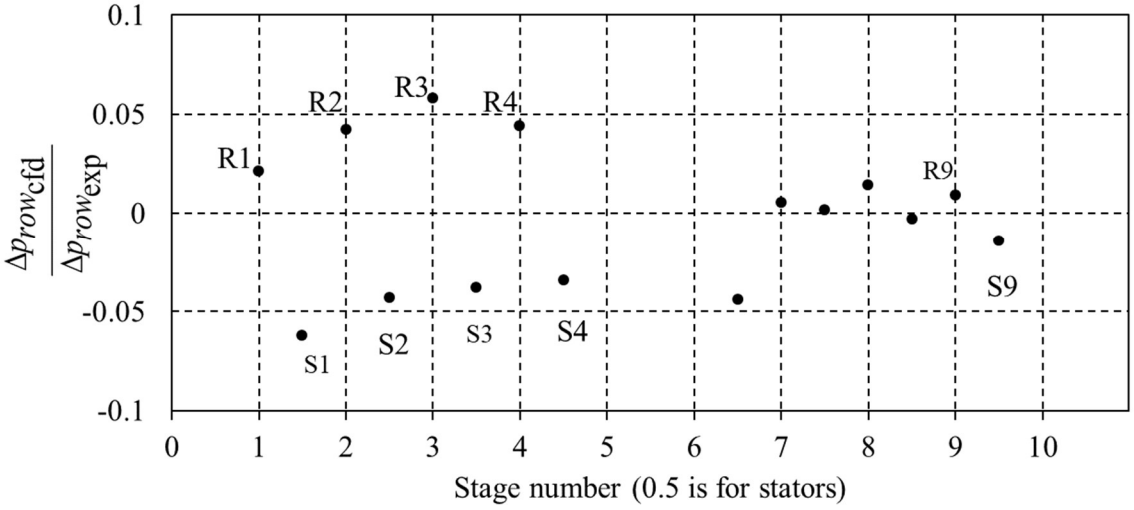

Figure 7.18 Delta casing pressures between the blade rows for CFD compared to the experiment

The stage pressure ratios on the casing along the compressor were within 2.5% agreement between the experiment and the CFD, with the biggest measured difference found in the first stage. This fact is again consistent with the difference in Stator 1 incidence indicating less turning in Rotor 1 for the CFD compared to the measured. For the first stage, the inlet boundary conditions are identical for both cases, therefore the deficit in rotor turning directly affects both the stage pressure ratio and its reaction.

Unfortunately, due to the limited access to the real engine, the middle stages were not traversed, and neither they were measured at the casing. This limited the possibility of consistency calculations along the whole compressor, so the differences between the computational model and the experiment cannot be tracked along the whole machine. For example, it was discovered during the project, that there is a concern regarding the mismatching between the group of four frontal stages and the rear part of the compressor. This caused significant flow separations in one of the middle stages, proven by the analysis of the flow visualisation on the blade surfaces of the real engine. Since it is known that RANS methods cannot always reliably simulate large separation zones, the biggest modelling uncertainty, and therefore, the largest difference with the experiment is expected to be in the middle group of stages for that compressor. In the next phase of the experimental campaign, it was planned to

study the middle stages in more detail, however, this was not realised within the timeframe of the presented research.

7.3 Concluding remarks

In this chapter, the corrections from Chapters 5 and 6 were applied to the real measurements in a multistage industrial compressor. The correction procedure consists of two major steps: the conversion of the measured values into the local flow values of undisturbed flow to account for the presence of the probe, and then the conversion of the local flow values into the representative pitchwise averaged values at a given span.

Before the corrections, the measured values of the mass flow integrated along the span were ±10–15% away from the inlet mass flow, measured independently. Measured pressures were more than 30% away from the ones calculated with mass conservation and radial equilibrium. After the corrections, the error in the mass flow fell within ±4%, and spanwise pressure gradients fell to within 3% from the radial equilibrium requirement.

Corrected measurements were then compared against multistage CFD results, and the differences were examined for self-consistency. For example, the difference in the stator inlet angle of 2° was proven to be consistent with the radial equilibrium condition downstream of the rotor, where the pressure gradient was larger by 20%. The differences in the measured velocity and angle were accounted for in the velocity diagram of the compressor stage and the difference in the kinematic reaction was found to be consistent with independently measured stage reaction based on casing pressure measurements between the blade rows.

The developed procedures allow for spanwise traversing results to be used in assessing the performance of industrial multistage axial compressors. With this procedure, the traversing results can provide more valuable and reliable data about the multistage compressors than was previously thought possible to obtain.

Chapter 8 Conclusions

For an advanced axial compressor design system, a high-fidelity experimental setup with spanwise measurement of the flow field is crucial for a deeper understanding of the three-dimensional flow structure in the real multistage compressor environment. However, such measurements have to be arranged in the limited space of inter-blade-row axial gaps at high flow speeds, which implies high measurement uncertainties and the risk of impact. The uncertainties are caused by the interaction between the probe and the blade flow field.

The aim of this study was to understand the physical mechanisms affecting the probe measurements in a multistage environment and to develop a procedure for measurement corrections during spanwise traversing that would improve the quality of the measured data. In this final chapter, the major findings of the work are summarised and recommendations for future work are outlined.

8.1 Major findings

The mechanisms affecting the probe readings were identified in Chapters 5 and 6. The immersed probe causes blockage in the measured flow field which changes the flow speed in the blade passage and flow redistribution to the neighbouring passages. In addition, the pressure distribution on the probe's surface is not the same at freestream calibration, including flow asymmetry and varying locations of the separation point on the probe's surface. However, these changes were found to be linear for certain probe locations and flow conditions, therefore the measurements under such conditions can be corrected.

The two limiting factors for the measurement corrections were found to be the presence of large vortical structures both around the probe and the blades, and the critical Mach number of the measured flow. In Chapter 5 it was shown that the probe-wake interaction with downstream blades significantly shifts the pressure distribution around the probe, causing nonlinear

deviations in the measurements. At a flow Mach number above 0.7, critical for cylindrical probes, the blockage effect of the probe becomes significant, and the interaction may change the flow field beyond the capabilities of the correction method. In Chapter 6 it was shown that when the probe interacts with blade wakes or corner separation zones, it causes a nonlinear transformation of these flow regions. Therefore, corrections for these effects are likely to be highly uncertain. Based on the limitations identified, low-uncertainty measurement locations were drawn for the compressor of interest for measurements both upstream and downstream of stator blades.

As a result, a two-step procedure for measurement corrections was developed. This enabled a single-point measurement at a given span to be converted into a representative flow metric, which can then be compared with the pitchwise-averaged values from the design code or CFD simulations. The corrections have been quantified in the form of linear equations, and the regions of high measurement uncertainty have been identified both for measurements upstream and downstream of stator blades.

The correction procedure based on two-dimensional flow field study have proven its validity for full three-dimensional setups with variable immersion of the probe away from the end walls. However, this finding is for a relatively slim holding stem: the ratio of the probe immersion to the stem diameter exceeds 40, whereas in the open literature this ratio is normally below 10. Therefore, it is important to validate the strength of the radial flow redistribution if an experimental setup has a stem geometry different to that used in this thesis.

As a result of the corrections procedure, the measurement uncertainties were reduced from ±6° down to ±1° for the flow angles. For the static pressure, the uncertainties were reduced from 35% of the dynamic head down to ±5%. These uncertainties are valid away from the end walls, near which the flow is highly skewed and has significant radial velocity components. The range of flow conditions and probe locations is defined where total pressure measurements are consistent and reliable without any corrections.

Developed methods have been applied to the real experimental results and have shown significant improvement in the self-consistency of the measurements. To control the consistency of the experimental data both before and after correction, a series of considerations were implemented, which were summarised in the consistency check procedure. This procedure is based on fundamental physical principles such as mass and energy conservation,

as well as radial equilibrium conditions for the turbomachinery flows. Without the corrections, the variations of the integrated mass flow, calculated along the compressor measurement sections, exceeded ±15%, which indicated serious issues with the experimental data. After the corrections, the variations of the mass flow fell within ±4%, with the remaining spread being caused by the measurement and process uncertainties.

A comparison of experimental results after corrections against CFD simulations revealed the differences in the amount of endwall blockage, especially near the casing in the frontal stages, and differences in exit flow angles. One of the findings was that the simulated flow has a larger deviation at the rotor exit compared to the measured values. The difference was proven to be consistent with other flow metrics, such as radial pressure gradient, and the reasons for that, as well as the changes in stage matching and compressor behaviour, can be explored by future researchers or industrial partners.

The developed methods, including the identification of necessary measurement corrections, the corrections procedure itself and the consistency check procedure, can be universally applied to similar compressors, as it accounts mainly for potential flow field interaction. The range of trustable locations and flow conditions is explained by the fundamental physical principles. Magnitudes of corrections and exact boundaries of the trustable regions can differ depending on blade geometry, including maximum thickness, leading edge diameter, loading style and design incidence, as well as relative probe size. These magnitudes and boundaries can be determined using CFD simulations in the same way as described in this thesis.

As a result of the presented study, knowledge about spanwise distributions of key aerodynamic parameters can enable a better understanding of the complex flows in industrial multistage axial compressors.

8.2 Recommendations for future work

The work in this thesis shows that if the probe measurements are well-understood and corrected for a constrained environment, the spanwise traversing can be beneficial to a compressor designer compared to currently used instrumentations of the stator leading edges, as it provides more flow variables at better spatial resolution. It will, however, only be practical if the probe is placed away from major vortical structures and the flow Mach number is below

a critical value for the probe so that the corrections are linear, and the correction procedure requires minimum input.

To extend the applicability of the spanwise traversing in industrial compressors, the author recommends that future work in the area should answer three questions. Firstly, how can the three-dimensionality of the flow redistribution caused by the probe immersion be universally corrected for? Secondly, what are the additional mechanisms causing the measurement uncertainties near the end walls and how can these uncertainties be quantified? And thirdly, what is the impact of flow unsteadiness on the probe readings?

8.2.1 Universality of the three-dimensional corrections

The change in the measurement corrections for various probe immersions along the span was found to be negligible, and the corrections for the three-hole pneumatic probe could be obtained from the quasi-two-dimensional calculations of the representative blade passage, providing that the probe free-jet calibration in the CFD accounts for the flow around the probe's tip. However, when strong radial flows are present in the compressor, and the flow is measured with a five-hole probe to capture such radial flows, the impact from the probe and the immersed stem can be more complicated. This is especially problematic when the stem interacts with the separation region near the casing or the blade suction side, so that the whole structure of the spanwise blockage changes a lot.

Understanding such interaction between the probe and fully three-dimensional flow in axial compressors can allow for a better understanding of the secondary flow features such as flows around corner separation zones and leakage flows.

8.2.2 Measurements near the end walls

In this study, for the measurements in the endwall regions, the corrections were extrapolated from the results of the mid-span, two-dimensional simulations. This resulted in sensible changes in spanwise parameter distribution near the end walls. However, the quantitative comparison of the full-span simulations with and without the probe showed a significant difference between virtually measured and undisturbed values; the uncertainty in these regions

has almost tripled. Therefore, the measurements in such regions require a better understanding of highly skewed, large pressure gradient flows around the probe tip.

For example, near the casing upstream of stators, the flow is highly distorted by the rotor tip vortex flow, and it also has a large velocity gradient due to the boundary layer on the casing surface. This results in a high skewness of the flow in that region so that the pressure distribution on the probe surface is no longer the same as it is at a uniform flow. This might affect the probe calibration characteristics used for data processing.

Similar problems arise when the probe is approaching the hub wall and the flow around the probe tip is dependent on the proximity to the hub wall. For shrouded stators, an understanding of such a flow field can allow for improved flow measurements near the hub wall, which is especially important for relatively large probe diameters typical of the rear stages in high-pressure axial compressors.

8.2.3 Unsteady effects on the probe readings

The key sources of uncertainty in an unsteady environment are the interaction with the rotor flow field, the vibration of the probe itself and the unsteadiness of the passage flow, especially when the probe is measuring downstream of the stator. In this work, the flow field downstream of the rotor was assumed to be averaged out due to the rotation. However, the actual flow field has high-frequency spikes in velocity profile due to blade wakes. It is unclear how these spikes are captured by the quasi-steady pneumatic probe, whose response time is several orders of magnitude higher than the wake frequency. In addition, the unsteadiness can affect the boundary layer conditions on the probe surface, thus impacting the probe's calibration characteristics.

Another source of uncertainty is the risk of probe vibration caused by the high immersion-to-diameter ratios of the holding stem. Three mechanisms can affect the flow measurements: first is a fluctuation in relative flow velocity due to the probe's relative motion during vibration. Second, the boundary layer transition and separation points shift due to the probe's motion. Third, the probe's oscillation results in changes in its relative position in the blade passage, and since the magnitude of the oscillations was found to be at a comparable scale with the probe

diameter, such a change in position can cause additional flow field redistribution and erroneous measurements.

It is not clear how these unsteady effects will affect the measurements, considering that the former not only experiences the variability of the upstream pressure field but also changes this field by going in and out of the blade passage. Studying the unsteady flow around an oscillating pneumatic probe in a fluctuating flow in proximity to the compressor blades would therefore be physically interesting and potentially important.

References

Adamczyk, J. J. (2000). Aerodynamic Analysis of Multistage Turbomachinery Flows in Support of Aerodynamic Design. ASME. *J. Turbomach*. April 2000; 122(2): 189–217. https://doi.org/10.1115/1.555439.

Aissa, M. H. and Verstraete, T. (2019). Metamodel-assisted multidisciplinary design optimization of a radial compressor. *International Journal of Turbomachinery, Propulsion and Power*, 4(4). https://doi.org/10.3390/ijtpp4040035.

Aschenbruck, J., Hauptmann, T., and Seume, J. R. (2015). Influence of a Multi-Hole Pressure Probe on the Flow Field in Axial-Turbines. Proceedings of 11th European Conference on Turbomachinery Fluid dynamics and Thermodynamics ETC11, March 23-27, 2015, Madrid, Spain.

Bailey, S. and Hultmark, M. (2013). Obtaining accurate mean velocity measurements in high Reynolds number turbulent boundary layers using Pitot tubes. *Journal of Fluid Mechanics*. 715.642-670.10.1017/jfm.2012.538.

Bauinger, S., Marn, A., Göttlich, E., and Heitmeir, F. (2017). Influence of Pressure Fluctuations on the Mean Value of Different Pneumatic Probes. *International Journal of Turbomachinery, Propulsion and Power*. 2.13.10.3390/ijtpp2030013.

Börner, M., Bitter, M., and Niehuis, R. (2018). On the challenge of five-hole-probe measurements at high subsonic Mach numbers in the wake of transonic turbine cascades. *Journal of the Global Power and Propulsion Society*. 2. JPRQQM. 10.22261/JGPPS.JPRQQM.

Brown, L. and Groh, F. (1962). Use of Experimental Interstage Performance Data to Obtain Optimum Performance of Multistage Axial Compressors. *Journal of Engineering for Power*. 84.187.10.1115/1.3673397.

Calvert, W. J., Ginder, R. B., McKenzie, I. R. I., and Way, D. J. (1989). Performance of a Highly-Loaded HP Compressor. Proceedings of the ASME 1989 International Gas Turbine

and Aeroengine Congress and Exposition. Volume 1: Turbomachinery. Toronto, Ontario, Canada. June 4–8, 1989. V001T01A012. ASME. https://doi.org/10.1115/89-GT-24

Chasoglou, A. C., Mansour, M., Kalfas, A. I., and Abhari, R. S. (2018). A novel 4-sensor fast-response aerodynamic probe for non-isotropic turbulence measurement in turbomachinery flows. *Journal of the Global Power and Propulsion Society* 2. 362–375.

Chernoray, V. and Hjärne, J. (2008). Improving the Accuracy of Multihole Probe Measurements in Velocity Gradients. 2.10.1115/GT2008-50492.

Chilla, M., Pullan, G., and Gallimore, S. (2020). Reducing Instrumentation Errors Caused by Circumferential Flow-Field Variations in Multistage Axial Compressors. *Journal of Turbomachinery*. 142.1-13.10.1115/1.4047610.

Clark Di Leoni, P., Mazzino, A., and Biferale, L. (2020). Synchronization to Big Data: Nudging the Navier-Stokes Equations for Data Assimilation of Turbulent Flows. Physical Review X. 10(1), 11023. https://doi.org/10.1103/PhysRevX.10.011023.

Clark, C. J. and Grimshaw, S. D. (2019). A pneumatic probe for measuring spatial derivatives of stagnation pressure. In: Proceedings of the ASME Turbo Expo. Vol. 6. 2019. ISBN:9780791858677. DOI: 10.1115/GT2019-91428.

Coldrick, S., Ivey, P., and Wells, R. (2003a). Considerations for Using 3-D Pneumatic Probes in High-Speed Axial Compressors. J. Turbomach. Jan 2003, 125(1):149–154.

Coldrick, S. (2003b). The Influence of Blade Row Aerodynamics on Pneumatic Gas Turbine Instrumentation. Thesis, Cranfield University, 2003. http://dspace.lib.cranfield.ac.uk /handle/1826/11295.

Coldrick, S., Ivey, P. C., and Wells, R. G. (2004a). The Influence of Compressor Aerodynamics on Pressure Probes: Part I — In Rig Calibrations. Proceedings of the ASME Turbo Expo 2004: Power for Land, Sea, and Air. Volume 2: Turbo Expo 2004. Vienna, Austria. June 14–17, 2004. ASME. 10.1115/GT2004-53240.

Coldrick, S., Ivey, P. and Wells, R. (2004b). The Influence of Compressor Aerodynamics on Pressure Probes: Part 2 — Numerical Models. Proceedings of the ASME Turbo Expo 2004: Power for Land, Sea, and Air. Volume 2: Turbo Expo 2004. Vienna, Austria. June 14–17, 2004. ASME. 10.1115/GT2004-53241.

Cruz, G. G., Babin, C., Ottavy, X., and Fontaneto, F. (2021). Bayesian Inference of Experimental Data for Axial Compressor Performance Assessment. In Volume 2A:

Turbomachinery — Axial Flow Fan and Compressor Aerodynamics (Vol. 2A-2021). American Society of Mechanical Engineers. https://doi.org/10.1115/GT2021-59200.

Cumpsty, N. A. (2004). *Compressor Aerodynamics*. Krieger.

Denton, J. D. (1978). Throughflow Calculations for Transonic Axial Flow Turbines. ASME. *J. Eng. Power*. April 1978; 100(2):212–218. https://doi.org/10.1115/1.3446336.

Dransfield, D. C. and Calvert W. J. (1976). Detailed flow measurements in a four-stage axial compressor. ASME paper 76-GT-46.

Eckardt, D. (2014). Gas Turbine powerhouse: The development of the power generation gas turbine at BBC – ABB – ALSTOM, 2nd edition. 10.1057/9783110359770.

Falchetti, F. (1992). Advanced CFD simulation and testing of compressor blading in the multistage environment. *International Journal of Rotating Machinery.* 10.2514/6.1992-3040.

Georgiou, D. P. and Milidonis, K. F. (2014). Fabrication and calibration of a sub-miniature 5-hole probe with embedded pressure sensors for use in extremely confined and complex flow areas in turbomachinery research facilities. *Flow Measurement and Instrumentation* 39. 54–63. DOI: 10.1016/j.flowmeasinst.2014.07.005.

Grimshaw, S. D. and Taylor, J. V. (2016). Fast-settling millimetre-scale five-hole probes. In: Proceedings of the ASME Turbo Expo. Vol. 6. ISBN: 9780791849828. DOI:10.1115/GT2016-56628.

Hayase, T. (2015). Numerical simulation of real-world flows. *Fluid Dynamics Research*, 47(5), 51201. https://doi.org/10.1088/0169-5983/47/5/051201

He, X., Ma, H., Ren, M., and Xiang, H. (2012). Investigation of the Effects of Airfoil-probes on the Aerodynamic Performance of an Axial Compressor. *Chinese Journal of Aeronautics*. 25. 517–523. 10.1016/S1000-9361(11)60415-9.

Hönen, H., Kunte, R., Waniczek, P., and Jeschke, P. (2012). Measuring Failures and Correction Methods for Pneumatic Multi-Hole Probes. ASME Turbo Expo 2012: Turbine Technical Conference and Exposition 10.1115/GT2012-68113.

Ikeguchi, T., Matsuoka, A., Sakai, Y., Sakano, Y., and Yoshiura, K. (2012). Design and Development of a 14-Stage Axial Compressor for Industrial Gas Turbine. Proceedings of the ASME Turbo Expo 2012: Turbine Technical Conference and Exposition. Volume 8:

Turbomachinery, Parts A, B, and C. Copenhagen, Denmark. June 11–15, 2012. 125–134. ASME.

Kupferschmied, P. (1998). Zur Methodik zeitaufgelöster Messungen mit Strömungssonden in Verdichtern und Turbinen. ETH dissertation No. 12774, Zürich, Switzerland.

Lakshminarayana, B., Suryavamshi, N., Prato, J., and Moritz, R. (1996). Experimental Investigation of the Flow Field in a Multistage Axial Flow Compressor. *International Journal of Rotating Machinery*. 2. 10.1155/S1023621X96000127.

Lecheler, S., Schnell, R., and Stubert, B. (2001). Experimental and Numerical Investigation of the Flow in a 5-Stage Transonic Compressor Rig. Proceedings of the ASME Turbo Expo 2001: Power for Land, Sea, and Air. Volume 1: Aircraft Engine; Marine; Turbomachinery; Microturbines and Small Turbomachinery. New Orleans, Louisiana, USA. June 4–7, 2001. V001T03A040. ASME.

Lee, S. and Yoon, T. (1999). An investigation of wall-proximity effect using a typical large-scale five-hole probe. *KSME International Journal*. 13. 273–285. 10.1007/BF02970486.

Lopes, G., Simonassi, L., Torre, A.F.M., and Lavagnoli S. (2022) Instrumentation Interference In a Transonic Linear Cascade. Proceedings of XXVI Biennial Symposium on Measuring Techniques in Turbomachinery Transonic and Supersonic Flow in Cascades and Turbomachines, Pisa, Italy.

Lou, F. and Key, N. L. (2020). Reconstructing Compressor Non-Uniform Circumferential Flow Field From Spatially Undersampled Data—Part 1: Methodology and Sensitivity Analysis. Proceedings of the ASME Turbo Expo GT2020-14867. 1–12.

Lou, F. and Key, N. L. (2021). Reconstructing Compressor Non-Uniform Circumferential Flow Field From Spatially Undersampled Data—Part 1: Methodology and Sensitivity Analysis. *ASME. J. Turbomach*. August 2021; 143(8):081002.

Lou, F., Matthews, D. R., Iii, N. J. K., and Key, N. L. (2020). Reconstructing compressor non-uniform circumferential flow field from spatially undersampled data – Part 2: Pratical application for experiments. Proceedings of the ASME Turbo Expo GT2020-15465. 1–12.

Ma, H., Li, S., and Wei, W. (2014). Effects of Probe Support on the Flow Field of a Low-Speed Axial Compressor. *Journal of Thermal Science*. 23. 10.1007/s11630-014-0685-7.

Menter, F. R., Langtry, R. B., Likki, S. R., Suzen, Y. B., Huang, P. G., and Völker, S. (2004). "A Correlation-Based Transition Model Using Local Variables—Part I: Model Formulation." ASME. *J. Turbomach*. doi: https://doi.org/10.1115/1.2184352

McKenzie, A. (2000). The design and performance of axial compressor stages in fully developed flow. Proceedings of The Institution of Mechanical Engineers Part A-journal of Power and Energy - PROC INST MECH ENG A-J POWER. 214. 575–583. 10.1243/0957650001538119.

Mito, R., Walker, T., Hamana, H., Gao, X., and Sakamoto, Y. (2015). Computational Fluid Dynamics Technology Applied to High Performance, Reliable Axial Compressors for Power Generation Gas Turbines. Mitsubishi Heavy Industries Technical Review Vol. 52 No. 1.

Munivenkatareddy, S. and Sitaram, N. (2016). Extended Calibration Technique of a Four-Hole Probe for Three-Dimensional Flow Measurements. Hindawi Publishing Corporation *International Journal of Rotating Machinery* Volume 2016, Article ID 5327297.

Mutlu Sumer, B. and Fredsoe. J. (1999). Hydrodynamics around cylindrical structures, volume 12 of Advanced series on coastal engineering. World Scientific.

Ng, H. and Coull, J.D. (2017). Parasitic Loss Due to Leading Edge Instrumentation on a Low-Pressure Turbine Blade. *J. Turbomach*. Apr 2017, 139(4):041007.

Outa, E., Hamana, H., and Mito, R. (2016). Development and Current Status of the Compressors for Industrial Gas Turbines. *Journal of the Society of Mechanical Engineers*. 119. 438–441. 10.1299/jsmemag.119.1173_438.

Pianko, M. and Wazelt, F. (1982). Propulsion and Energetics Panel Working Group 14 on Suitable Averaging Techniques in Non-Uniform Internal Flows. AGARD Advisory Report No 182. Advisory Group for Aerospace Research and Development. Neuilly Sur Seine, France.

Place, J. M. M. (1997). Three-Dimensional Flow in Axial Compressors. PhD thesis, Cambridge University Engineering Department, Cambridge, UK.

Sanders, C, Terstegen, M, Hölle, M, Jeschke, P, Schönenborn, H, and Fröbel, T. (2017). Numerical Studies on the Intrusive Influence of a Five-Hole Pressure Probe in a High-Speed Axial Compressor." *Proceedings of the ASME Turbo Expo 2017: Turbomachinery Technical Conference and Exposition*. *Volume 2A: Turbomachinery*. Charlotte, North

Carolina, USA. June 26–30, 2017. V02AT39A009. ASME. https://doi.org/10.1115/GT2017-63399

Schnoes, M, Voß, C, and Nicke, E. (2018). Design optimization of a multi-stage axial compressor using throughflow and a database of optimal airfoils. *Journal of the Global Power and Propulsion Society*.2018;2:516-528. doi:10.22261/JGPPS.W5N91I.

Seki, R., Yamashita, S., and Mito, R. (2021). Evaluation of a Flow Measurement Probe Influence on the Flow Field in High Speed Axial Compressors. Proceedings of the ASME Turbo Expo 2021: Turbomachinery Technical Conference and Exposition. Volume 2A: Turbomachinery — Axial Flow Fan and Compressor Aerodynamics. Virtual, V02AT31A001. ASME.

Seki, R., Yamashita, S., and Mito, R., 2021 Evaluation of a Flow Measurement Probe Influence on the Flow Field in High-Speed Axial Compressors. Proceedings of ASME Turbo Expo 2021 (online), 7-11 June 2021. ASME Paper No. GT2021-58558.

Seshadri, P., Duncan, A., Simpson, D., Thorne, G., and Parks, G. (2020). Spatial Flow-Field Approximation Using Few Thermodynamic Measurements—Part II: Uncertainty Assessments. ASME. *J. Turbomach*. February 2020; 142(2): 021007. https://doi.org/10.1115/1.4045782

Seshadri, P., Duncan, A., Thorne, G., Parks, G., Vazquez Diaz, R., and Girolami, M. (2022). Bayesian assessments of aeroengine performance with transfer learning. Data-centric Engineering, 3, e29. doi:10.1017/dce.2022.29.

Sieverding C. H. (1993). Advanced methods for cascade testing. AGARD AG 328.

Sieverding, C. H., Arts, T., Dénos, R., and Brouckaert, J. -F. (2000). Measurement techniques for unsteady flows in turbomachines. *Experiments in Fluids.* 28. 285–321. 10.1007/s003480050390.

Sitaram, N., Lakshminarayana, B., and Ravindranath, A. (1981). Conventional probes for the relative flow measurement in a turbomachinery rotor blade passage. *J. Eng. Power* 103, 406–414.

Smout, P. D. and Ivey, P. C. (1997). Investigation of Wedge Probe Wall Proximity Effects: Part 1—Experimental Study. ASME. J. Eng. Gas Turbines Power. July 1997; 119(3):598–604. https://doi.org/10.1115/1.2817026.

Steffens, K. (2013). Advanced compressor Technology – Key Success Factor for Competitiveness in Modern Aero Engines. MTU Aero Engines.

Stringham, G. Cassem, B., Prince, T., and Yeung, P. (1998). Design and Development of a Nine Stage Axial Flow Compressor for Industrial Gas Turbines. V001T01A042. 10.1115/98-GT-140.

Tanaka, R, Koji, T, Ryu, M, Matsuoka, A, and Okuto, A. (2012). Development of High Efficient 30MW Class Gas Turbine: The Kawasaki L30A. *Proceedings of the ASME Turbo Expo 2012: Turbine Technical Conference and Exposition*. *Volume 3: Cycle Innovations; Education; Electric Power; Fans and Blowers; Industrial and Cogeneration*. Copenhagen, Denmark. June 11–15, 2012. pp. 883-889. ASME. https://doi.org/10.1115/GT2012-68668.

Treaster, A. L. and Yocum, A. M. (1979). Calibration and Application of Five-Hole Probes. In: *ISA Transactions* 18.3. 23–34. ISSN: 00190578.

Tweedt, D. L. and Okiishi, T. H. (1983). Stator Blade Row Geometry Modification Influence on Two-Stage, Axial-Flow Compressor Aerodynamic Performance. Technical report AD-A141 793.

Vasseur A., Binder N., Champion J.-L., and Fontaneto, F. (2022). Evolution of a Five-Hole Probe Calibration Near a Wall. Proceedings of XXVI Biennial Symposium on Measuring Techniques in Turbomachinery Transonic and Supersonic Flow in Cascades and Turbomachines, Pisa, Italy.

Wellborn, SR, and Delaney, RA. (2001). Redesign of a 12-Stage Axial-Flow Compressor Using Multistage CFD. *Proceedings of the ASME Turbo Expo 2001: Power for Land, Sea, and Air*. *Volume 1: Aircraft Engine; Marine; Turbomachinery; Microturbines and Small Turbomachinery*. New Orleans, Louisiana, USA. June 4–7, 2001. V001T03A047. ASME. https://doi.org/10.1115/2001-GT-0351

Wyler, J. S. (1975). Probe Blockage Effects in Free Jets and Closed Tunnels. ASME. *J. Eng. Power.* October 1975; 97(4):509–514. https://doi.org/10.1115/1.3446046.

Xiang, H., Ge, N., Hou, M., Gao, J., and Rongfei, Y. (2016). An experimental investigation of the effects of upstream probe disturbance on compressor cascade performance. Proceedings of the Institution of Mechanical Engineers, Part G: *Journal of Aerospace Engineering*. 231. 10.1177/0954410016652435.

Zdravkovich, M. M. (1997). *Flow Around Circular Cylinders: Volume 2: Applications.* OUP Oxford, 1997. 592.

Zhang, D., Cheng, L., An, H., and Draper, S. (2020). Flow Around a Surface-Mounted Finite Circular Cylinder Completely Submerged Within the Bottom Boundary Layer. *European Journal of Mechanics, B Fluids* 86 (2021).169–197.

Zhong, Y., Ma, H., and Yang, Y. (2021). Effects of Probe Stem Surface Suction on the Aerodynamic Performance of a Compressor. Proceedings of the ASME Turbo Expo 2021: Turbomachinery Technical Conference and Exposition. Volume 2A: Turbomachinery — Axial Flow Fan and Compressor Aerodynamics. Virtual, Online. June 7–11, 2021. V02AT31A024. ASME. https://doi.org/10.1115/GT2021-59047

Zhou, C., Yue, Z., and Jin, D. (2022). Improving experiment data process accuracy for axial compressors: Converting inter-stage data into meridional flow fields. Proceedings of the Institution of Mechanical Engineers, Part G: *Journal of Aerospace Engineering*. 236(12):2483-2495. doi:10.1177/09544100211063686.